University of Naples “Federico II”

Low Field Magnetic Sensing with Giant Magneto Resistive Sensors

Federica Di Iorio

A dissertation submitted for the Doctor of Philosophy degree in
Innovative Technologies for Materials, Sensors and Imaging
XIX cycle

Coordinator:
Prof. Giancarlo Abbate

December 2007

Introduction

Giant Magnetoresistance (GMR) development, followed by work in magnetic tunnel junctions (MTJ), and spin electronic devices (SPINS) show now increasing interest for many applications in the information technology and magnetometry. Because of their small size, low power, and relatively low cost, solid state sensors that detect magnetic fields lower than Earth's have found several applications in all major industries. The resulting improvements in magnetoresistance have been accompanied by rapid exploitation of these new magnetics structures in magnetic sensors, read heads and nonvolatile memory (MRAM). GMR sensors are being used to determine precise magnetic orientation and to detect natural and man-made geophysical anomalies, various physiological functions, metal defects and minute particles associated with immunoassay. New applications are being discovered daily as the current technology involves limitations due to size, weight, power consumption, and cost. As these applications develop, there is an emerging requirement to provide new probes of low-field magnetic sensors for magnetic field images of the subject material or, as in the case of bioassays, to handle multiple variables simultaneously. Application areas being investigated include NDE (Non Destructive Evaluation) eddy-current mapping for defect detection in metallic materials, geophysical anomalies, and bioassays.
This work is mainly focused with the study of the Giant Magnetoresistive sensors (GMR) and their potentiality concerning the Non Destructive Evaluation applications. The experimental activity as been followed in the CNR-INFM Coherentia laboratories of Naples situated in the University Federico II faculty of Engineering. More details of the thesis include as follow:

In chapter I, some major GMR applications have been illustrated. Among all quoted applications, the discussion is focused on computer memory and storage applications in information technology industry, biosensing applications and Non Destructive Evaluations (NDE) using magnetic probes.

The chapter II contains a brief review of the giant magnetoresistance (GMR) effect exhibited by magnetic multilayers, granular alloys, and related materials. Various and much different physical origins can be responsible of the effect in the different systems. By starting with the

magnatoresistance (MR) effect characterization, we include a description of the main phenomenon in term of spin-dependent conduction and electronic band structure in magnetic multilayers.

The chapter III includes the main theoretical models used to describe the GMR behaviour and the electronic transport properties of magnetic multilayers. In this study, our attention will be aimed above all to the semiclassical Boltzmann theory which permits to obtain macroscopic transport equations of magnetic multilayers for current perpendicular to the layers. These macroscopic equations will be used to extract, with the aid of numerical simulation, the GMR behaviour of a magnetic multilayer.

The chapter IV will report the experimental characterization of the sensors including magnetic background noise analysis, conversion factor and non destructive measurements on several materials. The interest linked to this kind of sensors is addressed to the improvement of performances related to the spatial resolution and sensitivity. Thus, our study aimed to estimate the optimal configuration for a system of commercial GMR sensors. Our attention has been focused mainly to the gradiometric configuration. In fact, the use of GMR sensors in gradiometric configuration, together with the applied filtering technique, enables the strong reduction of the magnetic noise increasing the signal to noise ratio. The results coming from the measurements, taken on different materials, allows to understand the advantage of using an electronic gradiometer and the reliability of our experimental probe.

Acknowledgments

First of all, I wish to thank my supervisors Ing. Massimo Valentino and Prof. Antonello Andreone that relied in my competence and for giving me the right mentor during this thesis.
Only thanks to their expertise and patience this work can see the light.
I would also like to thank the head of the group Prof. Antonio Barone and the Prof. Ruggero Vaglio for giving me the possibility to continue these PhD studies despite my job busies.

A special thank to Gianrico who always is a supporter of my stubbornness to terminate what I begin. All PhD schools should be flat without Carmela's fellowship and I wish to thank her for my initialization in NDE field. Thanks to Antonio Maggio and Stefano Marrazzo for the technical support. And outside the laboratory, Roberto and all my colleagues of "GIOVE B" that took my place when I was studying.

Everything has been achievable and will keep on, thanks to my family who always trust in me and my niece Milena who gives me a smile every time I need.

Federica Di Iorio
December 2007

Contents

I Low-Field Magnetic Applications in Industry and Medicine

Industry continues to reap the benefits of solid state magnetic field sensing. Every day new applications are found for solid state magnetic field sensors due to their small size, low power and relatively low cost. The new frontier for these solid state sensors is very low magnetic fields. GMR technology is being applied to low-field magnetic applications and the newer GMR technologies such as Spin Dependent Tunnelling (SDT) will make even more of these applications possible. The chapter illustrates some major GMR application, already available nowadays, and enforce the importance of this technology.

There are many places in industry and in medicine in which magnetic fields the size of the Earth's magnetic field and smaller are of interest. The source of these fields can be magnetized objects, electrical currents, or the Earth's field itself. For this purpose, magnetic field sensing is often utilized for control and measurement. Generally in these applications, relatively large magnetic fields are used to avoid confusion with background magnetic fields such as the Earth's magnetic field, fields from ferromagnetic objects, and EMI. The fields detected are provided either from permanent magnets or from currents in coils, sometimes with soft magnetic cores. The size of these magnetic fields is usually tens to hundreds of Oe.

Since magnetic field sources are inherently dipole in nature, they decrease with the inverse cube of distance and, sometime, the low-field aspect of these applications can be due to the distance to a magnetic object or the size of the magnetic object itself. Therefore, the fields from these sources are relatively localized. Despite the increased measurement difficulties encountered, low magnetic fields are gaining increasing attention in industry. It is enough to think to computer memory and storage technology, Non Destructive Evaluations (NDE), biosensing applications, tomography, aeronautical and aerospace compass applications, motor vehicles surveying, currencies and other negotiable documents identification or validation and so on.

In this context, our attention is focalized to a solid state magnetic field sensors alternative technology. Since the discovery of giant magnetoresistance (GMR), magnetoresistive devices have progressed rapidly from the anisotropic magnetoresistance (AMR) structures that were the dominant thin film magnetoresistive material into the 1990s. GMR development, followed by work in magnetic tunnel junctions (MTJ), is now being amplified by the latest work in spin electronic devices (SPINS). These devices have an inherent advantage in size and power when compared to search coil, flux gate, and more complicated low-field sensing techniques such as Superconducting Quantum Interference Devices (SQUID) and spin resonance magnetometers. A solid-state magnetic sensor directly converts the magnetic field into a voltage or resistance with, at most a dc current supply. The sensing can be done in an extremely small, lithographically patterned area further reducing size and power requirements. The small size of a solid state element increases the resolution for fields that change over small distances and allows for packaging arrays of sensors in a small package.

Among all quoted applications, here the discussion is reduced to computer memory and storage applications in information technology industry and its market interest, biosensing applications and tomography as regard medicine and geophysics, to finish with Non Destructive Evaluations (NDE) that is our main field of interest.

I.1. The development of MRAM and data storage technology

Semiconductors and magnetic materials play an important role in the electronic devices. Data processing is carried out by carrier charge in semiconductor devices. In contrast, hard disk drives, which are representative of electron device using magnetic materials perform data processing using spin in the magnetic materials.

These two electron devices have been studied independently and have not always been developed together. In the semiconductor field, Si micro-fabrication and integration have realized large capacity memory devices, such as DRAMs. The study of magnetism has sought development of new and high- quality materials rather than the micro-fabrication of magnetic materials.

The discovery of the giant magnetoresistance (GMR) effect [*Ref. I.2*] in artificial superlattices and the giant tunnel magnetoresistance (TMR) at room temperature [*Ref. I.3*] triggered the formation of the spintronics field, where transport properties play an important role along with magnetic properties.

Figure I.1 summarizes the concept of spintronics, in which magnetic and semiconducting technologies play an important role. Both the spin and charge of electrons may contribute to discovery of new functional devices that will break in limits imposed on existing devices.

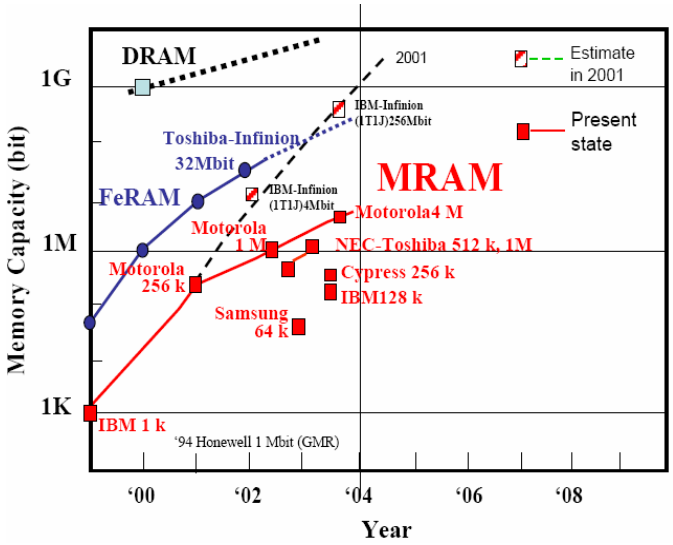

Figure I.1 MRAM capacities are shown for different years. DRAM and FeRAM points are also shown for comparison [Ref. I.1].

The study of magnetic RAM began in 1948 using a ferrite core that possessed a square hysteresis loop. In 1955, a square hysteresis loop with a small coercive force was reported for Ni-Fe (permalloy) and these devices together with permalloy wire memory began to be developed in the 1960s. Further improvements in magnetic memory density, though without performance or cost benefits, were demonstrated in the 1970s by yet another type of magnetic memory technology, bubble memory, although none competed economically with semiconductor memories. On the other hand, magnetoresistive random access memory, called simply MRAM, was proposed first in 1972 [*Ref. I.4*]. Then several memory cells made of Fe-Ni-Co alloys were demonstrated, even if the output signals of these memory cells were small because of the small magnetoresistance ratio[*Ref. I.5 -Ref. I.7*].

In 1988, the discovery of giant magnetoresistance in magnetic multilayers and sandwiches revealed large magnetoresistance ratio at liquid helium temperature [*Ref. I.2*]. At the same time, the evolution of deposition techniques allowed the application of artificial tunnel barrier technique to magnetic tunnel junctions (MTJ).

First, in 1991, Miyazaki and co-workers at Tohoku University reported NiFe/Al–Al_2O_3/Co junctions with TMRs of 2.7% at room temperature. This was a significantly higher percentage than earlier room temperature results, but far lower than expectations [*Ref. I.8*, *Ref. I.9*].

The invention of the spin valve device showed great promise for read-head sensors for hard disk drives, to propose the use of a spin-valve-based MRAM. The new magnetic device, the magnetic tunnel junction (MTJ), began to emerge in the mid-1990s [*Ref. I.15*].with the potential to enable a new memory that could simultaneously achieve high speed, high density, and non volatility.

Finally, in 1994 two groups working independently, both using artificial tunnel barriers of Al_2O_3, obtained magnetoresistance values at room temperature that began to approach the magnitude expected. Miyazaki and Tezuka, experimenting with Fe–Al_2O_3–Fe structures, obtained an 18% effect at room temperature [*Ref. I.3*], while Moodera et al. at MIT, working with CoFe–Al_2O_3–Co, produced effects of up to 11.8% at room temperature [*Ref. I.10*].

The first MRAM cell with MTJ was reported by Wang and Nakamura [*Ref. I.15*] in 1996. They called this memory spin tunnelling random access memory (STram). Essential attributes of this MRAM technology are non-volatility and unlimited read and write endurance. In addition it can operate at high speeds up to several nanoseconds, but far to have competitive densities.

These evolution shifted the interest to this type of magnetic RAM also for the military and aerospace market. This broader range of applicability has led to widespread research and

development activity aimed at demonstrating magnetic tunnel junction random access memory with commercial market potential.

In 1999, IBM [*Ref. I.11*].and Motorola [*Ref. I.12*] developed 1 kbit and 512 bit MRAMs, respectively. Motorola developed successfully 1 Mbit, 2 Mbit and 4 Mbit MRAMs [*Ref. I.13*] In Japan, NEC and Toshiba cooperated and developed a 1 Mbit MRAM in 2003 [*Ref. I.14*]. Today, a big effort comes from IBM to demonstrate of basic capabilities of the MTJ technology. IBM researchers work on a 16-Mb ‘‘product demonstrator’’ design in 180-nm node technology, which was targeted to be a realistic test bed for the MRAM technology (2006) [*Ref. I.16*]. 16-Mb MRAM is the largest MRAM yet fabricated, with the smallest cell size ($1.42\mu m^2$) among multi-megabit MRAM designs. The main features of the design are summarized in the Table I.1 below.

Interface	16-Mb asynchronous SRAM (1 Mb x 16)
Technology	CMOS 7sf (180 nm), 1-poly, 3-Cu metal
MRAM specific layers	Three-level MRAM adder
Chip size	7.9 mm x 10 mm
Cell size	1.42 μm^2 (efficiency ;30%)
Vdd	2.3–3.3 V or 1.8 V
Access/cycle times	Read: 30 ns Write: 30 ns
Active current (read)	25 mA @ 30 ns
Active current (write)	80 mA @ 30 ns
Standby current	32 μA
Deep power-down current	5 μA, no loss of data

Table I.1 Design parameters for 16-Mb MRAM. Data from Ref. I.16.

Following the initial demonstration of high TMR at room temperature, it was quickly recognized that the magnetic tunnel junction had a number of properties that would make it very attractive for the read operation in a very dense memory cell (see Table I.2).

High magnetoresistance (MR) advantage	advantage
High resistance	advantage
Controllable resistance	advantage
Weak temperature dependence	advantage
Scalable to small sizes with high MR	advantage
MR falls off with increasing voltage	disadvantage

Table I.2 Magnetic tunnel junction properties for read operation.

The high magnetoresistance is important for obtaining a large signal from a memory cell, especially if a fast read operation is desired. Equally important the high resistance of a magnetic tunnel junction, compared with that of earlier magnetic devices, is compatible with high-speed sensing using CMOS circuitry. The high resistance is introduced in a very compact structure, basically in the space of an electrical via connection between two wiring layers. The resistance depends exponentially on the thickness of the very thin tunnel barrier, of the order of 10 to 20$\mathring{A}$. The extremely small thicknesses involved might appear to make the resistance difficult to control but early improvements in deposition techniques demonstrated that it is possible to control the resistance making it tunable from $60\Omega/\mu m^2$ to $10^7\Omega/\mu m^2$. Another essential attribute of magnetic tunnel junctions for read operations in a memory is that their electrical properties vary only slowly with temperature. The important scale for temperature variations is set by the Curie temperature of the magnetic electrodes, which is of the order of $500°C$ or greater in commonly used alloys of Ni, Fe, and Co. Important for future scaling, the magnetic tunnel junction could be scaled to very small sizes while its magnetoresistance value remained unchanged.

The only negative aspect of the properties of the magnetic tunnel junction from a read perspective is that the magnitude of the magnetoresistance effect falls off with increasing voltage. However, this range of falloff is slow enough to result in a sufficiently large signal for sensing by memory readout circuitry; with improvements in MTJ quality, typical half voltages currently range from $500mV$ to more than $700mV$.

As before, the magnetic tunnel junction device, with its large magnetoresistance signal, its CMOS-compatible [*Ref. I.17*] resistance value, and its compact structure, has led to the consideration of several MRAM architecture possibilities. As concern, early anisotropic magnetoresistance (AMR) and spin-valve devices pursued for MRAMs, it is well-known that, because of the small signal required, the magnetic storage state of those devices could be disturbed in some manner (destructively or non destructively) during the read operation in order to provide a self-reference signal. The small signal and associated, complex referencing and sensing operations inevitably result in a slow read operation. The TMR device, on the other hand, could be laid out compactly and placed in series with a switch element (either an FET transistor or a diode) and sensed directly, assuming that tracking variations of the resistance value between different TMR elements are smaller than the magnetoresistance ratio.

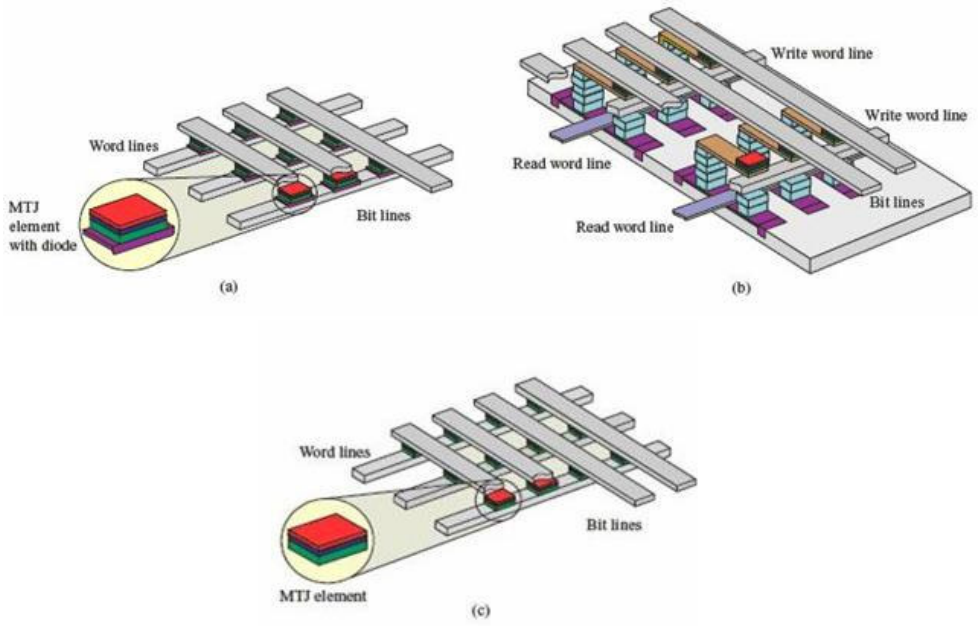

Figure I.2 MRAM architectures. (a) Cross-point architecture with thin-film diode in the tunnel junction stack. (b) FET architecture. (c) Switchless cross-point architecture.

Figure I.2 shows three architectures that should permit MRAM realizations because of the large signal of the TMR element. Figure I.2(a) shows a particularly compact ‘‘cross-point’’ arrangement in which each magnetic tunnel junction stack also contains a thin-film diode. The diode serves to block the sneak current paths in the matrix arrangement of the cells. During a read operation, a cell is selected by grounding one word line while all of the other word lines are biased as high as the sense line. Then, just one device along a bit line will be forward-biased, and the current that flows through it will be detected. The requirements for high-speed operation of this type of array are 1) that the diode carry a relatively high forward current so that the voltage drop across it when forward biased is less than that across the magnetic tunnel junction and 2) that the diode have a high rectification ratio in order to limit sneak paths in large arrays. For the compact cross-point structure, the diode must be formed above a wire that can carry substantial current (several milliamps). Unfortunately, the forward conductance of thin-film diodes that can be formed on high-conductivity metal wires is insufficient for high-speed cells with small areas. It has thus not been possible to realize this very attractive architecture.

A second architecture, shown in Figure I.2(b), utilizes an FET switch in the substrate to eliminate the sneak paths during the read operation. The cell area is doubled because it is necessary to connect to the FET switch in the substrate through a via to the side of the MTJ stack. However, fast

operation is obtained, since there is then generally enough silicon area in the larger cell to implement a high-conductance FET switch.

A second type of cross-point architecture with the thin-film diode is shown in Figure I.2(c) [*Ref. I.18*, *Ref. I.19*]. In this case, to avoid sneak paths during write operations, the resistance value must be large. Then, during the read operation, all lines in the entire array are carefully biased so that current flows preferentially through just one device. The signal is weak because of the large resistance and sneak current paths, so sensing is slow, but the very high density of the cross-point arrangement is maintained. Moreover, since the substrate is not involved in the cells, it is conceptually possible to stack layers of cells.

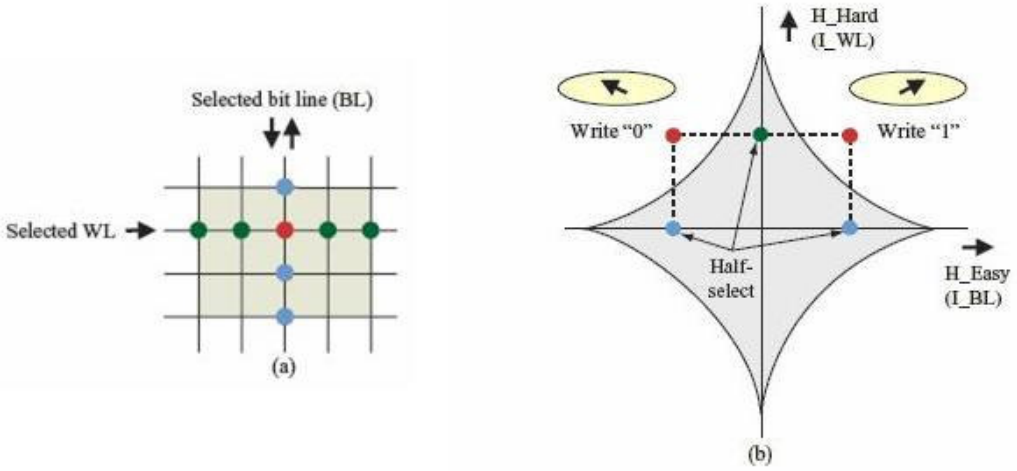

Figure I.3 Coincident field selection for writing a magnetic element of an MRAM. (a) Schematic of array with colored dots indicating the selected (red) and half-selected (blue and green) bits. (b) Switching threshold (astroid) curve with appropriate field values indicated for the write operation and with magnetization orientation fields. Part (b) The ellipses show the direction of the shape anisotropy of the free magnetic layers of the bits; the arrows inside the ellipses indicate the orientations of the free-layer magnetization.

In all cases, the MRAM write operation is done by a coincidence of x- and y-currents, and these are easiest to control if the lines supplying these are isolated, as for the architectures of Figure I.2(a) and 2(b). In conventional MRAM, the write operation makes use of the stability boundary curve shown in part (b) of Figure I.3. The boundary astroid curve illustrated is that calculated for a single-domain model of the switching free layer, and is expressed as

I.1) $$H_x^{2/3} + H_y^{2/3} = H_i^{2/3}$$

where Hx and Hy are respectively the x and y fields, and H_i is the anisotropy field of the assumed single-domain magnetic element. This functional form is that of a mathematical curve called an astroid, but in the MRAM field the term has generally taken on the meaning of the experimentally obtained switching boundary, which in the best cases only approximates a true mathematical astroid curve. For field excursions that remain inside the astroid curve, the element is magnetically stable, pointing either to the left or to the right. For field excursions that go outside the astroid curve, the element is written to one definite state. Many of the largest challenges of MRAM are associated with controlling the write operation, particularly with ensuring that none of the write operations cause an undesired switching event in any of the half-selected bits, see Figure I.3(a). Without a carefully balanced pinned layer structure the astroids can be offset to the right or left. In addition, the element shapes are not perfectly uniform in size, causing the astroid sizes and shapes to vary. Finally, it turns out that the energy barrier that separates the two stable states vanishes as the write field approaches the astroid boundary. Thus, there is a non-negligible probability of the magnetization spontaneously switching by a thermally activated process [*Ref. I.20*]. A more advanced ‘‘toggle’’ MRAM write architecture was later introduced by Motorola for a bilayer storage film [*Ref. I.21*].

A generic view on MRAM characteristics concludes our discussion. Table I.3 compares embedded SRAM, DRAM, and Flash (NOR Flash) with estimated embedded MRAM for cost, performance, power, and write endurance.

Category	*Parameter*	*SRAM*	*DRAM*	*NOR Flash*	*MRAM*
Cost	Cell area	3.7 μm^2	0.56 μm^2	0.5 μm^2	0.7–1.4 μm^2
	Process cost adder	0%	25%	25%	25%
Performance	Read access	3.3 ns	13 ns	13 ns	5–20 ns
	Write cycle	3.4 ns	20 ns	5 μs	5–20 ns
Power	Data retention	0.6 nA per bit at 85°C	0.2 nA per bit at 85°C	0	0
	Read active	15 pC per bit	7 pC per bit	30 pC per bit	7 pC per bit
	Write active	15 pC per bit	7 pC per bit	30 nC per bit	45 pC per bit
Miscellaneous	Write endurance	Unlimited	Unlimited	10^5 cycles	Unlimited

Table I.3 Typical or estimated parameter values for a variety of embedded memory technologies at the 180-nm technology node. Entries in color indicate areas in which embedded MRAM is expected to have a significant advantage. Data from Ref. I.16.

In summary, among the best attributes of MRAM are zero data-retention power, very low standby power, unlimited write endurance, and relatively high speed. Low standby power can be achieved because MRAM has no array leakages (all voltages are zero in an MRAM array in standby), few reference currents, and no pumped supplies that must be maintained. Read-active power is good and is comparable to that for embedded DRAM. Write-active power is high compared to that for embedded SRAM and DRAM, but much lower than for embedded Flash. Read performance is comparable to that of embedded Flash and DRAM, but slower than for embedded SRAM. And finally, write-cycle time is comparable to that of embedded DRAM and slower than that of embedded SRAM, but much faster than that of embedded Flash.

The choice of which embedded memory technology to use depends on the intended application. In some cases the application attributes dictate clear choices. An application would select embedded MRAM if it most valued nonvolatility and low standby power; otherwise, embedded SRAM and DRAM could be used. If embedded MRAM were at a comparable state of maturity, it would present a choice that could offer the tradeoff of a larger write power vs. lower power for data retention and standby operation. Depending on the application, this could be an attractive tradeoff. The issue for MRAM is that it is not yet at a comparable state of maturity that allows these comparisons to be real options.

I.2. A Lab-On-A-Chip application: the detection of magnetic microbeads in biosensors

Although magnetic sensing has been applied to biological diagnostics in the past, the sensors used have limited the deployment of such systems due to their size and power constraints. Now solid state magnetic sensors promise to change this picture by facilitation miniaturized magnetic sensor based systems. The applications include detection of the small magnetic fields created by nerve impulses for monitoring the activity of the heart and brain. The previously insurmountable barrier to the use of solid state magnetic sensors, sensitivity, is being overcome by sensors utilizing GMR materials and MTJ.

Magnetic particles have been used for many years in biological assays. These particles range in size from few nanometers up to a few microns, and in composition from pure ferrite to small percentages of ferrite encapsulated in plastic or ceramic spheres. The beads are coated with a chemical or biological species such as DNA or antibodies that selectively binds to the target.

The selectivity of sample and target can be used as a rapid sensitive detection strategy with the integration of a magnetic detector. This integration is facilitated by the development of solid-state GMR sensors. These sensors have the advantage of being compatible with silicon integrated circuit fabrication technology resulting in a single detector, or even multiple detectors, that can be made on a single chip along with any of the required electrical circuitry. Results from theoretical modeling, as well as laboratory results, show that GMR detectors can resolve single micrometer-sized magnetic beads.

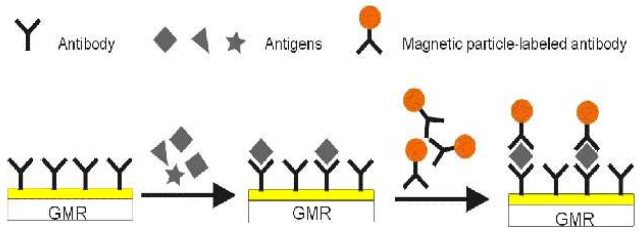

Figure I.4 Antigens are detected by flowing them over a sensor coated with antibodies to which they bind. The magnetic particle-labelled antibodies then bind to the antigens providing a magnetic indication of the presence of those antigens.

Small magnetic beads, coated with a material that binds to the biological molecules to be analyzed are allowed to settle on a substrate that is selectively coated in different areas with substances that

bond to specific molecules of interest. After removing the beads that are not bonded to the substrate via a molecule of interest, the presence of the remaining magnetic microbeads is detected by magnetic sensors in the array [*Ref. I.22*]. Figure I.4 schematically shows the bonding of the beads to the sites via the molecules to be detected. Several bioassays can be simultaneously accomplished using an array of magnetic sensors, each with a substance that bonds to a different biological molecule. This application requires extremely small, low-power, lowfield magnetic sensors.

Efforts in this direction have been made by Rife et al. [*Ref. I.23*] They are developing a biosensor system, the Bead Array Counter (BARC), based on the capture and detection of micron-sized, paramagnetic beads on a chip containing an array of GMR sensors [*Ref. I.22 - Ref. I.28*], see Figure I.5.

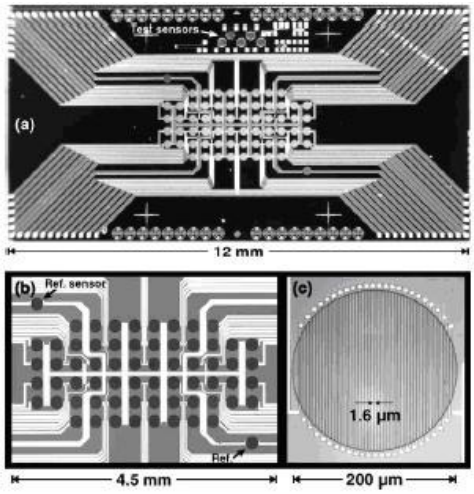

Figure I.5 Optical micrographs of a BARC-III sensor chip. (a) The 68 pin-out chip, including a central sensing area with 64 sensors and two reference sensors, and a number of test structures. (b) Closer view of the central sensing area. (c) Close-up of one serpentine GMR sensor trace encompassing a 200 _m-diameter sensing zone. [Ref. I.23].

They designed and characterized micromagnetic performance of a larger chip with 64 sensor zones (BARC-III). BARC-III chip includes 64 individually addressable GMR sensors and two reference sensors with 68 pin-outs. Each sensor is a serpentine resistor trace 1.6μm wide on a 4.0μm pitch, with a total length of 8mm within a 200μm -diameter circular zone, increasing the active area per biomolecular spot by quite 10 times. The BARC-III sensors are composed of a multilayer GMR material [*Ref. I.30*] with a larger saturation field and GMR effect, ~30mT and ~15%, respectively. The overall structure of each sensor is illustrated in cross-section in Figure I.6.

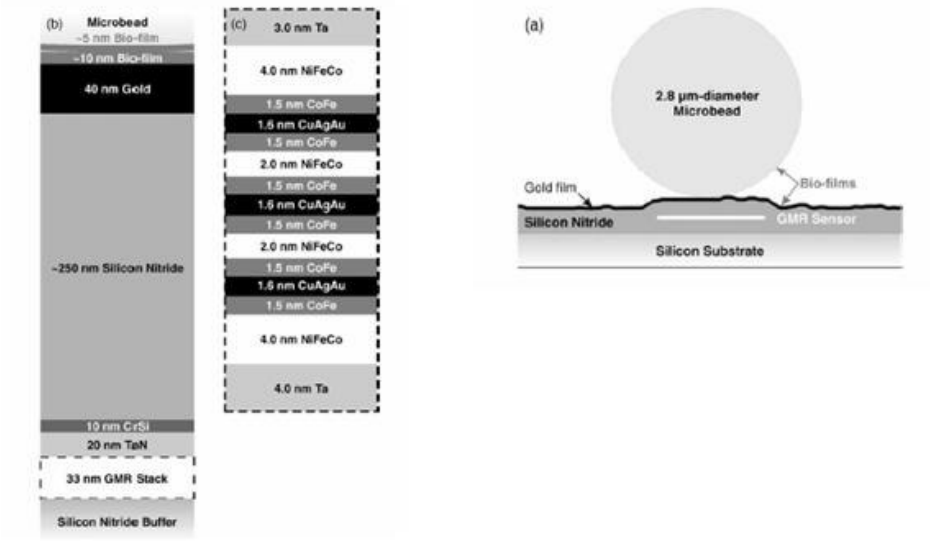

Figure I.6 Cross-sectional, scale illustration of (a) the bead/sensor chip geometry; (b) the multilayer chip design; and (c) the films comprising the GMR stack.[Ref. I.23].

The basic GMR film structure includes four ferromagnetic layers interspersed with three non-ferromagnetic layers. Antiferromagnetic exchange coupling generates the alternating, opposing magnetizations required for the GMR effect. The ferromagnetic layers have three sub-layers, composed of an internal layer of NiFeCo (chosen for its good linearity and low hysteresis with relatively high magnetic polarization), sandwiched between two thin films of CoFe (to maximize the magnetoresistance of the overall structure).

BARC-III chips is covered with a silicon nitride passivation layer in order to protect the circuitry from the corrosive and conductive biochemical reagents. However, the presence of this layer is detrimental to sensor performance because of the strong dependence of the GMR signal on the distance of the bead from the sensor (as will be reviewed below). For this reason the passivation layer has been reduced to 250*nm* thick. As beads, commercial paramagnetic particles Dynal M-280 [*Ref. I.22*] beads are used. These 2.8μm-diameter beads are composed of magnetic γ-Fe_2O_3 and Fe_3O_4 nanoparticles (<20 nm in diameter) dispersed in a polymer matrix [*Ref. I.31*, *Ref. I.32*]. The nanoparticles within these beads are often described as superparamagnetic; that is, they are small enough that the ambient thermal energy is greater than the magnetic alignment energy, so they spontaneously demagnetize at room temperature.

Although Dynal M-280 microbeads have excellent biocompatible surface properties, their magnetic properties are not optimal, having a relatively low saturation magnetization, the magnetic content

among beads varies widely (with a standard deviation of 72%), and some beads are non-magnetic [*Ref. I.22*]. Rife team have focused on NiFe ($Ni_{30}Fe_{70}$) beads produced by an industrial carbonyl process because of their superior magnetic moment [*Ref. I.26*, *Ref. I.33*]. Because of this property, smaller solid ferromagnetic beads could effectively be used as biomagnetic labels, which would increase the dynamic range of biosensor assays.

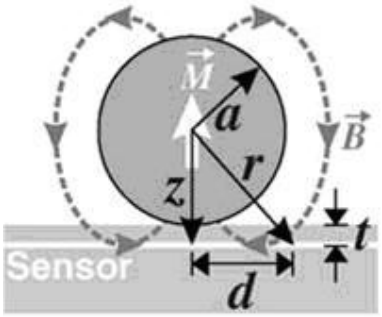

Figure I.7 Illustration of the micromagnetics of a paramagnetic bead under an applied field (in the direction of M). A cross-section of a bead of radius a on top of a sensor separated by an overlayer of thickness t. The dashed lines and arrows indicate the induced magnetic field.

The electronic detection of magnetic microbeads on BARC GMR sensors [*Ref. I.22*, *Ref. I.26*] can be summarized as follows. An external ac magnetic field, H_z , is applied normal to the chip (the *z*-direction). As illustrated in Figure I.7, an individual bead, magnetized by the external field and resting on the surface above the GMR resistor trace, generates an ac local dipole field, *B*, with planar components sufficient to cause a magnetoresistance change. The ac change in resistance, $\Delta R/R$, generates an ac voltage change across a dc-biased Wheatstone bridge. The bridge voltage signal is filtered to remove the dc component, amplified 1000 times or more, and detected by a lock-in amplifier synchronized with the applied ac magnetic field. The overall GMR signal for a sensor, $\Delta R/R$, is determined by sensor geometry and the cumulative local magnetoresistance changes associated with individual microbeads. For the weak fields expected from the microbeads, the local magnetoresistance change depends primarily on the strength of the field oriented along the trace or sensing axis, *Bx*. It is only this component of the planar field that is of interest. For a bead of magnetization *M* and radius *a* separated from the GMR trace by an overlayer of thickness *t*, the field *Bx* at a distance *d* along the trace and relative to the center of the bead is given by

I.2) $$B_x = \mu_0 M \frac{a^3 (a+t) d}{\left((a+t)^2 + d^2\right)^{5/2}}$$

This field has a maximum value

I.3) $$B_{x,mzx} = 3.6 \frac{\mu_0}{4\pi} \frac{M}{\left(1 + (t/a)\right)^3}$$

that occurs at a distance $d = (a + t)/2$ along the trace. The rms ac bridge voltage expected for a single bead centered over a sensor trace can be approximated as

I.4) $$\Delta V \approx 1.14 V_{dc} C_0 \left(\frac{a^2}{wL}\right)\left(\frac{\mu_0}{4\pi}\right)^2 \frac{M_{max}^2}{\left(1 + (t/a)\right)^6}$$

The Wheatstone bridge signal results in the range of $19 \div 22 nV$ for Dynal M-280 microbeads and $0.72 \div 1.2 \mu V$ for $Ni_{30}Fe_{70}$ beads of $2.8 \mu m$ diameter, demonstrating the enhanced sensitivity of the system by the use of ferromagnetic beads.

Although other approaches may generate larger S/N for smaller particles, BARC-III sensors combined with NiFe microbeads have the largest potential sensitivity assuming passive delivery of target molecules to the sensor. Small, highly sensitive microsensors will ultimately have the advantage if high density arrays can be integrated and multiplexed on a chip. Moreover, the overall sensitivity of any of these schemes would be enhanced if target biomolecules can be *actively* directed to the sensing zones; for example, by magnetic, fluidic, or electrochemical forces.

The recent progress in the area of microfluidics and Lab-On-A-Chip-type devices make possible the developing of more gentle protocols and affordable instruments for specific blood analysis tasks. The use of physical fields for the separation of cells takes advantage of the heterogeneity of physical properties of the blood cells. After exposure to fields of different nature, differences in size, density, electrical permittivity, dielectric characteristics, or adhesiveness among cells can be revealed in the form of forces differentially acting on cells of a particular type. Populations of cells that share similar behaviour upon field exposure can then be differentially manipulated and eventually partitioned from the whole sample.

Small-scale implementation greatly favours on-chip field separation. Very strong fields can be created over small distances and small displacements on the scale of cell size can be used for effective separation. Even more important for cell separation, regardless of the nature of these

fields, is microscale control, which allows for the manipulation of single cells and particles in suspension, with the potential for extreme purity or efficiency of the separation. Since the principles of separation of particles from solutions by using fields were outlined by Giddings in 1991 [*Ref. I.34*], a variety of fields have been employed in small-scale applications. Previously, we fully discussed about microfabricated devices for cell separation using magnetic interactions by coupling magnetic beads. As further examples, we note microfabricated devices using mechanical forces or mechanical restriction of cell (dense array of posts [*Ref. I.35*], weir-type structure, array of narrow channels [*Ref. I.36*]), dielectrophoresis (DEP) that uses the electrical polarization of cells in non uniform electric fields to induce translational motion or reorientation of cells, affecting their dynamic behaviour [*Ref. I.37*, *Ref. I.38*, *Ref. I.39*], optical interaction and trapping based on microfluidic systems using a diode laser bar that permit a separation of cells based on their size [*Ref. I.40*] and biochemical interaction based on differences among cells that can be effectively used to selectively destroy some cell subpopulations after uniform exposure of the whole sample to a selectively toxic environment [*Ref. I.41*].

Lastly, as Lab-On-A-Chip devices become enabling tools for separation and analysis of small and homogenous subpopulations of cells precisely and without altering their state, new possibilities open for diagnostic applications and treatment.

I.3. Magnetoresistive sensors for Non Destructive Evaluation

Increased research activity on nondestructive testing has been motivated by the need for precise evaluation of cracks and flaws for the assessment of the expected life of mechanical components. Along with a variety of methods that include dye penetrants, X-ray, and ultrasonic testing, eddy-current testing (ECT) is also commonly used for detecting defects such as fatigue cracks, inclusions, etc., in conductive materials. Eddy currents are induced in a specimen as a result of the application of an alternating magnetic field. In the presence of defects, which act as a high resistance barrier, the eddy-current flow is perturbed. As a result of this defect, a "leakage" magnetic field is produced. Such field perturbations are usually detected as an impedance change in the exciting coil [*Ref. I.42*].

In recent years, electromagnetic methods for eddy-current inspection have attracted increasing attention. Electromagnetic sensors, based on either Hall effect, anisotropic magnetoresistance (AMR) [*Ref. I.43*, *Ref. I.44*], giant magnetoresistance (GMR) effect [*Ref. I.45*, *Ref. I.46*], or SQUID have been successfully used for crack detection. In the last fifteen years, the high-T_C SQUID represented an alternative eddy current sensor. Thanks its high magnetic field sensitivity and its ability to function down to zero frequency it can detect much deeper defect than traditional eddy-current sensors. Moreover, the wide dynamic range enables the SQUID to maintain its high sensitivity in the presence of strong dc or noise fields so that it is possible to monitor also the very low magnetic field variations induced in last generation materials, as Carbon Fibre Reinforced Polymer (CFRP) and Fiber/Metal Laminates (FMLs) [*Ref. I.47-Ref. I.53*]. There are few disadvantage in using SQUIDs, in fact, since the SQUID is a superconductive device it is necessary to manipulate cryogenic liquid, generally LN_2, therefore skilled personnel is needed, and its very expensive costs.

Among the magnetoresistive sensors, GMR and AMR sensors, offer a good tradeoff in terms of performance versus cost. They have small dimensions, high sensitivity over a broad range of frequency (from hertz to megahertz domains), low noise, operate at room temperature, and are inexpensive. Although their sensitivities are comparable, GMR sensors have better directional property than AMR sensors. Both types of sensors detect the component of the magnetic field vector along their sensitive axis. In the case of GMR sensors, fields applied perpendicularly to the sensitive axis have negligible effect on their output. In contrast, the sensitivity of AMR-based probes is lowered by a field perpendicular to the sensitive axis, which, at high values, can even "flip" the sensor response [*Ref. I.43*]. This property is particularly important in the coil–crack

interaction problems, where the electromagnetic field has a complex three-dimensional (3-D) geometry. The directional property of GMR sensor can be used in a difficult problem encountered in NDE, detection of edge cracks [*Ref. I.46*]. It is shown that, by properly orienting the sensitive axis, the probe will be insensitive to the edge. Additionally, the presence of the edge enhances the sensitivity and resolution of the GMR probe to cracks initiating perpendicular to this edge.

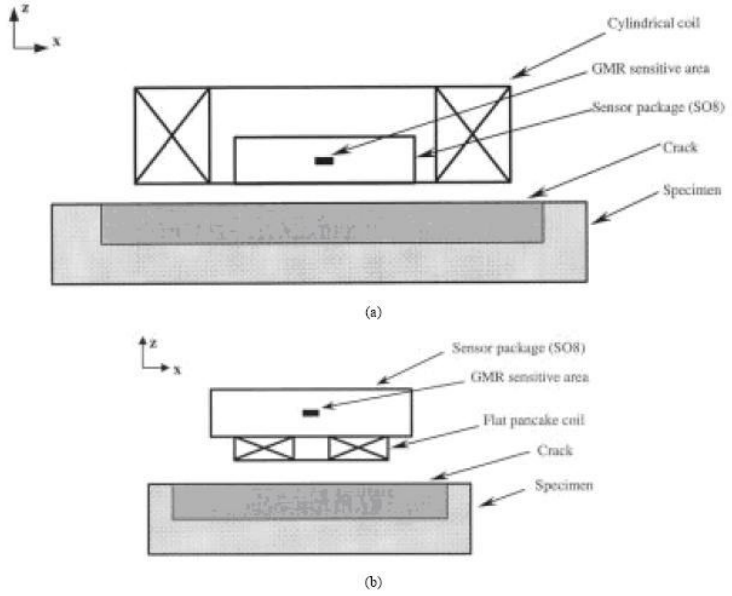

Figure I.8 Schematic diagram indicating probe assembly and coordinate system. (a) Cross section of the probe assembly utilizing a cylindrical coil surrounding the sensor. (b) Cross section of the probe assembly with flat coil placed on the sensor package.

The main components of the eddy-current probes comprise either a relatively large cylindrical coil or a flat spiral "pancake- type" coil with the GMR sensor located on the coil axis. Probe geometry is shown in Figure I.8(a) and (b), while dimensions of the coils generally used are about 6mm till 3mm. The GMR sensor consists of four thin-film resistors in a Wheatstone bridge configuration with two of them being magnetically shielded and acting as dummy resistors. The sensing axis of the GMR probe is coplanar with the surface of the specimen. The excitation field on the coil axis, being perpendicular to the sensing axis of the GMR films, has no effect on the sensor. In a defect-free specimen, because of the circular symmetry of the induced eddy currents, these will produce no effect on the sensor output. In the presence of a defect, output signal from the sensor is produced only by the perturbation of the eddy-current flow path. A sinusoidal current source provides a current through the coil of controlled amplitude (till 3 A) and frequency (between 1 and 100 kHz).

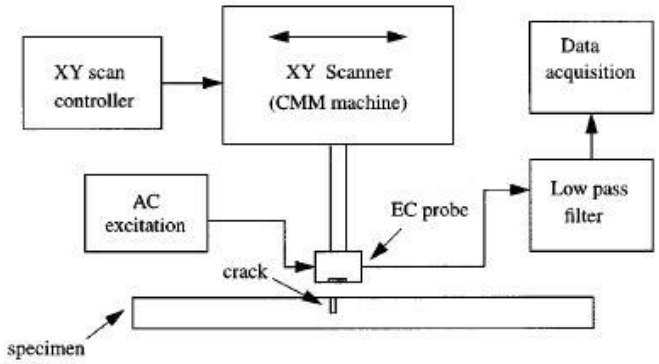

Figure I.9 Block diagram of experimental setup for scanning of specimens containing geometric flaws. [Ref. I.54].

A schematic diagram of the experimental setup is shown in Figure I.9. The system was developed [*Ref. I.54*] to assess the feasibility of the GMR eddy-current probe as an effective flaw detector. Various calibrated defects were machined into the surface of an aluminum plate by using end-milling cutters. As example demonstrating the possibilities of GMR based non destructive technique, the results on aluminium plate having cracks of fixed length (15 mm) and width (0.5 mm) but varying depths are reported. The map obtained, Figure I.10, shows two symmetrical peaks that are located on each side of the crack. In this figure it is noticed that, besides the central maxima at either side of the crack, each peak has two shoulders. Locating these shoulders at the points that correspond to the minimum magnitude of the output slope, it is observed, for this particular case, that the distance between these coincides with the length of the crack.

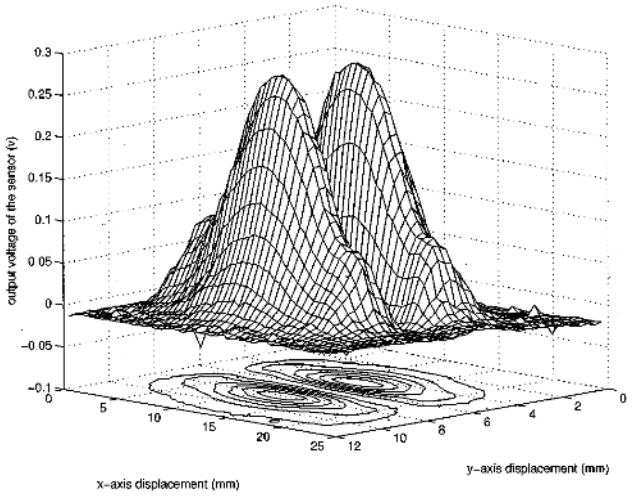

Figure I.10 Output from eddy-current sensor scanning a crack of length 15 mm and depth 2 mm with sensing axis perpendicular to crack orientation. Map showing magnitude and contours of sensor output. [Ref. I.54].

The showed results are restricted to aluminium plate sample.

Notwithstanding, when eddy current technique is applied to a composite, it shows a reduction of sensitivity to detect deep flaws because of the low electrical conductivity of such materials and high sensitivity of the coil to lift off variation. In the following chapters, the discussion will be focalized on theory, models and simulations that can be used to improve the GMR sensitivity and the measurement technique in an unshielded environment to make it a possible measurement technique for materials characterized by a very low electrical conductivity.

References

Ref. I.1 T. Miyazaki, Spintronics, 2004

Ref. I.2 M.N. Baibich et al., Phys.Rev.Lett 61, 2472 (1988)

Ref. I.3 T. Miyazaki and N. Tezuka, J.Magn.Magn.Mater. 139, L231(1995)

Ref. I.4 L.J. Schwee, IEEE Trans. On Magn 8, 405 (1972)

Ref. I.5 G.B Graley, J.M. Daughton, A.V. Pohm, C.S. Comstock, IEEE Trans. On Magn 27, 5517 (1991)

Ref. I.6 K.T.M. Ranmuthu, I.W. Ranmuthu, A.V. Pohm, C.S. Comstock, IEEE Trans. On Magn 28, 2359 (1992)

Ref. I.7 A.V. Pohm, J.M. Daughton, K.E. Spears, IEEE Trans. On Magn 28, 2356 (1992)

Ref. I.8 T. Miyazaki, T. Yaoi, S. Ishio, J.Magn.Magn.Mater. 98, L7-L9(1991)

Ref. I.9 T. Yaoi, S. Ishio, T. Miyazaki, IEEE Trans. On Magn Jpn 8, 498-504(1993)

Ref. I.10 J.S. Moodera, L. R. Kinder, T. M. Wong, and R. Meservey, Phys. Rev. Lett. 74, No. 16, 3273–3276 (1995)

Ref. I.11 R.E. Scheuerlein et al, Proc of ISSCC 2000, p.128, (2000)

Ref. I.12 M. Durlam et al., Proc of ISSCC 2000, p.130, (2000)

Ref. I.13 M. Durlam et al., Tech. Dig. of International Electron Device Meeting 2000, p.995

Ref. I.14 S. Tahara et al., Abstract of the Integrated Circuits and Devices (2003)

Ref. I.15 Z.G. Wang, Y. Nakamura, IEEE Trans. On Magn. 32, 4022 (1996)

Ref. I.16 W.J. Gallagher and S. S. P. Parkin, IBM J. Res. Develop. Vol. 50 no. 1 January 2006

Ref. I.17 R.E. Scheuerlein Proocedings of the 70th Biennial IEEE International Nonvolatile Memory Tech. Conf. (1998)

Ref. I.18 F.Z Wang, Appl. Phys.Lett. 77, 2036-2038 (2000)

Ref. I.19 W. Reoh et al., IEEE Circuits and Devices Mag. 18, 5, 17-27 (2002)

Ref. I.20 N.D. Rizzo et al., Appl. Phys.Lett. 80, 13, 2335-2337 (2002)

Ref. I.21 M. Durlam et al., IEDM Tech. Digest, pp. 34.6.1-34.6.3

Ref. I.22 D.R. Balset, G.U. Lee et. Al, Biosensor and Bioelectronics, vol 13, 731-739 (1998)

Ref. I.23 J.C. Rife et al., Sensors and Actuators A 107 209-218 (2003)

Ref. I.24 D.R. Baselt, Biosensor using magnetically detectable label, US Patent 5, 981, 297 (9 November 1999).

Ref. I.25 R.L. Edelstein et al., Biosensor and Bioelectronics. 14, 805–813 (2000)

Ref. I.26 M.M. Miller et al., J. Magn. Magn. Mater. 225, 138–144 (2001)

Ref. I.27 C.R. Tamanaha, L.J. Whitman, R.J. Colton, J. Micromech. Microeng. 12, N7–N17 (2002)

Ref. I.28 P.E. Sheehan, R.L. Edelstein et al., Biosensor and Bioelectronics. 18, 1455–1459 (2003)

Ref. I.29 U. Hardman (Ed.), Magnetic Thin Film and Multilayer Systems::Physics, Analysis, and Industrial Applications, Springer, Berlin, 1996.

Ref. I.30 J.B.J. Daughton, R. Beech, A. Pohm,W. Kude, IEEE T. Magn. 30, 4608–4610 (1994)

Ref. I.31 Dynal, Dynal Biotech, Oslo, Norway.

Ref. I.32 W.S. Prestvik et al., Scientific and Clinical Applications of Magnetic Carriers, Plenum Press, (1997)

Ref. I.33 S. Calvin, M.M. Miller, R. Goswami, S.F. Cheng, S.P. Mulvaney et al., J. Appl. Phys. 94, 778–783 (2003)

Ref. I.34 J.C. Giddings, B.N. Barman, M.K. Liu, ACS Symp. Ser. 464, 128–144 (1991)

Ref. I.35 P. Wilding et al., Anal. Biochem. 257(2), 95–100 (1998)

Ref. I.36 H. Mohame et al., IEEE Trans. Nanobiosci. 3(4), 251–256 (2004)

Ref. I.37 P.R.C. Gascoyne, J. Vykoukal, Electrophoresis 23(13), 1973–1983 (2002)

Ref. I.38 J.Voldman, M.L. Gray, M. Toner, M.A. Schmidt, Anal. Chem. 74 (16), 3984–3990 (2002)

Ref. I.39 B.H. Lapizco-Encinas, B.A. Simmons, E.B. Cummings, Y. Fintschenko, Anal. Chem. 76(6), 1571–1579 (2004)

Ref. I.40 R.W Applegate, J. Squier, T. Vestad, J. Oakey, D.W.M. Marr, Optics Express 12(19), 4390–4398 (2004)

Ref. I.41 P. Sethu, M. Anahtar, L.L. Moldawer, R.G. Tompkins, M. Toner, Anal. Chem. 76(21), 6247–6253 (2004)

Ref. I.42 S. K. Burke, J. Non-Destruct. Eval., vol. 7, pp. 35–41, (1988)

Ref. I.43 B. Lebrun, Y. Jayet, and J. C. Baboux, Mater. Eval., vol. 53, no. 11, pp. 1296–1300, (1995)

Ref. I.44 E. S. Boltz and T. C. Tiernan, Rev. Prog. Quant. Non-Destruct. Eval., vol. 17, pp. 1033–1038, (1998)

Ref. I.45 W.W.Ward, III and J. C. Moulder., vol. 17, pp. 291–298, (1998)

Ref. I.46 T. Dogaru and S. T. Smith., vol. 16, pp. 31–53, (2000)

Ref. I.47 W G Jenks, S S H Sadeghi and J P Wikswo Jr., J. Phys. D: Appl. Phys. 30, 293-323 (1997)

Ref. I.48 M.v. Kreutzbruck, M. Muck, U, Baby, C. Heiden, Proceeding of the 7th ECNDT, 46-52 (1998)

Ref. I.49 A. Ruosi, G. Peluso, G. Pepe, M. Valentino, Elettromagnetic Nondestructive Evaluation (II), R. Albanese et al (Eds.), IOS Press, pp 215-223 (1998)

Ref. I.50 M. Valentino, A. Ruosi, G.Pepe and G.Peluso, Physica C, 372-376 (2002)

Ref. I.51 A.Ruosi, M.Valentino, V. Lopresto, G.Caprino, Journal of composite Material 56, 141-149 (2002)

Ref. I.52 C. Bonavolontà, G. Peluso, G.P. Pepe, M. Valentino, EPJ 42, 491-496 (2004)

Ref. I.53 C. Bonavolontà, G. P. Pepe, G. Peluso, M. Valentino, G. Caprino and V. Lopresto, IEEE Trans. Appl. Superconductivity 15, N°2, 711-714 (2005)

Ref. I.54 T. Dogaru and S. T. Smith, IEEE Trans. On Magn 37, 5, September (2001)

II Giant Magnetoresistance effect: basics of theory

This chapter contains a brief review of the giant magnetoresistance (GMR) effect exhibited by magnetic multilayers, granular alloys, and related materials. Various and much different physical origins can be responsible of the effect in the different systems. By starting with the MR effect characterization, we covered a description of the phenomenon in terms of spin-dependent conduction and electronic band structure in magnetic multilayers.

Magnetoresistance (MR) is the change of electrical resistivity (ρ) due to an external magnetic field (H) [*Ref. II.1*, *Ref. II.2*]. Positive or negative MR refers to the increase or the decrease of resistivity with the magnetic field. In the Drude model of metals there is no MR. However, MR exists in all real metals, and the magnitude and behaviour of MR are different for various types of metals. Furthermore, the measured MR depends not only on the strength of the magnetic field, but also the direction of the magnetic field with respect to the current. For a wire sample with a current density (J), there are two possible orientations of H: longitudinal $H \parallel J$ and transverse $H \perp J$. Hence, there are two kinds of MR: $\Delta\rho_{\parallel} = \rho_{\parallel}(H) - \Delta\rho_{\parallel}(0)$ and $\Delta\rho_T = \rho_T(H) - \rho_T(0)$. For thin film specimens, where the current is usually in the film plane, MR can be measured with the field in three different directions: $\Delta\rho_{\parallel}$ (longitudinal, $H \parallel J$), $\Delta\rho_T$ (transverse, $H \perp J$) with an in-plane magnetic field and $\Delta\rho_{\perp}$ (perpendicular, $H \perp J$) with H perpendicular to the film plane [*Ref. II.3*]. In the next hints, the characteristics of MR in various materials at low temperatures have been summarized.

Ordinary magnetoresistance (OMR) arises from the effect of the Lorentz force on the electron trajectories due to the applied magnetic field (Figure II.1).

II.1) $$\mathrm{F} = \mathrm{eE} + e[\mathrm{v} \times \mathrm{B}]$$

where e denotes the carrier charge (for electrons e = −q, and for holes e = q and q = 1.6×10^{-19} C), **E** denotes the electric field, **v** the carrier velocity and **B** the magnetic induction. The first term on the right-hand side of eq.II.1 represents a Coulomb force and the second term is the Lorentz force law. For non degenerate semiconductors exposed to transverse electrical and magnetic fields (i.e. **E·B**= 0), the current transport equation for one type of carrier becomes:

II.2) $$\mathrm{J} = \mathrm{J}_0 + \mu_{\mathrm{H}}[\mathrm{J}_0 \times \mathrm{B}]$$

where **J** denotes the total current density and the term $\mathbf{J}_0 = \sigma\mathbf{E} - \mathrm{eD}\Delta\mathrm{n}$ is the current density due to the electric field and carrier-concentration gradient Δn only. The transport coefficients μ_{H} (the Hall mobility which has the sign of the corresponding charge-carrier), σ (the conductivity), and D (the diffusion coefficient) are determined by the carrier scattering processes and generally depend on the electric and magnetic fields.

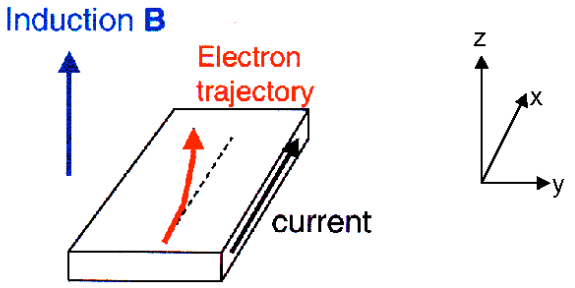

Figure II.1 Effect of the Lorentz force on the electrons trajectory when a magnetic field B is applied along the direction z perpendicular to the electric field E direction x.

A macroscopic and tangible consequence of the Hall field is the appearance of a measurable transverse voltage that is proportional to the magnetic field. This voltage is known as the *Hall voltage*, V_H, and can be calculated as:

II.3) $$V_H = -\mu_H B E_x w$$

where w denotes the strip width. By relating the Hall mobility in eq.II.3 to the current density, it is possible to express the Hall voltage as:

II.4) $$V_H = -R_H J_x B w$$

where $R_H = -\mu_H/\sigma = r/en$ denotes the Hall coefficient, r the Hall scattering factor of carriers and n is the carrier density. This indicates that low carrier-concentration produces a large Hall coefficient R_H, and explains why semiconductors are more useful here than metals are. The presence of the Hall field also results in inclination of the total electric field in the sample, with respect to the external field, by the *Hall angle* θ_H with $\tan\theta_H = E_z/E_x = -\mu_H B$.

Consider now the assumption of zero Hall electric field, $E_z = 0$. This condition is approximately realised by considering a short strip with wide cross-section. If an electric field $\boldsymbol{E}_{ex} = (Ex, 0, 0)$ is applied, as before, the current density given by eq.II.2 leads to another lateral component J_z, which produces a rotation of the current lines described by the ratio:

II.5) $$\frac{J_z}{J_x} = \mu H B = \tan\theta L$$

where θ_L is referred to as the carrier or Lorentz deflection angle. The longer carrier drift path brought by this deflection leads to the transversal geometric magnetoresistance effect:

II.6) $$\frac{\rho_B - \rho_0}{\rho_0} = (\mu_H B)^2$$

where ρ_0 denotes the electrical resistivity at $\boldsymbol{B} = 0$, and ρ_B the resistivity enhanced by the magnetic field. eq.II.6 shows that the relative change in resistivity increases with the square of the mobility-induction product. Hence this effect is very small for silicon. Sensors based on this effect require high-mobility III–V compounds such as InSb or InAs. Due to their low electron mobility, the geometrical magnetoresistivity in ordinary non-magnetic metals, such as Au, is quite small and has no practical importance (less than 1% in fields of the order of 1 Tesla). Nevertheless, both $\Delta\rho_{\parallel}$ and $\Delta\rho_T$ are positive with $\Delta\rho_T > \Delta\rho_{\parallel}$ and increase approximately as H^2 without saturation [*Ref. II.1*, *Ref. II.2*].

The anisotropic magnetoresistance (AMR) is a larger physical effect occurring in ferromagnetic transition metals and alloys [*Ref. II.4*, *Ref. II.5*]. In these materials the magnetisation vector determines the direction along which the current normally flows. The application of an external magnetic field rotates the magnetisation vector in the sample, and thus the current path, by an angle θ. The specific resistivity of the sample as a function of θ, $\rho(\theta)$, is given by:

II.7) $$\rho(\theta) = \rho_T + (\rho_{\parallel} - \rho_T)\cos^2\theta = \rho_T + \Delta\rho\cos^2\theta$$

where $\rho\|$ is the resistivity of the sample when $\theta = 0$, ρ_T the resistivity of the sample when $\theta = 90°$, θ being the angle between the internal magnetisation and the direction of the current, and the quotient $\Delta\rho/\rho_T$ is called the magnetoresistive effect.

In ferromagnetic metals (e.g., Fe, Co) and alloys (e.g., permalloy), substantial MR is observed. It is almost always the case that $\Delta\rho_{\parallel}$ is positive and $\Delta\rho_T$ is negative, as shown in Figure II.2(a), and $\rho_{\parallel} > \rho_T$, which is opposite to that of OMR. AMR originates from the spin-orbit interaction and causes the resistance to depend on the relative orientations of the magnetization and the electric current. The magnetic field range in which the AMR effect occurs is governed by the field needed

to change the direction of the magnetic moment. As result, both $\rho_{\parallel}$ and ρ_T are saturated under a modest field. For example, permalloy ($Ni_{80}Fe_{20}$) films, which are presently employed in sensor applications, exhibit the AMR effect of 1-2%, the resistance change taking place in a field range of a few Gauss [*Ref. II.6*].

Giant magnetoresistance (GMR) is one of the most fascinating discoveries in thin-film magnetism, which combines both technological potential and deep fundamental physics. In 1988, Baibich et al. discovered giant negative magnetoresistance in (001)Fe/(001)Cr multilayers in which the interlayer exchange interaction (J) causes antiferromagnetic alignment of adjacent Fe layers [*Ref. II.7*]. Like other magnetoresistive effects, GMR is the change in electrical resistance in response to an applied magnetic field. Baibich's group discovered that the application of a magnetic field to a Fe/Cr multilayer resulted in a significant reduction of the electrical resistance of the multilayer, in fact, the resistivity changed by as much as a factor of two. This effect was found to be much larger than either ordinary or anisotropic magnetoresistance and was, therefore, called "giant magnetoresistance" or GMR. Subsequently, such large effects and the intricate oscillations in MR, as caused by the oscillatory *J*, have been observed in a large variety of multilayers [*Ref. II.7*, *Ref. II.8*]. A similar, though diminished effect was discovered in Fe/Cr/Fe trilayers [*Ref. II.9- Ref. II.11*]. High magnetoresistance values can also be obtained in other magnetic multilayers, such as Co/Cu [*Ref. II.12- Ref. II.15*]. However, what distinguishes GMR from OMR and AMR is not just its magnitude, but also its being negative in all field directions: longitudinal, transverse and perpendicular. As shown in Figure II.2(b), $\rho_{\parallel} \approx \rho_T$, and the difference in $\rho_{\perp}$ is due to the demagnetizing factor associated with thin films. It should be mentioned that AMR is also present in systems exhibiting GMR. This is of particular concern in systems where the so-called GMRs are quite small (e.g., 5% at 5 K). In such cases, the value of the GMR is not known reliably unless measurements have been extended to more than one field orientations (especially $\rho_{\parallel}$) and that the AMR has been determined [*Ref. II.16*]. These negative GMRs have been observed only in the magnetic multilayer geometry, upon which many theoretical models are based [*Ref. II.17*, *Ref. II.18*]. Extensive results, both experimental [*Ref. II.19*] and theoretical [*Ref. II.20*], show that the oscillation periods of the MR depend on the specific crystalline orientation of the multilayers. These results seem to suggest that the intriguing GMR effects are intimately connected with the multilayer geometry.

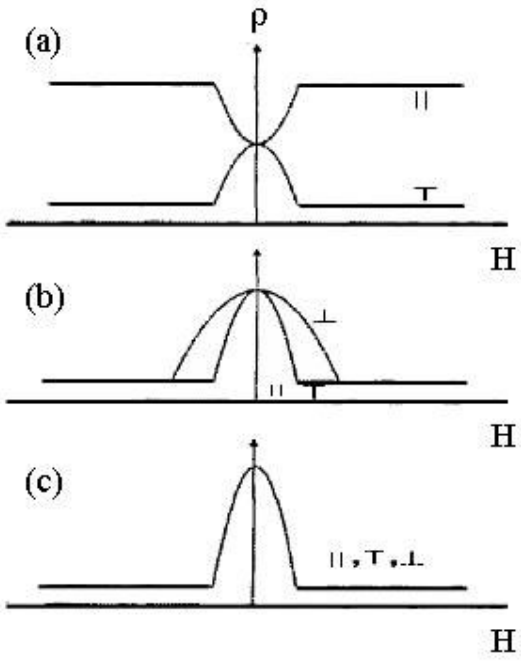

Figure II.2 Schematic representations of (a) anisotropic magnetoresistance in ferromagnetic alloys, and giant negative magnetoresistance in (b) multilayers, and (c) granular solids.[Ref. II.3].

Among the last spreading researches, there is GMR effect in granular Co-Cu alloys [*Ref. II.21*, *Ref. II.22*], and subsequently, in a number of other granular systems. Xiao et al. [*Ref. II.22*, *Ref. II.23*]further show that in granular systems, $\rho_{\perp} \approx \rho_{\parallel} = \rho_{T}$, as schematically shown in Figure II.2(c). In these materials, ferromagnetic precipitates are embedded in a non-magnetic host metal film. The randomly-oriented magnetic moments of the precipitates can be aligned by the applied magnetic field which results in a resistance drop.

II.1. Origin of GMR

GMR can be qualitatively understood using the Mott model, which was introduced as early as 1936 to explain the sudden increase in resistivity of ferromagnetic metals as they are heated above the Curie temperature. There are two main points proposed by Mott. First, the electrical conductivity in metals can be described in terms of two largely independent conducting channels, corresponding to the up-spin and down-spin electrons, which are distinguished according to the projection of their spins along the quantization axis. The probability of spin-flip scattering processes in metals is normally small as compared to the probability of the scattering processes in which the spin is conserved. This means that the up-spin and down-spin electrons do not mix over long distances and, therefore, the electrical conduction occurs in parallel for the two spin channels. Second, in ferromagnetic metals the scattering rates of the up-spin and down-spin electrons are quite different, whatever the nature of the scattering centers is. According to Mott, the electric current is primarily carried by electrons from the valence *sp* bands due to their low effective mass and high mobility. The *d* bands play an important role in providing final states for the scattering of the *sp* electrons. In ferromagnets the *d* bands are exchange-split, so that the density of states is not the same for the up-spin and down-spin electrons at the Fermi energy. The probability of scattering into these states is proportional to their density, so that the scattering rates are spin-dependent, i.e. are different for the two conduction channels. Although, as we will see below, this picture is too simplified in a view of the strong hybridization between the *sp* and *d* states, it forms a useful basis for a qualitative understanding of the spin-dependent conduction in transition metals.

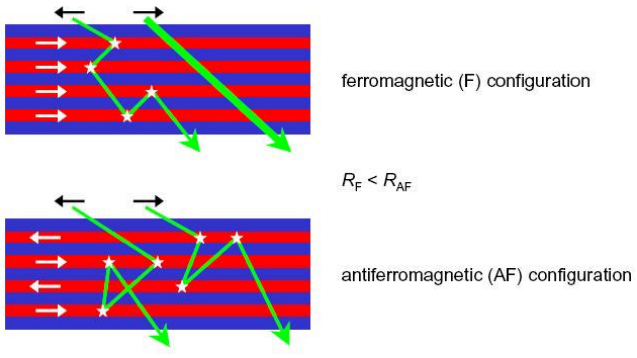

Figure II.3 Schematic illustration of electron transport in a multilayer for parallel and antiparallel magnetizations of the successive ferromagnetic layers. The magnetization directions are indicated by the arrows. The solid lines are individual electron trajectories within the two spin channels.

Figure II.3 shows the two collinear magnetic configurations assuming that the scattering is strong for electrons with spin antiparallel to the magnetization direction, and is weak for electrons with spin parallel to the magnetization direction. For the parallel aligned magnetic layers, the up-spin electrons pass through the structure almost without scattering, because their spin is parallel to the magnetization of the layers. On the contrary, the down-spin electrons are scattered strongly within both ferromagnetic layers, because their spin is antiparallel to the magnetization of the layers. Since conduction occurs in parallel for the two spin channels, the total resistivity of the multilayer is determined mainly by the highly-conductive up-spin electrons and appears to be low. For the antiparallel-aligned multilayer, both the up-spin and down-spin electrons are scattered strongly within one of the ferromagnetic layers, because within one of the layers the spin is antiparallel to the magnetization direction. Therefore, in this case the total resistivity of the multilayer is high. As it was originally suggested by Baibich *et al.*, [*Ref. II.7*] spin-dependent scattering is the primary origin of GMR.

II.2. Spin–dependent conduction

According to Mott's first argument, the conductivity of a metal is the sum of the independent conductivities for the up-spin and down-spin electrons:

II.8) $$\sigma = \sigma_{\uparrow} + \sigma_{\downarrow}$$

Within each conduction channel the conductivity is determined by various factors. In order to illustrate their role we use the Drude formula which can be expressed as follows:

II.9) $$\sigma_{Drude} = \frac{e^2 k_F^2}{\pi\hbar 6\pi}\lambda$$

Here σ_{Drude} is the Drude conductivity per spin, $e^2/\pi\hbar \approx 0.387\cdot 10^{-4}\ \Omega^{-1}$ is the spin conductance quantum, k_F is the Fermi momentum, and λ is the mean free path, which is the product of the relaxation time τ and the Fermi velocity v_F, i.e.

II.10) $$\lambda = v_F \tau$$

Although the Drude formula is valid only for free electrons, it is useful to understand qualitatively the factors affecting the spin-dependent conductivity. The conductivity is determined by the electrons which have the Fermi energy. Due to the Pauli exclusion principle the electrons which lie below the Fermi level can not gain energy responding to the small applied electric field, because all the states at higher energies are occupied. As a consequence, only electrons at the Fermi level can contribute to the electric current. As can be seen from eq.II.9, the conductivity is proportional to the cross sectional area of the Fermi surface $\approx k_F^2$, which characterizes the number of electrons contributing to the conduction. The mean free path depends on the Fermi velocity and relaxation time, the latter can be estimated from the Fermi rule

II.11) $$\tau^{-1} = \frac{2\pi}{\hbar}\left\langle V_{scatt}^2 \right\rangle n\left\langle E_F \right\rangle$$

where $\left\langle V_{scatt}^2 \right\rangle$ is an average value of the scattering potential and $n\left\langle E_F \right\rangle$ is the density of electronic states at the Fermi energy E_F for the appropriate spin.

Although all the quantities which enter expressions (II.8)-(II.11) are in general spin-dependent, the origin of the spin dependence is different. The Fermi momentum k_F and the Fermi velocity v_F are intrinsic properties of the metal and entirely determined by the electronic band structure of the metal. In ferromagnetic metals these quantities are different for the up- and down-spin electrons. The density of states at the Fermi energy $n\left\langle E_F \right\rangle$ is also determined by the spin-polarized band structure. On the contrary, the scattering potential which enters eq.II.11 is not an intrinsic property of the metal. It is generated by the scatterers such as defects, impurities, or lattice vibrations. The scattering potential can be either spin-dependent or spin-independent, which is determined by the particular mechanism of scattering. Spin-dependent scattering potentials might also contribute to GMR at the interfaces between ferromagnetic and non-magnetic layers. In real magnetic multilayers these interfaces are not ideal. Interfacial roughness and/or substitutional disorder (i.e. mixing of the adjacent metal atoms at the interface) are always present in experiments. Randomness of the atomic potentials at the interface results in enhanced interfacial scattering.

The relative importance of spin-dependent scattering potentials can, however, be diminished in real GMR structures which are far from being perfect. Various types of defects such as grain boundaries, stacking faults and misfit dislocations are always present in the multilayers. Because the relaxation time in eq.II.11 is determined by the *configurationally-averaged* value of the scattering potential squared, various types of scattering centers can make this average value spin-independent. In these circumstances the spin-polarized band structure of the multilayer becomes decisive and usually gives the dominant contribution to the spin dependence of the mean free path and the conductivity.

II.3. Role of band structure

The electronic band structure of the multilayer is probably the most important property which determines the spin-dependent conduction and consequently is responsible for the GMR. In most experiments on GMR the ferromagnetic 3*d* transition metals Co, Fe and Ni, and their alloys, such as permalloy $Ni_{80}Fe_{20}$, are used in combination with non-magnetic spacer layers, such as Cr or the noble metals Cu, Ag and Au.

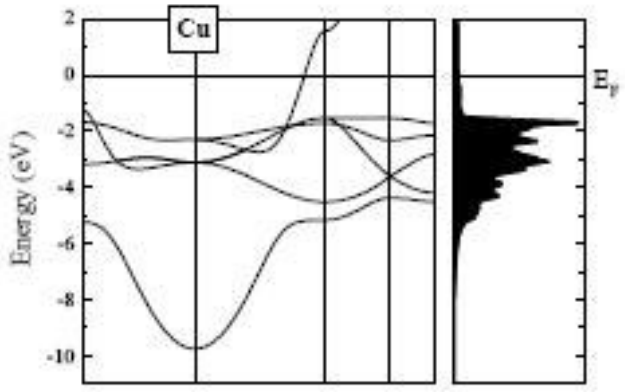

Figure II.4 Electronic band structures (left panel) and the density of states (right panel) of Cu. The band structure of non-magnetic Cu is same for the up-spin and down-spin electrons. It is characterized by the fully occupied d bands and the presence of a dispersive sp band at the Fermi energy, which result in high conductivity of Cu.

Due to the spin-orbit coupling of the 3*d* transition metals being very weak the electronic structure for the up-spin and down-spin electrons can be considered independently. The 3*d* elements are characterized by the presence of the 4*s*, 4*p* and 3*d* valence states, which are distinguished by their orbital momentum. The 4*s* and 4*p* states create a dispersive *sp* band which is similar to a free-electron band. The *sp* electrons have a high velocity, a low density of states and consequently a long mean free path, i.e. they may be thought to be mainly responsible for the conductivity in 3*d* metals. On the contrary, the *d* band is localized in a relatively narrow energy window and is characterized by a high density of states and a low velocity of electrons. In the interval of energy where the *sp* and *d* bands cross, they can not be considered as independent because of the strong *sp*-*d* hybridization, which modifies substantially the band structure. It changes dramatically the properties of the *sp*

electrons, which is reflected in the band bending and results in a reduced velocity associated with the *sp* band.

These features are evident from Figure II.4, in which the electronic band structure of Cu is shown. In ferromagnetic 3*d* metals the *d* band is exchange-split. Due to the localized nature of the *d* electrons, two *d* electrons experience a strong Coulomb repulsion provided that they have antiparallel spins and occupy the same orbital. To reduce the energy it is advantageous for the *d* electrons to have parallel-oriented spins, because the Pauli exclusion principle does not permit two electrons with the same spin to approach each other closely (i.e. occupy the same orbital) and hence the Coulomb interaction is reduced. Therefore, the Coulomb repulsion in conjunction with the Pauli principle leads to the ferromagnetic exchange interaction and favors the formation of a spontaneous magnetic moment. However, putting all the electrons into states with the same spin direction increases the total kinetic energy, the increase being larger the wider the *d* band or lower the *d*-band density of states. There are, therefore, two competing tendencies, which have to be balanced in order to find whether ferromagnetic ordering is favored. The condition which has to be satisfied for the appearance of ferromagnetism is the famous Stoner criterion $J_n(E_F)>1$, where J is the exchange constant (which takes the value of about $1eV$ for 3*d* transition metals) and $n(E_F)$ is the density of states for a given spin at the Fermi energy [*Ref. II.24*]. The Stoner criterion is satisfied for *bcc* Fe, *fcc* Co and *fcc* Ni. Due to the exchange splitting of the *d* bands, the number of occupied states is different for the up-spin and down spin electrons, giving rise to the non-zero magnetic moments of $2.2\mu_B$, 1.7 μ_B and 0.6 μ_B for Fe, Co and Ni respectively.

In order to distinguish between the high and low-occupied spin states, the terms 'majority-spin electrons' and 'minority-spin electrons' are usually used. The band structure of Co as a representative of the ferromagnetic 3*d* metals is shown in Figure II.5. The conductivity is determined by the position of the Fermi energy with respect to the *d* bands. In the case of Cu, the *d* bands are fully occupied and the Fermi level lies within the *sp* band (Figure II.4). Due to the high velocity of the electrons within the *sp* band and the low density of states with resultant low probability of scattering, the mean free path is long and Cu is a very good conductor. This is also the case for the other noble metals Ag and Au. On the other hand, in the case of a ferromagnetic metal like Co, as a result of the exchange splitting, the majority *d* band is fully occupied, whereas the *d* minority band is only partly occupied (Figure II.5).

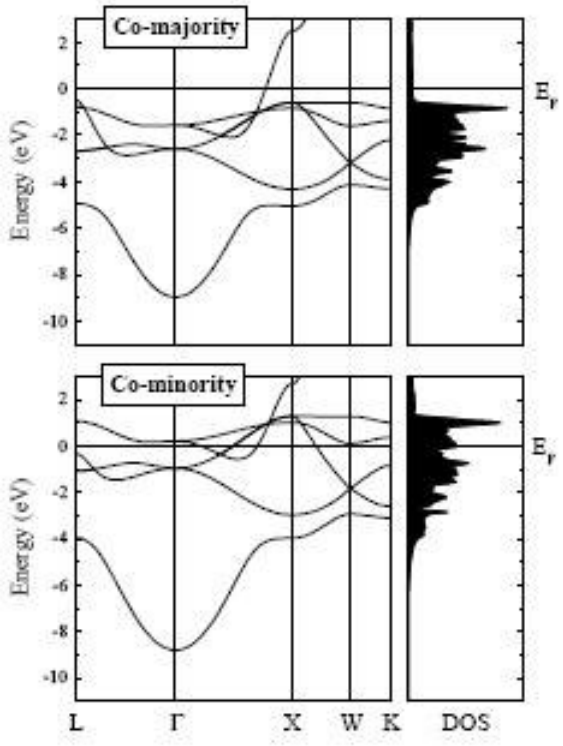

Figure II.5 Electronic band structures (down diagram) and the density of states (up diagram) of fcc Co for the majority-spin and minority-spin electrons. The electronic structure of ferromagnetic Co is different from Cu for the two spin orientations and is characterized by the exchange-split d bands. The Fermi level lies within the sp band for the majority-spin electrons, which leads to high conductivity of majority-spin channel. The Fermi level lies, however, within the d band for the minority-spin electrons resulting in low conductivity of the minority-spin channel. The sp electrons are strongly hybridized with the d electrons, which diminishes their contribution to conduction.

The Fermi level lies, therefore, within the *sp* band for the majority spins but within the *d* band for the minority spins. The exchange splitting of the spin bands leads to a crucial difference in the conductivity between the majority- and minority-spin electrons. For the majority spins the situation is similar to that in Cu: the conductivity is governed by the *sp* electrons and is high. On the contrary, the conductivity of the minority-spin electrons is not entirely determined by the *sp* electrons. Due to the strong *sp-d* hybridization which mixes the *sp* and *d* states the contributions of both the *sp* and *d* electrons become important. The minority bands represent hybridized *spd* bands which are not dispersive and have a high density of states. This makes the mean free path associated with these bands relatively short and the minority-spin conductivity low, despite a sizeable factor proportional to the area of the multiband Fermi surface. These arguments, which are based on the spin-polarized band structure, explain the strong spin asymmetry in the conductivity of bulk Co.

The presence of the interfaces in a magnetic multilayer adds a new important feature to our discussion above of spin-dependent transport in bulk elemental ferromagnets. The two adjacent metals creating the interface have different band structures, which lead to a potential step at the interface and results in the transmission probability across the interface being less than 1. If the interface separates ferromagnetic and non-magnetic metals the transmission will be spin-dependent due to the spin dependence of the band structure of the ferromagnetic layer. This can be illustrated by considering the band structures of Co and Cu, which are shown in Figure II.4 and Figure II.5. As is seen by comparing the figures, the band structure of Cu is similar to the band structure of the majority spins in Co. This good band matching implies a high transmission for the majority-spin electrons across the Co/Cu interface. On the contrary, there is a relatively large band mismatch between Cu and the minority spins in Co and consequently the transmission of the minority-spin electrons across the Co/Cu interface is expected to be poor. Therefore, the interfaces of the Co/Cu multilayer act as spin-filters. When the filters are aligned, the majority spin-electrons can pass through relatively easily. When the filters are antialigned, the electrons in both spin channels are reflected at one of the interfaces. This spin-dependent transmission is an important ingredient of the electronic transport in GMR structures.

Band matching also plays an important role in the spin-dependent interface scattering due to the intermixing of atoms near the interfaces. If we ignore the change in the chemical state of the atoms, i.e. assume that their atomic energy levels and magnetic moments are identical to those in the bulk of the adjacent layers, then the intermixing at the interface produces a random potential which is strongly spin-dependent. This spin dependence is a direct consequence of the good band matching for the majority spins in Co/Cu, which implies a small scattering potential, and the poor band matching for the minority spins in Co/Cu, which implies a large scattering potential. A similar behaviour takes place in Fe/Cr multilayers, where a very small scattering potential (good band matching) is expected for the minority-spin electrons, but a large scattering potential (bad band matching) is expected for the majority-spin electrons. Thus, the matching or mismatching of the bands between the ferromagnetic and nonmagnetic metals results in spin-dependent scattering potentials at disordered interfaces, which can contribute to GMR.

References

Ref. II.1 N.W. Ashcroft and N.D. Mermin, solid State Physics, Holt, Reinhart and Winston, New York, (1976)

Ref. II.2 P.L. Rossiter, The Electrical Resistivity of Metals and Alloys, Cambridge U. P., Cambridge, (1987)

Ref. II.3 C.L. Chien et al., J. Appl. Phys 73, 5309 (1993)

Ref. II.4 T.R. McGuire and R.I. Potter, IEEE Trans. Mag. MAG-11, 1018 (1975)

Ref. II.5 D.A. Thompson, IEEE Trans. Mag. MAG-11, 1039 (1975)

Ref. II.6 F.E. Shelledy and J.L. Nix, IEEE Trans. Mag. (1992)

Ref. II.7 M.N. Baibich et al., Phys.Rev.Lett 61, 2472 (1988)

Ref. II.8 W.P. Pratt Jr., S.F. Lee, J.M. Slaughter, R. Loloee, P.A. Schroader, J. Bass, Phys. Rev. Lett. 66, 3060 (1991)

Ref. II.9 G.Binash, P.Grünberg, F.Saurenbach, and W.Zinn, Phys.Rev.B 39, 4828 (1989)

Ref. II.10 W.H.Butler, X.-G.Zhang, D.M.C.Nicholson, and J.M.MacLaren, J.Magn.Magn.Mat. 151, 354 (1995)

Ref. II.11 E.Y.Tsymbal and D.G.Pettifor, J.Magn.Magn.Mat. 202, 163 (1999)

Ref. II.12 S.S.P.Parkin, Z.G.Li, and D.J.Smith, Appl.Phys.Lett. 58, 2710 (1991)

Ref. II.13 S.S.P.Parkin, R.Bharda, and K.P.Roche, Phys.Rev.Lett. 66, 2152 (1991)

Ref. II.14 H.Sato, T.Matsudai, W.Abdul-Razzaq, C.Fierz, and P.A.Schroeder, J.Phys.:Cond.Mat. 6, 6151 (1994)

Ref. II.15 R.Takatani, T.Dei, and Y.Sugita, J.Appl.Phys. 73, 6375 (1993)

Ref. II.16 A. Chaiken, G.A. Prinz and J.J. Krebs, J. Appl. Phys. 87, 4892 (1990)

Ref. II.17 R.E. Camley and J. Barnas, Phys. Rev. Lett. 63, 664 (1989)

Ref. II.18 P.M. Levy, S. Zhang, and A. Fert, Phys. Rev. I.ett. 65, 1643 (1990)

Ref. II.19 M.T. Johnson et al., Phys. Rev. Lett. 68, 2688 (1992)

Ref. II.20 P. Bruno and C. Chappert, Phys. Rev. Lett. 67, 1602 (1991)

Ref. II.21 A. Berkowitz et al., Phys. Rev. Lett. 68, 3745 (1992)

Ref. II.22 J.Q. Xiao, J.S. Jiang, and C.L. Chien, Phys. Rev. Lett. 68, 3749 (1992)

Ref. II.23 J.Q. Xiao, J.S. Jiang, and C.L. Chien, Phys.Rev.B 46, 9266 (1992)

Ref. II.24 E.C. Stoner, Proc. Royal Soc. A165, 372 (1938)

III Theoretical and experimental results

By starting with the main theoretical models which describe the GMR behaviour, the transport properties of magnetic multilayers will be estimated. The interlayer exchange coupling permits to reorient the magnetic moments of the ferromagnetic layers relative to one another. Thus, the relative magnetic moments oscillate between ferromagnetic and antiferromagnetic as a function of the thickness of the nonmagnetic layer. By choosing an appropriate thickness of the non-magnetic layer it is, therefore, possible to create an antiparallel configuration of the ferromagnetic layers and then align the moments by an applied magnetic field. In the meanwhile, the magnetic layer thickness dependence and the dependence by the number of bilayers are studied. In this study, our attention will be aimed above all to the semiclassical Boltzmann theory which permits to obtain macroscopic transport equations of magnetic multilayers for current perpendicular to the layers. These macroscopic equations will be used to extract, with the aid of numerical simulation, the GMR behaviour of a magnetic multilayer.

Physical insight into the origin of the current-in-the-plane (CIP) GMR can be obtained using the simple resistor model [*Ref. III.1,Ref. III.2*]. The series-resistor model can be generalized to include spin-dependent interface resistances, by adding additional resistors in the network. However, this model is a better approximation for the description of GMR within the current-perpendicular-to-the-plane (CPP) geometry [*Ref. III.3 -Ref. III.5*], infact, it is not able to provide a quantitative description of the CIP GMR even if it is useful as a starting point for understanding this phenomenon. For this reason it has often been used to obtain values of the spin-dependent bulk and interface resistances from CPP experimental data. However, the resistors model provides a simplistic and sufficient effect GMR. For an explanation of the physics involved is necessary to present some of the main theoretical models.

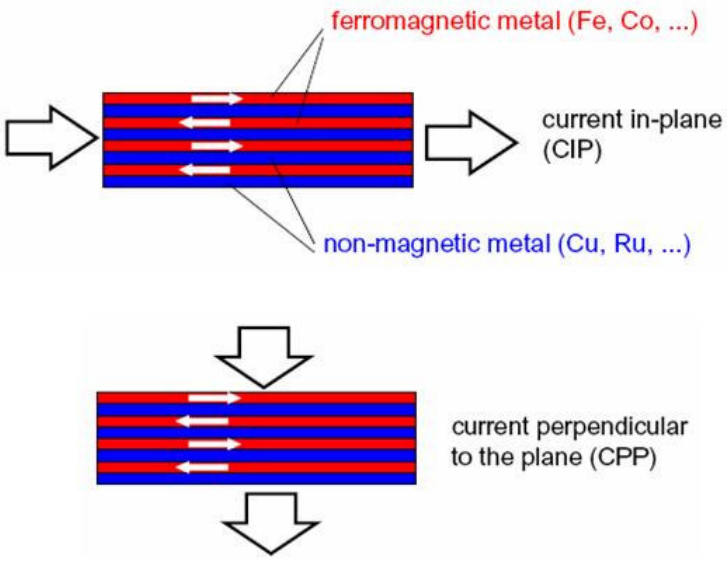

Figure III.1 Geometry for the CIP (up) and CPP (down) GMR. The arrow external to the multilayer indicate the current flow direction.

A large number of various theoretical models have been developed to describe GMR. These models differ mainly in the way that they treat the electronic structure and the electronic transport. The electronic structure can be described either within a simple free-electron approximation or within an accurate multiband approach. The main advantage of the free-electron theories is that they are physically more transparent and, though simple, can still capture some important physics of GMR. This is also the case for simple tight-binding models, which approximate the electronic structure by a single tight-binding band. Multiband models are, however, essential for a quantitative description of GMR. The electronic transport can be considered either within semiclassical Boltzmann theory

or within quantum-mechanical theory. The Boltzmann theory of transport is a versatile formalism, which has been widely used for treating GMR. It has been chosen as formalism for magnetic multilayers of practical interest because the subband energy splitting is comparable with the life-time broadening due to scattering. In these cases quantum-mechanical theory within a multiband treatment of the electronic structure is the best way to describe GMR.

Our attention will be aimed above all to the semiclassical Boltzmann theory which permits to obtain macroscopic transport equations of magnetic multilayers for current perpendicular to the layers (CPP). These macroscopic equations will be used to extract the GMR behaviour of an hypothetical magnetic multilayer.

III.1. Resistor model

According to the resistor model each metallic layer and each interface is treated as an independent resistor. Within each spin conduction channel the resistors are added in parallel or in series depending on the relationship between the mean free path and the layer thickness. If the mean free path is short compared to the layer thickness, $\lambda << d$, then each layer conducts the electric current independently and the resistors should be added in parallel. Under this circumstance the resistance of the parallel and antiparallel configurations are the same and consequently the GMR effect is zero. The above observation indicates that for obtaining non-zero GMR effect, the mean free path should be sufficiently long. This is consistent with the qualitative picture of GMR (the top panels of Figure III.2), which is based on the possibility for the electrons to propagate across the spacer layer freely, sensing the magnetizations of the two consecutive ferromagnetic layers. In the limit of mean free path being long compared to the layer thickness, $\lambda >> d$, the probability of scattering within the multilayer is the sum of scattering probabilities within each layer and each interface. Therefore, within a given spin channel the total resistance is the sum of resistances of each layer and each interface, i.e. the resistors are connected in series. In order to build up the resistor network for the multilayer, we consider a unit cell consisting of four layers, two ferromagnetic and two non-magnetic, as is shown in the top panels of Figure III.2 a and b.

Usually, the global spin-quantization axis has been chosen collinear to the magnetization directions. Within each ferromagnetic layer the electron spin can be either parallel or antiparallel to the magnetization direction. In the former case the electron is locally a majority-spin electron and in the latter case a minority-spin electron. The majority- and minority-spin resistivities of the ferromagnetic layer are different and are equal to $\rho_{\uparrow}$ and $\rho_{\downarrow}$ respectively. The resistance of the bilayer, which consists of the ferromagnetic layer (FM is for ferromagnetic metal) and the spacer layer (NM is for normal metal), for either of the two spin channels is equal to

III.1) $$R_{\uparrow,\downarrow} = \rho_{NM} d_{NM} + \rho_{\uparrow,\downarrow} d_{FM}$$

where ρ_{NM} and d_{NM} denote the resistivity and the thickness of the non-magnetic spacer layer and d_{NM} is the thickness of the ferromagnetic layer. For simplicity the interface resistance between the ferromagnetic and spacer layers has been omitted.

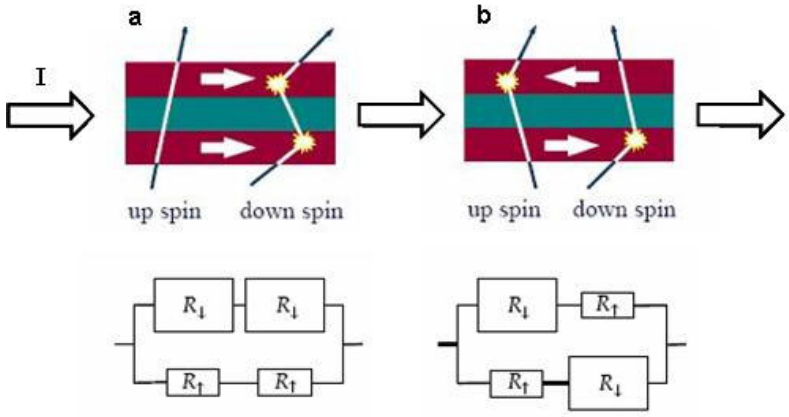

Figure III.2 Schematic illustration of electron transport in a multilayer for parallel (a) and antiparallel (b) magnetizations of the successive ferromagnetic layers. The magnetization directions are indicated by the arrows. The solid lines are individual electron trajectories within the two spin channels. It is assumed that the mean free path is much longer than the layer thicknesses and the net electric current flows in the plane of the layers. Bottom panels show the resistor network within the two-current series resistor model. For the parallel-aligned multilayer (a), the up-spin electrons pass through the structure almost without scattering, whereas the down-spin electrons are scattered strongly within both ferromagnetic layers. Since conduction occurs in parallel for the two spin channels, the total resistivity of the multilayer is low. For the antiparallel-aligned multilayer (b), both the up-spin and downspin electrons are scattered strongly within one of the ferromagnetic layers, and the total resistivity of the multilayer is high.

Using the resistances which are defined by eq.III.1 the equivalent network of resistors for the parallel and antiparallel magnetizations are shown in the bottom panels of Figure III.2 a and b. The total resistance of the parallel-aligned multilayer is then given by

III.2) $$R_P = N\frac{R_\uparrow R_\downarrow}{R_\uparrow + R_\downarrow}$$

where N is the number of the four-layer unit cells within the multilayer. The total resistance of the antiparallel-aligned multilayer equals to

III.3) $$R_{AP} = N\frac{R_\uparrow + R_\downarrow}{2}$$

Thus, the magnetoresistance ratio is determined by the simple expression

III.4) $$\frac{\Delta R}{R} = \frac{R_{AP} - R_P}{R_P} = N\frac{(R_\downarrow - R_\uparrow)^2}{4R_\downarrow R_\uparrow}$$

Note that within this definition, in which GMR effect is normalized to the low resistance R_P, the effect can be larger than 100%. Bruno and co workers [*Ref. III.6*] collected in his study the various conventions adopted in scientific articles, the previous definition as an optimistic estimation effect. Their study shows that the effect GMR may also be assessed by normalising to the highest resistance R_{AP} for which

III.5) $$\frac{\Delta R}{R} = \frac{R_{AP} - R_P}{R_{AP}}$$

having thus a worst estimation of GMR effect. On the contrary, normalising to the sum the resistance of both the multilayer, it would lead to the evaluation referred to as "reasonable" effect

III.6) $$\frac{\Delta R}{R} = \frac{R_{AP} - R_P}{R_{AP} + R_P}$$

How is predictable and how it will be later reported graphically through simulations, the definitions lead to widely different estimations. Nevertheless, the definition yield by eq.III.4 is used in most papers devoted to GMR [*Ref. III.7 - Ref. III.10*].

Using eq.III.1 and eq.III.4 it is easy to identify the main factors which determine GMR. In the limit that the resistance of the spacer layer is small as compared to the resistance of the ferromagnetic layers, the expression for GMR is

III.7) $$\frac{\Delta R}{R} = \frac{(\rho_\downarrow - \rho_\uparrow)^2}{4\rho_\downarrow \rho_\uparrow} = \frac{(\alpha - 1)^2}{4\alpha}$$

where the spin asymmetry parameter is defined by $\alpha = \rho_\downarrow / \rho_\uparrow$. As it is obvious from eq.III.7, the magnitude of GMR is strongly dependent on the asymmetry in the resistivity between the two spin conduction channels in ferromagnetic layers. Large asymmetry, i.e. $\alpha >> 1$ or $\alpha << 1$, is an important requirement for obtaining high values of GMR. If there is no spin asymmetry in the resistivity of the two spin channels, i.e. $\alpha = 1$, then the GMR will be zero.

The above model is too simplified as GMR depends on many other factors such as the properties of the FM/NM interface which were ignored in this estimate. The finite resistance of the spacer layer may also be taken into account [*Ref. III.11*], which leads to

III.8) $$\frac{\Delta R}{R} = \frac{(\alpha - 1)^2}{4(\alpha + pd_{NM}/d_{FM})(1 + pd_{NM}/d_{FM})}$$

where $p = \rho_{NM}/\rho_{\uparrow}$. Hence, for a given value of α, the GMR will increase with decreasing pd_{NM}/d_{FM}. Therefore, in order to obtain higher GMR, it is important to have a low resistivity of the non-magnetic spacer layer. As a function of the spacer thickness d_{NM}, the GMR decreases monotonically and at large spacer thickness it falls off as $1/d_{NM}^2$. Although the drop in GMR with increasing spacer thickness is also found in experiments, the experimental behaviour on d_{NM} is different compared to this simplified model. As discussed later, the CIP GMR is found to decrease exponentially with d_{NM} for large spacer thicknesses. The reason for this disagreement is that the series-resistor model is not applicable for d_{NM} large compared to the mean free path. In the latter case, more sophisticated models have to be applied.

III.2. Semiclassical Boltzmann theory within free-electron model

The resistor model, which has been introduced in the previous paragraph, is too simple to describe correctly CIP GMR in magnetic multilayers and spin valves. This model is based on the assumption that the mean free path is long for both spin channels as compared to layer thicknesses ($\lambda >> d$). This approximation is not justified for real layered systems because the mean free path within one of the spin channels is comparable to or even less than the layer thickness. In addition, the resistor model is unable to predict the asymptotic behavior of GMR for large layer thicknesses. A more sophisticated quantitative insight into spin-dependent transport can be obtained using the semiclassical Boltzmann theory of transport [*Ref. III.12,Ref. III.13*]. This theory considers electron transport using classical dynamics. Nevertheless, the semiclassical theory includes many aspects of quantum mechanics. For example, within this approach quantum-mechanical statistics is used and scattering can be calculated quantum-mechanically assuming a realistic band structure. Boltzmann theory is based on a semiclassical description of the electrons in metals in the presence of external fields using a statistical distribution function. The distribution function $f(\mathbf{r},\mathbf{k},t)$ is defined as the number of electrons with given position $\mathbf{r}$ and wave-vector $\mathbf{k}$ at time t. We assume that the two spin states of the electrons are uncoupled and, therefore, the distribution function can be considered independently for the up- and down-spin channels. The Boltzmann transport equation is obtained by balancing the change in the distribution function caused by the applied electric field and the scattering processes that act to bring it back towards equilibrium. The equation is described as follow

III.9) $$\frac{df(\mathbf{r},\mathbf{k},t)}{dt} = -\dot{\mathbf{r}}\cdot\nabla_{\mathbf{r}} f - \dot{\mathbf{k}}\cdot\nabla_{\mathbf{k}} f + \left(\frac{df}{dt}\right)_{scatt}$$

The first term in this equation describes the electron drift due to their velocity, the second term reflects the acceleration of the electrons due to the applied field and the scattering term describes scattering of the electrons by imperfections in the lattice, such as defects or impurities. It can be written in terms of the probability $P_{\mathbf{kk}'}$ for an electron to scatter between momentum $\mathbf{k}$ and $\mathbf{k}'$:

III.10) $$\left(\frac{df}{dt}\right)_{scatt} = \sum_{\mathbf{k}'}\{P_{\mathbf{kk}'}[1-f(\mathbf{r},\mathbf{k},t)]f(\mathbf{r},\mathbf{k}',t) - P_{\mathbf{k}'\mathbf{k}}[1-f(\mathbf{r},\mathbf{k}',t)]f(\mathbf{r},\mathbf{k},t)\}$$

where the right-hand term describes "scattering-out" processes, in which an electron from an occupied state of momentum **k** scatters into unoccupied states **k′** , and the left-hand term describes scattering processes, in which electrons from occupied states of momentum **k′** scatter into an unoccupied state **k**. We are interested in a steady state solution, when the distribution function is no longer changing so that *df*/*dt*=0 in eq.III.9. In this case, taking into account the principle of microscopic reversibility, i.e. $P_{\mathbf{kk'}} = P_{\mathbf{k'k}}$, and assuming a uniform applied electric field ***E***, we obtain

III.11) $$\mathbf{v}(\mathbf{k}) \cdot \nabla_{\mathbf{r}} f(\mathbf{r},\mathbf{k}) - \frac{e}{\hbar}\mathbf{E} \cdot \nabla_{\mathbf{k}} f(\mathbf{r},\mathbf{k}) = \sum_{\mathbf{k'}} P_{\mathbf{kk'}} [f(\mathbf{r},\mathbf{k}') - f(\mathbf{r},\mathbf{k})]$$

where *e* is the absolute value of the electron charge and **v** is the electron velocity. Aiming at a linear response theory, it is convenient to represent the distribution function as $f(\mathbf{r},\mathbf{k}) = f_0(\mathbf{k}) + g(\mathbf{r},\mathbf{k})$, where *g*(**r**,**k**) is the deviation of the distribution function *f*(**r**,**k**) from the equilibrium Fermi-Dirac distribution $f_0(\mathbf{k}) = \{1 + \exp[(E(\mathbf{k}) - E_F)/kT]\}^{-1}$ due to the applied electric field. Substituting this form into eq.III.11 and retaining only the lowest order contribution with respect to ***E*** we obtain

III.12) $$\mathbf{v}(\mathbf{k}) \cdot \nabla_{\mathbf{r}} g(\mathbf{r},\mathbf{k}) - e\mathbf{E} \cdot \mathbf{v}(\mathbf{k}) \frac{\partial f_0(\mathbf{k})}{\partial E(\mathbf{k})} = \sum_{\mathbf{k'}} P_{\mathbf{kk'}} [g(\mathbf{r},\mathbf{k}') - g(\mathbf{r},\mathbf{k})]$$

This is a general representation of the linearized Boltzmann kinetic equation for the description of the electric current, the density of which is given by

III.13) $$\mathbf{j}(\mathbf{r}) = -\frac{e}{V}\sum_{\mathbf{k}} \mathbf{v}(\mathbf{k}) \cdot g(\mathbf{r},\mathbf{k})$$

where *V* is the volume of the system. However, the evaluation of eq.III.12 is not easy to perform because of the scattering term $\sum_{\mathbf{k'}} P_{\mathbf{kk'}} \cdot g(\mathbf{r},\mathbf{k}')$, which links the values of the distribution function at various momenta. The Boltzmann equation can be simplified using the relaxation time approximation. Within this approximation the scattering-in term is neglected and results in

III.14) $$\mathbf{v}(\mathbf{k}) \cdot \nabla_{\mathbf{r}} g(\mathbf{r},\mathbf{k}) - e\mathbf{E} \cdot \mathbf{v}(\mathbf{k}) \frac{\partial f_0(\mathbf{k})}{\partial E(\mathbf{k})} = -\frac{g(\mathbf{r},\mathbf{k})}{\tau(\mathbf{k})}$$

where $\tau(\mathbf{k})$ is the relaxation time for an electron to scatter out of momentum state **k**, which is defined by

III.15) $$\tau^{-1}(\mathbf{k}) = \sum_{\mathbf{k'}} P_{\mathbf{kk'}}$$

In general, neglecting the scattering-in term is not a trivial approximation and has to be justified (*Ref. III.12*). For a bulk homogeneous system it is coherent within the relaxation time approximation to derive the expression for the conductivity tensor $\sigma^{\mu\nu}$ which is defined by

III.16) $$\mathbf{j}^{\mu} = \sum_{\nu} \sigma^{\mu\nu} E^{\nu}$$

where the indices μ and ν denote the Cartesian components. In this case $\nabla_{\mathbf{r}} g(\mathbf{r},\mathbf{k}) = 0$ and it follows from eq.III.14 that

III.17) $$g(\mathbf{k}) = e\tau(\mathbf{k})\frac{\partial f_0(\mathbf{k})}{\partial E(\mathbf{k})}\mathbf{v}(\mathbf{k})\cdot\mathbf{E}$$

Taking the zero-temperature limit, i.e. $\partial f_n^0(\mathbf{k})/\partial E_n(\mathbf{k}) = -\delta[E(\mathbf{k}) - E_F]$ and substituting eq.III.17 into eq.III.13, we obtain the well-known expression for the conductivity for single spin channel within the relaxation time approximation [*Ref. III.12*]

III.18) $$\sigma^{\mu\nu} = \frac{e^2}{V}\sum_{\mathbf{k}} \mathbf{v}^{\mu}(\mathbf{k})\mathbf{v}^{\nu}(\mathbf{k})\tau(\mathbf{k})\delta[E(\mathbf{k}) - E_F]$$

Films and multilayers are assumed to be homogeneous in the *xy* plane of the layers but inhomogeneous in the *z* direction perpendicular to the planes, due to the presence of the interfaces and boundaries, therefore, the distribution function g(*z*,**v**) is dependent on *z*, but independent of *x* and *y*. In this case the solution of the Boltzmann equation (eq.III.14) takes the form

III.19) $$g^{\pm}(\mathbf{r},\mathbf{k}) = e\tau(\mathbf{k})\mathbf{E}\cdot\mathbf{v}(\mathbf{k})\frac{\partial f_0(\mathbf{k})}{\partial E(\mathbf{k})}\left[1 + A^{\pm}(\mathbf{k})\exp\left(\frac{\mp z}{\tau(\mathbf{k})|\mathbf{v}_z(\mathbf{k})|}\right)\right]$$

Here signs ± refer to whether the *z*-component of the electron velocity is positive or negative. The coefficients $A^{\pm}$ are determined from matching the boundary conditions at the interfaces and outer boundaries in terms of reflection and transmission probabilities. The current density can be obtained from eq.III.13.

Within a free-electron model the band structure of a magnetic multilayer or a thin film is described using a single parabolic band which is independent of the spin direction. The complicated electronic structure of the transition metals is therefore significantly simplified by neglecting contribution from the *d* bands and their strong hybridization with the *sp* bands. Within the free-electron approximation the expression for the conductivity per spin, which can be found from eq.III.13 by integrating over the film thickness, is simplified [*Ref. III.15*]:

$$\sigma = \frac{1}{d}\sum_{i}^{n}\frac{d_i}{\rho_i} - \frac{3}{4}\frac{\lambda_i}{\rho_i}\int_0^1 d\mu\left(1-\mu^2\right)\mu\left[A_i^{+}(\mu)\left(1-e^{-\frac{d_i}{\lambda_i\mu}}\right)+A_i^{-}(\mu)\left(1-e^{\frac{d_i}{\lambda_i\mu}}\right)\right] \qquad \textit{III.20)}$$

Here we have assumed for simplicity that the relaxation time is independent of **k** and introduced the layer-dependent mean free paths $\lambda_i = \tau_i v_F$. In eq.III.20 μ refers to the cosine of the momentum perpendicular to the interfaces, *d* is the total thickness of the multilayer, d_i and ρ_i are the thickness and the resistivity of the metal layer *i*, omitting spin indices. The first term in this expression gives the conductivity if the various layers were carrying the electric current in parallel. The second term is responsible for finite size effects. The coefficients $A^{\pm}$ can be found using the boundary conditions.

We note that the solution of the Boltzmann equation takes the form of equation III.19 only for the CIP geometry. In this case the current and applied field can be assumed to be uniform within the plane of the multilayer. For the CPP geometry the electric field is position and spin dependent because magnetic multilayers are inhomogeneous in the direction of the electric current [*Ref. III.14*] therefore, equation III.19 does not hold. This point will be further discussed in the next paragraph.

III.3. From Boltzmann equation model to macroscopic transport equations

For the CIP geometry, there are several classical and quantum models, both based on the existence of spin-dependent scattering. Their common physical content is that the electrons average the properties of multilayers in the perpendicular direction on the length scale of the electron mean free path (MFP) λ. This implies that GMR vanishes when the period of the multilayer becomes larger than MFP [*Ref. III.16-Ref. III.18*].

For CPP geometry, the experimental results [*Ref. III.19*] bring to a two current scheme with volume and interface resistances in series for each spin direction [*Ref. III.20*]. Alternatively, it has been proposed to explain the CPP-MR of multilayers by using the concept of "spin coupled interface resistance". This concept was introduced [*Ref. III.21-Ref. III.23*] to describe the electron transport through an interface between ferromagnetic and nonmagnetic metals. Briefly, in the ferromagnet, if the current is spin polarized, there will be spin accumulation around the interface with the nonmagnetic metal. This spin accumulation gives rise to an extra potential drop ΔV_I, proportional to the current density J, $\Delta V_I = J r_{SI}$ where r_{SI} is the "spin coupled interface resistance". This effect does not appear in the CIP geometry because there is no net charge or spin transport through the interfaces and therefore no spin accumulation. The extension of this theory to multilayer [*Ref. III.21*] assumes that spin coupled interface resistances of successive interfaces are additive[*Ref. III.22, Ref. III.23*]. Really, in the limit appropriate for the experiments, i.e. with thicknesses much shorter than the spin diffusion length (SDL) l_{sf}, the assumption of additive interfaces resistance is incorrect [*Ref. III.24*]. The spin accumulation induced by successive interfaces interfere and partly balance each other. This gives a behaviour of CPP-MR different from that asserted before. The second point is that the macroscopic equations used in *Ref. III.21- Ref. III.23* are not valid if the layer thickness become of the order of the MFP.

According to *Ref. III.24*, the Boltzmann equation model reduces to macroscopic transport equations when the SDL is much longer than the MFP, $l_{sf} >> \lambda$, valid whatever the ratio between the layer thicknesses and the SDL. The model considers a structure where single domain ferromagnetic (F) metal layers alternate with non ferromagnetic (N) metal layer. In all the layers, it is assumed a simplified single parabolic conduction band, with the same effective mass m and Fermi velocity v_F. A given current density J flows along the z axis perpendicular to the plane of the layers and only configuration where the magnetization of a given F layer is "up" or "down" along the x axis, taken as spin quantization axis, has been considered. Because the magnetizations are all collinear, the

local velocity distribution function of the conduction electrons for the spin direction *s*, $f_s(z,\mathbf{v})$ is introduced. Looking for a solution of the linearized Boltzmann equation, i.e. eq.III.14, the model in *Ref. III.24* considers the local electric field $E(z)=-\partial V(z)/\partial z$ and, in order to account for spin accumulation, the chemical potential for spin *s*, $\mu_s(z)$ jointly with $\bar{\mu}_s(z)=\mu_s(z)-eV(z)$ the electrochemical potential for spin *s*. These statements lead to a new set of equations resulting from the Boltzmann equation:

III.21) $$\frac{e}{\sigma_s}\frac{\partial J_s}{\partial z}=\frac{\bar{\mu}_s-\bar{\mu}_{-s}}{l_s^2}$$

III.22) $$\frac{\partial \bar{\mu}_s}{\partial z}(z)=\frac{e}{\sigma_s(z)}\left[J_s(z)-\frac{4}{15}\lambda_s(z)\frac{\partial}{\partial z}\int_{-\infty}^{+\infty}\partial\bar{z}\,G_s^{(2)}(z,\bar{z})\left(\lambda_s(\bar{z})\frac{\partial J_s}{\partial \bar{z}}(\bar{z})\right)\right]$$

where $G_s^{(2)}(z,\bar{z})$ is the Green function, $\lambda_s=v_F\left(1/\tau_s+1/\tau_{sf}\right)^{-1}$ and $l_s=\left[1/3(v_F\lambda_s)\tau_{sf}\right]^{1/2}=\left(D_s\tau_{sf}\right)^{1/2}$ are respectively the local electron mean free path and spin diffusion length for spin *s*, D_s is the diffusion constant.

Equation III.22 shows explicitly that the Boltzmann model beyond the macroscopic transport equation breaks the locality of the linear response relation between the elettrochemical potential gradient and the current. $\partial\bar{\mu}_s/\partial z$ at a given point no longer depends only on the current at the same point but also on the current divergence integrated over a domain centered at this point and upon a length of the order of the MFP. The appearance of a current divergence for spin *s* occurs because of the spin relaxation mechanisms which take place on the length scale of the SDL, $l_s >> \lambda$. This mean that quite generally [*Ref. III.23*]

$$\lambda_s\frac{\partial J_s}{\partial z}\approx\frac{\lambda_s}{l_{sf}}J \qquad \text{with } \left(1/l_{sf}\right)^2=\left(1/l_\uparrow\right)^2+\left(1/l_\downarrow\right)^2$$

For a multilayer with layer thicknesses $t << l_{sf}$, it leads to

$$\lambda_s\frac{\partial J_s}{\partial z}\approx\frac{t}{l_{sf}}\frac{\lambda_s}{l_{sf}}J$$

Proving the whole Boltzmann correction of eq.III.22 is proportional to λ_s / l_{sf} . Thus regardless of the layer thicknesses the macroscopic transport equations eq.III.21 and

III.23) $$J_s = \frac{\sigma_s}{e}\frac{\partial \overline{\mu}_s}{\partial z}$$

Are recovered in the limit $\lambda_s / l_{sf} << 1$. eq.III.23 is just the Ohm's law, and eq.III.21 expresses that, in steady state, the spin accumulation, that is related to the spin current divergences, is balanced by the spin- flip processes. The previous equations should be transformed in a more directly usable way. Thus, the spin-dependent electrochemical potential is written as $\overline{\mu}_{\pm} = \overline{\mu} \pm \Delta\mu$ where $\Delta\mu$ is the term related to the spin accumulation. In free-electron model, $\Delta\mu$ is also related to the out-of-equilibrium magnetization ΔM by $|\Delta\mu| = 2\mu_0 |\Delta M| / (3n\mu_B)$ where *n* is the electron density and μ_B the Bohr magneton. The gradient of spin-dependent part of $\overline{\mu}_{\pm}$ divided by *e* is equivalent to an electric field, $F(z) = 1/e\, \partial\overline{\mu}/\partial z$. Thus eq.III.21and eq.III.23 transform into

III.24)
$$\frac{e}{\sigma_{\pm}}\frac{\partial J_{\pm}}{\partial z} = \pm 2\frac{\Delta\mu}{l_s^2}$$
$$J_{\pm}(z) = \sigma_{\pm}\left[F(z) \pm \frac{1}{e}\frac{\partial \Delta\mu}{\partial z} \right]$$

This leads to a spin-diffusion type equation for $\Delta\mu$

III.25) $$\frac{\partial^2 \Delta\mu}{\partial z^2} = \frac{\Delta\mu}{l_{sf}^{\ 2}}$$

in an homogeneous medium, hold the following general solution:

III.26) $$\Delta\mu = A\exp(z/l_{sf}) + B\exp(-z/l_{sf})$$

III.27) $$(\sigma_+\overline{\mu}_+ + \sigma_-\overline{\mu}_-) = Cz + D$$

At this stage, it is possible to introduce a bulk spin asymmetry coefficient β in the F layers,

III.28) $\rho_{\uparrow(\downarrow)} = 1/\sigma_{\uparrow(\downarrow)} = 2\rho_F^*\left[1-(+)\beta\right]$

and write in the N layers $\rho_{\uparrow(\downarrow)} = 2\rho_N^*$, obtaining the general expressions of $\overline{\mu}_{\pm}(z)$, *F(z)* and $J_{\pm}(z)$ reported in the Appendix C of *Ref. III.24.* Obviously, they still depend on various integration constant which have to be determined in each layer by taking into account the proper boundary conditions at each interface. As example, an interface located at $z=z_0$ leads to the continuity of the current, $J_s\left(z=z_0^{+}\right)-J_s\left(z=z_0^{-}\right)=0$. In presence of interface scattering, i.e. significant scattering localized in an interfacial zone that is supposed to be infinitely thin, the potential conditions are $\overline{\mu}_s\left(z=z_0^{+}\right)-\overline{\mu}_s\left(z=z_0^{-}\right)=r_s\left[J_s\left(z=z_0\right)/e\right]$ where r_s is the spin-dependent boundary resistance for a unit surface of the *F/N* interfaces. In the same way as in the bulk, it is possible to introduce an interfacial spin asymmetry coefficient γ according to

III.29) $r_{\uparrow(\downarrow)} = 2r_b^*\left[1-(+)\gamma\right]$

Using the general solutions [*Ref. III.24*] and taking into account the previous boundary conditions at each interfaces, all the parameters of interest in any multilayer structure can be calculated.

The general case of a multilayer with both interface and bulk spin-dependent scattering can be summarized into a resistor scheme of Figure III.3(a) for the AP configuration and of Figure III.3(b) for the P configuration. These schemes, in the limit $t_F << l_{sf}^{(F)}, t_N << l_{sf}^{(N)}$, allow the calculation of the resistance of a multilayer according to the following expressions

III.30) $r_{+(-)}^{(AP)} = \left(r_+^{(P)} + r_-^{(P)}\right)/2$

III.31) $r_{+(-)}^{(P)} = 2\rho_F^*\left[1+(-)\beta\right]t_F + 2\rho_N^* t_N + 4r_b^*\left[1+(-)\gamma\right]$

This gives the type of expression already used [*Ref. III.20*] for the interpretation of experimental results on Ag/Co and Cu/Co multilayers formed by *M* bilayers:

III.32) $R^{(AP)} = M\left(\rho_F^* t_F + \rho_N^* t_N + 2r_b^*\right)$

III.33) $$\frac{1}{R^{(P)}} = \frac{1}{M}\left(\frac{1}{2\rho_F^*(1-\beta)t_F + 2\rho_N^* t_N + 4r_b^*(1-\gamma)} + \frac{1}{2\rho_F^*(1+\beta)t_F + 2\rho_N^* t_N + 4r_b^*(1+\gamma)}\right)$$

which leads to

III.34) $$R^{(P)} = R^{(AP)} - \frac{\left(\beta\rho_F^*\left(t_F/(t_F+t_N)\right)L + 2\gamma r_b^* M\right)^2}{R^{(AP)}}$$

where $L = M(t_F + t_N)$ is the total thickness of the multilayer, $\rho_F^*\left(t_F/(t_F+t_N)\right)L$ is the total resistance of the magnetic layers and $2r_b^* M$ the total resistance of the interfaces.

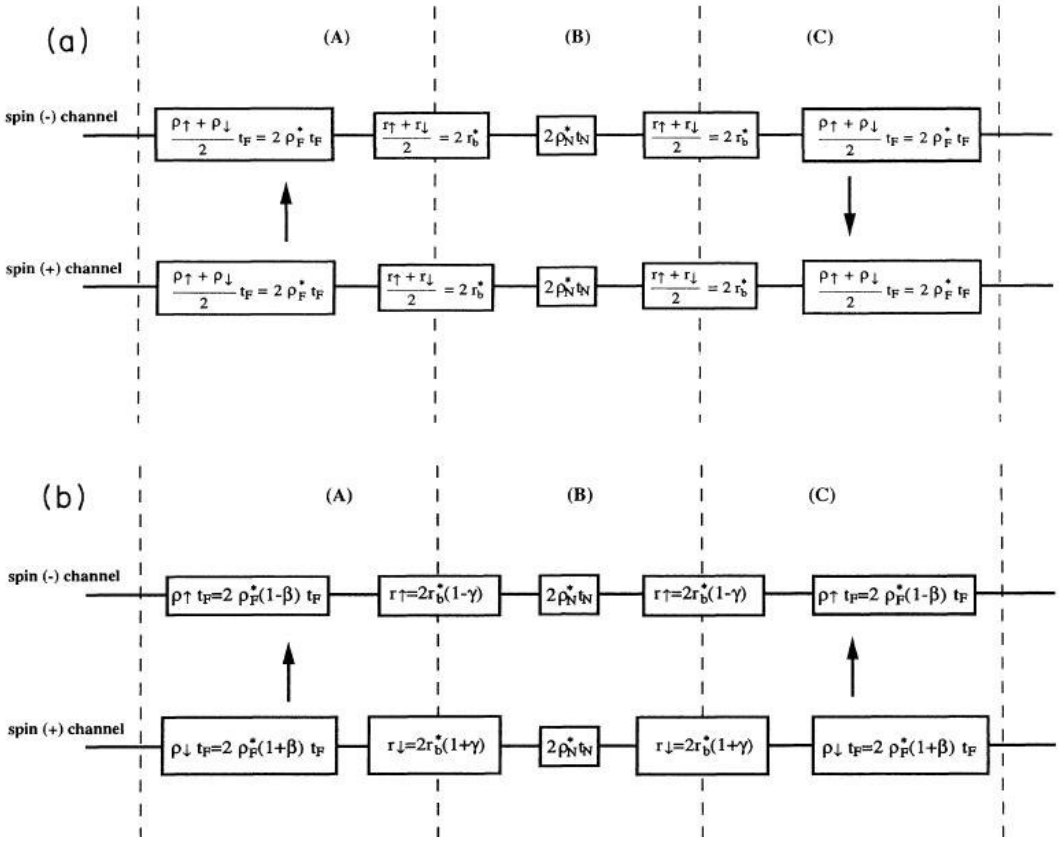

Figure III.3 Equivalent resistance array giving the potential drop coming from the pseudoelectric field F in the limit $(t_N, t_F) << l_{sf}$ *, for the general case with both bulk and interface spin dependent scattering. (a) is for an anti-ferromagnetic arrangement and (b) is for a ferromagnetic one.* $\rho_\uparrow$ *and* $\rho_\downarrow$ *are the resistivities induced by spin-dependent bulk scattering.* $r_\uparrow$ *and* $r_\downarrow$ *are the resistivities induced by spin-dependent interface scattering. The letters (A) and (C) are denoted the ferromagnetic layers while (B) is to denote the normal layers.*

From the literature, in particular *Ref. III.20* and *Ref. III.24*, it is possible to retrieve the physically significant parameters, concerning Ag/Co and Cu/Co multilayers, showed in the following table:

	$\rho_N^*\ [n\Omega m]$	$\rho_F^*\ [n\Omega m]$	bulk spin asymmetry β	$\alpha_F = \rho_\downarrow/\rho_\uparrow$	$r_b^*\ [\Omega m^2]$	interfacial spin asymmetry γ	$\alpha_b = r_\downarrow/r_\uparrow$
Co/Ag	10 ± 1	107 ± 10	0.48 ± 0.05	≈ 2.9	$(0.56\pm0.03)10^{-15}$	0.85 ± 0.03	≈ 12
Co/Cu	7 ± 2	87 ± 4.5	0.5 ± 0.1	≈ 3	$(0.5\pm0.02)10^{-15}$	0.76 ± 0.05	≈ 7.3

Table III.1 Physically significant parameters for Co/Ag and Co/Cu multilayers. Generally, in Co layers, even if the mean free path is somewhat shorter than in Ag or Cu (i.e. $\lambda \approx 10^2$ Å), spin-diffusion lengths $l_{sf} \approx 10^3$ Å are expected. Thus, mean free path $\lambda = 10^2$ Å $<< l_{sf} = 10^3$ Å spin diffusion length. Data from Ref. III.24.

By adopting these data into eq.III.32 and eq.III.34, it is possible to obtain the GMR behaviour of a magnetic multilayer as function of the number of Co/Cu bilayers:

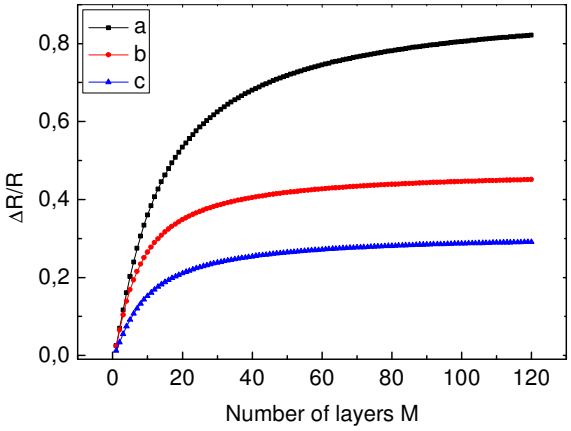

Figure III.4 GMR behaviour as a function of the number of bilayers, t_{Cu} varying (fixed the total thickness L=7200 Å, the spin diffusion length l_{sf}=2000 Å and t_{Co}= 60 Å $\rightarrow t_{Cu} = L/M - t_{Co}$, $t_{Cu} = 5\cdot10^{-11} \div 7\cdot10^{-7}$). Following the different GMR definitions, we denote with (a) the optimistic, (b) the pessimistic and (c) the reasonable characterizations of the GMR effect. Data from Ref. III.25.

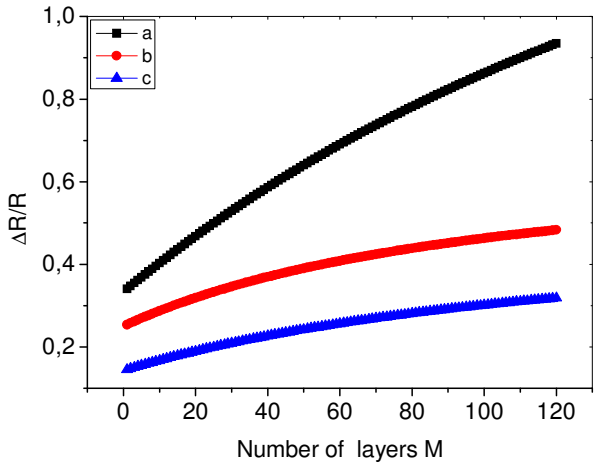

Figure III.5 GMR behaviour as a function of the number of bilayers, t_{Co} varying (fixed the total thickness L=7200 Å, the spin diffusion length l_{sf}=2000 Å and t_{Cu}= 30 Å $\rightarrow t_{Cu} = L/M - t_{Co}$, $t_{Cu} = 6 \cdot 10^{-10} \div 7 \cdot 10^{-7}$). Following the different GMR definitions, we denote with (a) the optimistic, (b) the pessimistic and (c) the reasonable characterizations of the GMR effect. Data from Ref. III.25.

As shown in the previous figures, with increasing number of FM/NM bilayers within a multilayer the value of GMR monotonically increases until it reaches saturation. One of the factors, which may play a role in increasing GMR with the number of bilayers, is an improvement in the structural quality for the thicker multilayers. However, the major factor, which is responsible for the behavior of GMR versus *M,* shown in Figure III.4, is the presence of centre of scattering at the outer boundaries of the multilayer. The calculated linear variations shown that finite l_{sf} are similar to those published in *Ref. III.21*.

Our attention is principally based on Co/Cu multilayers because of the high values of GMR, published by literature, that are even 120% in Co/Cu multilayers [*Ref. III.26*]. Sizeable values of GMR were also obtained in the multilayers: Co/Ag, 22% at room temperature, but the higher values for Co/Cu multilayers lead to pay more attention to this composition. In fact, it was found that the magnitude of GMR varies considerably depending on the chemical constituents of the multilayer. There are two factors, which are crucial for obtaining high values of GMR. These are the band matching and the lattice matching between the ferromagnetic and nonmagnetic metals. The noble metals Ag and Au can serve as good spacer materials in Co-, Ni- and $Ni_{80}Fe_{20}$–based multilayers and spin valves. These metals have electronic and atomic structure similar to Cu, although not as good band and lattice matching with the 3*d* ferromagnets. For example, $Ni_{80}Fe_{20}$/Ag, and $Ni_{80}Fe_{20}$/Au permalloy-based multilayers show GMR values of about 20% at room temperature and

reveal a high sensitivity of the resistance to the applied field, 0.2%/Gauss, and low interlayer coupling [*Ref. III.27, Ref. III.28*]. This combination makes them attractive for applications. Unfortunately, the growth of these multilayers represents a real problem. For example the $Ni_{80}Fe_{20}$/Ag multilayer has to be deposited at liquid-nitrogen temperatures in order to obtain the required integrity of the layers.

III.4. Nonmagnetic layer thickness dependence

When considering the dependence of GMR on the non-magnetic layer thickness in magnetic multilayers and spin valves one should compare the resistances of the perfectly parallel and antiparallel magnetic configurations. The presence of the interlayer exchange coupling leads to oscillations in GMR, similar to those displayed in Figure III.6. This oscillatory contribution to GMR reflects the extent of antiparallel alignment, which is achieved at zero magnetic field, rather than an intrinsic variation in GMR. Spin valves are in this sense better for studying the spacer thickness dependence of GMR than magnetic multilayers. This is due to the pinned ferromagnetic layer, which keeps the direction of its magnetization and helps to maintain an antiparallel alignment of the magnetizations in a certain field interval, provided that the ferromagnetic interlayer coupling is not stronger than the exchange-bias field. However, at small spacer thicknesses the magnetic layers may become strongly coupled ferromagnetically due to the presence of pinholes in the nonmagnetic film, leading to a decreased GMR ratio.

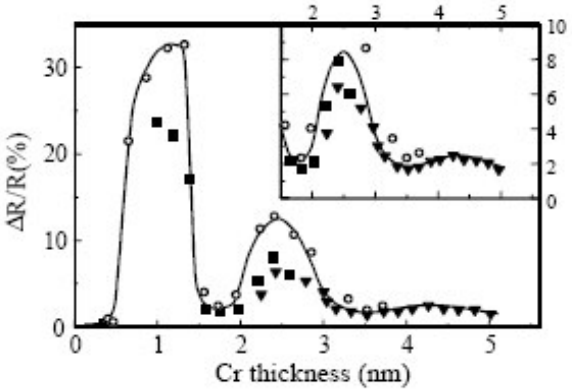

Figure III.6 Saturation magnetoresistance at 4.2K versus Cr thickness for Si(111)/Cr(10nm)/[Fe(2nm)/Cr(t)]NCr(5nm) multilayers deposited at various temperatures: triangles and squares - 40°C (N=30); circles - 125°C (N=20). Data from Parkin et al. [Ref. III.29]

The dependence of GMR on the non-magnetic layer thickness in spin valves was studied by Dieny and co-workers [*Ref. III.30*]. Figure III.7 shows the variation of GMR as a function of the thickness of the non-magnetic layer (NM) in spin valve structures with composition:

Si/Co(7nm)/NM(*dNM*)/Ni80Fe20(5nm)/ Fe50Mn50Mn(8nm) with NM=Cu and Au. As seen from the following figure, the value of GMR decreases monotonically with increasing non-magnetic layer thickness.

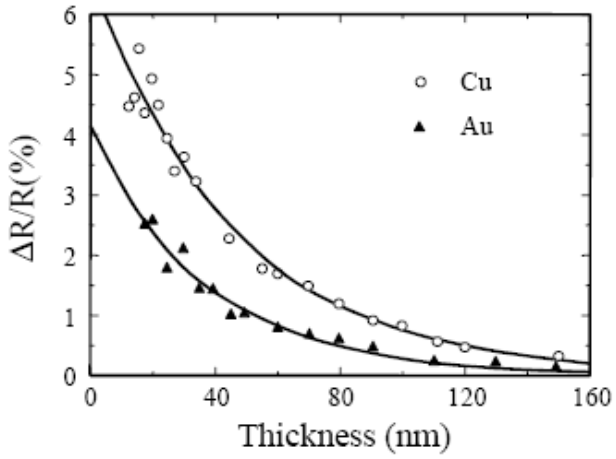

Figure III.7 Magnetoresistance at room temperature versus thickness of the noble-metal layer in spin valves Si/Co(70nm)/NM(dNM)/Ni80Fe20(5nm)/Fe50Mn50(8nm)/NM(1.5nm) with NM = Cu and Au. The solid lines represent fits according to eq.III.1. Data from Dieny et al. [Ref. III.30]

This decrease can be qualitatively ascribed to two factors. (i) With increasing spacer thickness the probability of scattering increases as the conduction electrons traverse the spacer layer, which reduces the flow of electrons between the ferromagnetic layers and consequently reduces GMR. (ii) The increasing thickness of the nonmagnetic layer enhances the shunting current within the spacer, which also reduces GMR. These two contributions to GMR can be described by the following expression:

III.35) $$\frac{\Delta R}{R} = \left(\frac{\Delta R}{R}\right)_0 \frac{e^{-(d_{NM}/l_{NM})}}{(1 + d_{NM}/d_0)}$$

The exponential factor represents the probability that an electron is not scattered within the NM layer. The factor in the denominator describes the shunting effect due to the NM layer. The parameter l_{NM} is related to the mean free path of the conduction electrons in the spacer layer. One expects that l_{NM} will be less than the mean free path in the spacer layer λ_{NM}, due to the fact that electrons which most effectively contribute to GMR have out-of-plane velocities. Dieny *et al.* [*Ref. III.32*] proposed that for systems of practical interest l_{NM} is approximately equal to half of the mean

free path λ_{NM}. The parameter d_0 is an effective thickness, which depends on the conductance of the system in the absence of the NM layer, $(\Delta R/R)_0$ is a normalization coefficient.

It was found that the Cu and Au thickness dependence of GMR, illustrated in Figure III.7, can be well fitted by using the experimental parameters in the following table:

	$l_{NM}\,[nm]$	$\lambda_{NM}\,[nm]$	$\rho_{NM}\,[\mu\Omega m]$
Cu	6	11.5	5
Au	5	8.5	7

Table III.2 Significant parameters of the noble-metal layer. Data from Ref. III.32.

These decay lengths are determined by scattering in the spacer, due to phonons, grain boundaries, and other defects, and are correlated with the mean free path λ_{NM}. The smaller value found for Au is consistent with the higher resistivity of Au.

Our aim is to confirm the GMR trend previously described using the eq.III.32 and eq.III.34, and the physical parameters of the Table III.1.

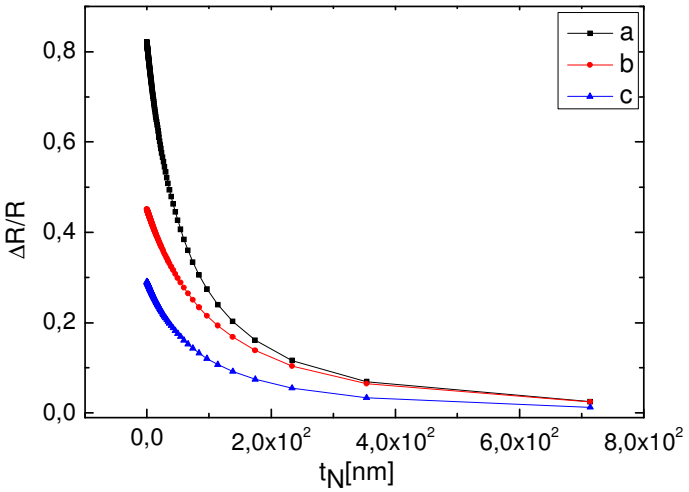

Figure III.8 GMR responses as function of the nonmagnetic layer thickness, t_{Cu} varying (fixed the total thickness $L=7200\,\mathring{A}$, the spin diffusion length $l_{sf}=2000\,\mathring{A}$ and $t_{Co}=60\,\mathring{A}$). In the label, (a) indicates the GMR effect according the formula $R_{AP}-R_P/R_P$, (b) is $R_{AP}-R_P/R_{AP}$ and (c) is $R_{AP}-R_P/R_{AP}+R_P$ respectively.

GMR in magnetic multilayers versus thickness of the non-magnetic spacer layer, see Figure III.8, behaves in a similar way as in spin valves (Figure III.7). Figure III.8 displays values of GMR in

Co/Cu multilayers measured at relatively large Cu thicknesses, so that the interlayer exchange coupling is small [*Ref. III.33*].Note that the interlayer exchange coupling decreases with increasing Cu thickness much faster than GMR, such that the exchange coupling fields become much weaker than the saturation fields.

To have a complete overview of the trend on changing the nonmagnetic layer, we paid attention to alternative materials within the framework of semiconductor materials. In fact, intense research efforts are now devoted to extending these spin-dependent effects to semiconductor materials. There have been noteworthy advances in spin injection and detection using inorganic semiconductors [*Ref. III.34-Ref. III.36*], actually spin-valve devices with semiconducting spacers have not yet been demonstrated. Organic π-conjugated semiconductors may offer a promising alternative approach to semiconductor spintronics. Organic π-conjugated semiconductors (OSEs) are a relatively new class of electronic materials that are revolutionizing important technological applications including information display and large-area electronics [*Ref. III.37*,*Ref. III.38*], owing to their ability to be economically processed in large areas, their compatibility with low-temperature processing, the tunability of their electronic properties, and the simplicity of thin-film device fabrication. For the device in object [*Ref. III.39*], Alq_3 has been chosen, most commonly used in organic light-emitting diodes (OLEDs), to serve as an OSE spacer in organic spin-valves, because it can easily be deposited as thin films and integrated with a variety of metallic electrodes. As shown in Fig. 1a, the vertical organic spin-valves consist of three layers: two ferromagnetic electrode films (*FM1* and *FM2*, respectively) and the OSE spacer. The two *FM* electrodes have different coercive fields (H_{c1} and H_{c2}, respectively).

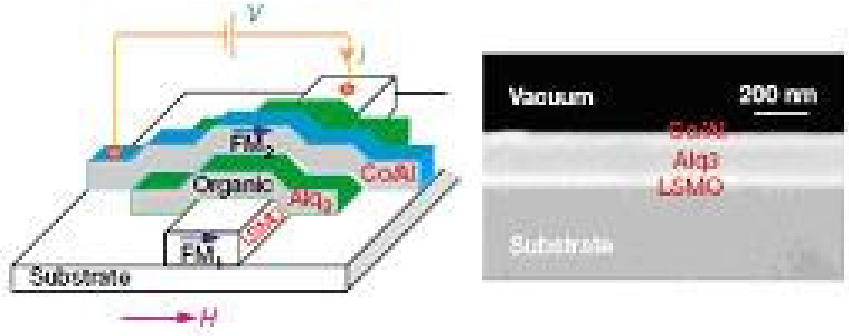

Figure III.9 Schematic representation of a typical device that consists of two FM electrodes (FM1 and FM2) and an OSE spacer. Spin-polarized electrical current I flows from FM1 (LSMO), through the OSE spacer (Alq_3), to FM2 (Co) when a positive bias V is applied. An in-plane magnetic field, H, is swept to switch the magnetization directions of the two FM electrodes separately.

Devices with *d<100 nm*, have an 'ill-defined' layer of up to 100*nm* that may contain pinholes and Co inclusions. These findings suggest that the OSE spacers in the spin-valve devices fabricated with *d>100 nm* may be composed of two sublayers: one sublayer with a thickness d_0 of the order of 100*nm* immediately below the Co electrode that contains Co inclusions owing to the interdiffusion; and a second sublayer of neatly deposited Alq_3 between this defected sublayer and the LSMO film, having a thickness d-d_0, in which carrier transport is dominated by carrier drift.

The GMR effect and its dependence on d can be analysed using a simple injection and diffusion model. In conventional magnetic tunnel junction devices with a very thin insulating tunnel barrier, the Julliere model [*Ref. III.40*] has often been used to analyse the tunnelling magnetoresistance. In the present organic spin-valves, the neatly deposited OSE sublayer with thickness $d–d_0$ is so thick ($>30nm$) that simple quantum mechanical tunnelling through it is not a viable possibility. It is assumed that there exists a potential barrier for spin injection at the Co/OSE interface, which may be self-adjusted. Once carriers are injected through this interface they easily reach the neat sublayer, where they drift under the influence of the electric field towards the other interface, from which they can be extracted. As the injected carriers reach the end of the ill-defined sublayer, the spin polarization is p_1; it further decays in the remaining neatly deposited sublayer with a surviving probability $\exp\left[-(d-d_0/l_S)\right]$, where z is the drift/diffusion distance along the normal direction to the interface, and l_S is the spin diffusion length in the neatly deposited OSE sublayer. The spin polarization p is defined as $p=(N_\uparrow - N_\downarrow)/(N_\uparrow + N_\downarrow)$ where $N_\uparrow(N_\downarrow)$ is the carrier density in the majority (minority) spin state. The thickness dependence of the GMR magnitude is expressed according to the following equation:

III.36) $$\frac{\Delta R}{R}=\frac{R_{AP}-R_P}{R_{AP}}=\frac{2P_1P_2e^{-(d-d_0/l_S)}}{1+P_1P_2e^{-(d-d_0/l_S)}}$$

The experimental values used as references are shown in the following table:

	$d[nm]$	$d_0[nm]$	$l_{NM}[nm]$	$p_1\ p_2$	$\Delta R/R[\%]$
LSMO/Alq_3/Co	130÷250	87	45	-0.32	40÷2

Table III.3 Experimental parameters for the LSMO (100 nm)/Alq3 (130 nm)/Co (3.5 nm) spin-valve device. In the first cell is expressed the range of the values used for the simulation.

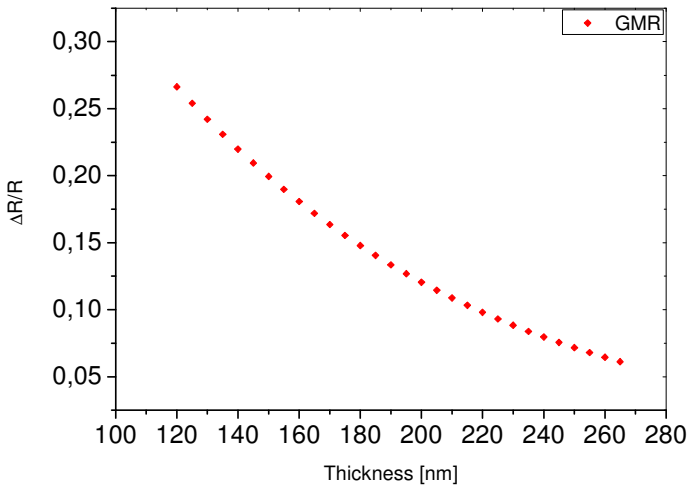

Figure III.10 The GMR value of a series of LSMO/Alq3/Co devices with different d. The line fit through the data points was obtained using the spin diffusion model, equation III.36, with three adjustable parameters shown in Table III.3

By adopting a simple injection and diffusion model, the previous figure is a confirmation that the evolution of the magnetoresistance is descending according an exponential law with the thickness of not magnetic layer.

III.5. Magnetic layer thickness dependence

Similarly to the previous study, the dependence of GMR on the magnetic layer thickness in spin valves - M1(t $\mathring{A}$)/Cu(22 $\mathring{A}$)/$Ni_{80}Fe_{20}$(50 $\mathring{A}$)/$Fe_{50}Mn_{50}$(80 $\mathring{A}$)/Cu(15 $\mathring{A}$) - was studied by Dieny and co-workers [*Ref. III.30*]. They describe the variation of MR in the spin valve structure in terms of the thickness of the nominally "free" magnetic layer *M(1)*=Co, NiFe or Ni, at different temperatures, as shown in the following figure

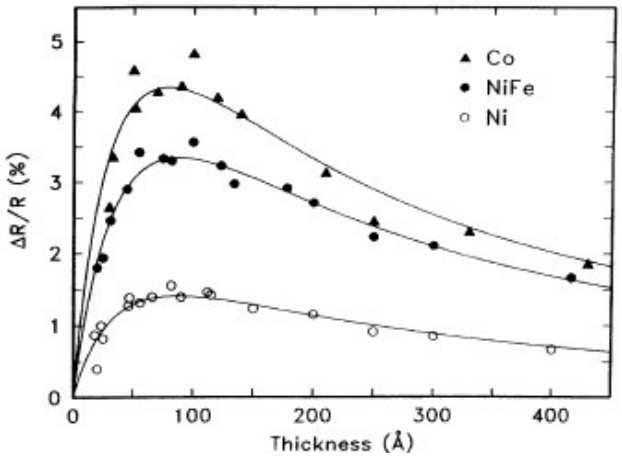

Figure III.11 Variation of the magnetoresistance versus the thickness of the "free" ferromagnetic layer M(1), with M(1)=Co, NiFe or Ni, at room temperature. Data from Ref. III.30.

The observed variations have a very similar shape characterized by a broad maximum between 60 and 110 $\mathring{A}$. This shape is different from that previously observed in Fe/Cr multilayer for which $\Delta R/R$ decreases monotonically for Fe thickness above 10 $\mathring{A}$, which was interpreted as demonstrating the dominant role of interfacial scattering in Fe/Cr [*Ref. III.41-Ref. III.43*]. The broad maximum shows that in the observed structure the MR arises within an "active" part of the ferromagnetic layer, about 90 $\mathring{A}$ thick, located next to the Cu/M interface. The decrease of MR at larger thickness can be attributed to increased shunting with *M(1)* layer thickness.

Following the schematic representation of a spin valve structure in Figure III.12, the ferromagnetic layer, whose thickness is varied, is divided into an "active" and an "inactive" regions. "Active" region means the part of the ferromagnetic layer which gives the main contribution to the MR. At 0*K* the thickness of this *active* part, t_0, is linearly related to the longer of the two spin-dependent

mean free path, λ^+ and λ^-, corresponding to electrons with their spin parallel and antiparallel to the magnetization of the ferromagnetic layer. There is the assumption that λ^+ is the longer of the two mean free paths. Thus, the *inactive* part of *M(1)* is described as a resistance (R_1) which is independent of the orientation of the magnetization, connected in parallel to the resistance (R_0) of the *active* part of the spin valve structure.

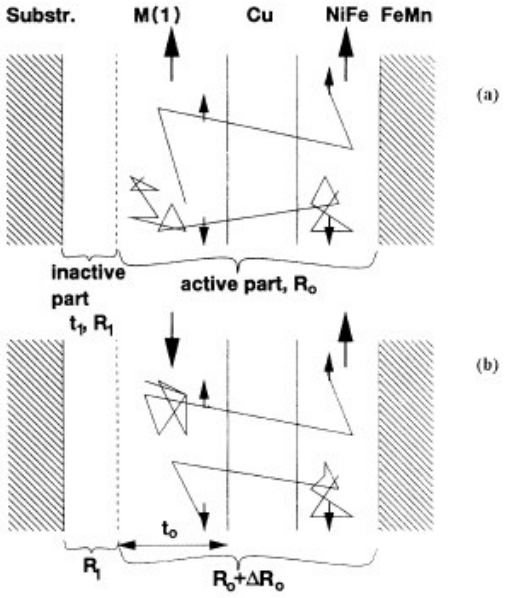

Figure III.12 Schematic representation of the spin valve structure. The two species of electrons (spin ↑ and spin ↓*) have different mean free paths due to the spin- dependent character of the scattering in ferromagnetic transition metal.*

Neglecting the contribution of the other terms including the structure - $Cu/Ni_{80}Fe_{20}/Fe_{50}Mn_{50}//Cu$ – the measured MR is given by

III.37) $$\left[\frac{\Delta R}{R}\right]_{measured} = \frac{R_{\uparrow\downarrow} + R_{\uparrow\uparrow}}{R_{\uparrow\uparrow}}$$

where

III.38) $$R_{\uparrow\uparrow} = \frac{R_0 R_1}{R_0 + R_1}$$

III.39) $$R_{\uparrow\downarrow} = \frac{(R_0 + \Delta R_0)R_1}{R_0 + R_1 + \Delta R_0}$$

Therefore

III.40) $$\left[\frac{\Delta R}{R}\right]_{measured} = \left[\frac{\Delta R_0}{R_0}\right]\frac{1}{1 + R_0/R_1}$$

Introducing the sheet conductance G_{rest} of the rest of the structure $Cu/Ni_{80}Fe_{20}/Fe_{50}Mn_{50}//Cu$, we note that it is varying almost linearly with the thickness of the *M(1)* layer, $G \cong G_{rest} + t_{M(1)}/\rho_{M(1)}$. This behaviour is pull out from experimental observations from *Ref. III.30,* as displayed in the following figure

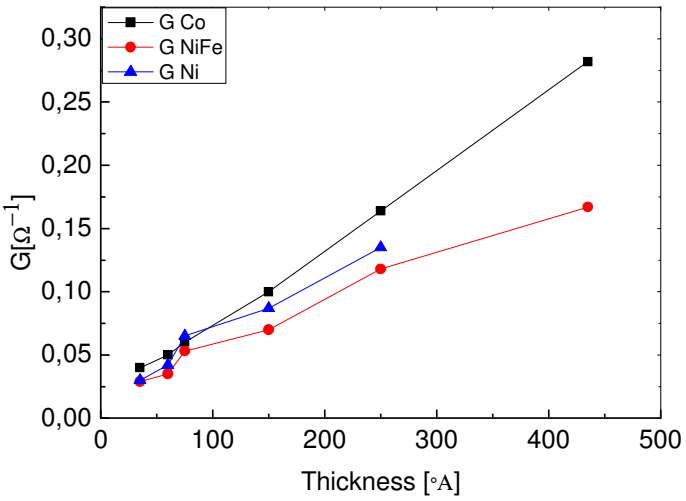

Figure III.13 Variation of the sheet conductance versus M(1) layer thickness for a structure M1(t Å)/Cu(22 Å)/$Ni_{80}Fe_{20}$(50 Å)/$Fe_{50}Mn_{50}$(80 Å)/Cu(15 Å), with M(1)=Co, NiFe and Ni.

In the relevant data, other physical parameters have been extracted as reported in the table below

	NiFe	Ni	Co	Au	Cu
$\rho[\mu\Omega cm]$	29.89	15.89	45	8.42	6.31

Table III.4 Resistivity at room temperature for the materials used in the spin valve

Thus, introducing the sheet conductance G_{rest} in the eq.III.40

III.41) $$\left[\frac{\Delta R}{R}\right]_{measured} \cong \left[\frac{\Delta R_0}{R_0}\right]\frac{G_{rest}+t_0/\rho_{M(1)}}{G_{rest}+t_{M(1)}/\rho_{M(1)}}$$

For $t_{M(1)} > t_0$, a hyperbolic decrease of the MR is expected due to the shunting of the current in the *inactive* part of *M(1).*Below the characteristic thickness *t0* the decrease of MR is due to two effects. The ferromagnetic layer is now so thin that the incoming electrons with the longer mean free path λ^+ have a reasonable probability of scattering not within this layer but rather on the substrate or in the FeMn layer. Thus, the scattering loses some of its spin-dependent character leading to a reduction of ΔR. On the other side, some of the outgoing electrons with the longer mean free path which would have been available from a thick *M(1)* layer are no longer present. Both phenomena can be described quantitatively, assuming that a continuous flow of electrons goes in or out of *M(1).* For $\lambda^+ >> \lambda^-$, most of this flow consists of spin $\uparrow$ electrons, so that the contribution of spin $\downarrow$ can be neglected. A lot of electrons of this flow has a scattering event within a thin layer t(M1) and the probability for a spin $\uparrow$ electron to be scattered is $\left[1-\exp\left(-t_{M(1)}/t_0\right)\right]$. Putting together these two contributions, one from shunting effect, the other from the bulk scattering of spin $\uparrow$ electron, it is possible to extract a more comprensive expression

III.42) $$\frac{\Delta R}{R}\left(t_{M(1)}\right) = A\frac{1-\exp\left(-t_{M(1)}/t_0\right)}{1+t_{M(1)}/G_{rest}\rho_{M(1)}}$$

With two adjustable parameter namely: *A* and t_0 The quantity *A* is characteristic of the materials involved in the essential part of the spin-valve, *M(1)*, *N*, and *M(2)*.

Ferromagnet	*A*(%)	$t_0(\mathring{A})$	$G_{rest}\rho_{M(1)}(\mathring{A})$
Co	14.5	72	65
$Ni_{80}Fe_{20}$	9.6	72	85
Ni	5.1	85	65

Table III.5 Characteristic MR parameter A and "active" layer thickness for the M(1)=Co, NiFe and Ni.

Our aim is to simulate the eq.III.32 and eq.III.34, following the various definitions collected by Bruno and co-workers, to play the same behaviour for a multilayer Co/Cu by referencing to the data in the Table III.1. This results could be useful to design and fabricate a new sensors starting from the fundamental magnetic properties of the materials.

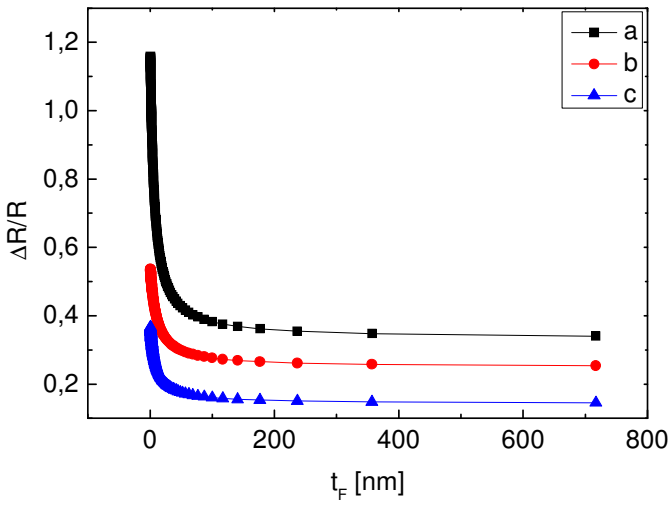

Figure III.14 GMR behaviour as function of the magnetic layer thickness, t_{Co} varying (fixed the total thickness L=7200 Å , the spin diffusion length l_{sf}=2000 Å and t_{Co}= 30 Å . In the label, (a) indicates the GMR effect according the formula $R_{AP}-R_P/R_P$, (b) is $R_{AP}-R_P/R_{AP}$ and (c) is $R_{AP}-R_P/R_{AP}+R_P$ respectively

As reported in Figure III.14, this shape is different from that previously observed because of the hyperbolic decrease of GMR which can be interpreted as a proof of the dominant role of interfacial scattering in Co/Cu multilayers.

References

Ref. III.1 D.M. Edwards, R.B. Muniz, J. Mathon, IEEE Trans. Magn. 3, 4941 (1991)

Ref. III.2 J Mathon, Contemp. Phys. 32, 143 (1991)

Ref. III.3 S. Zhang, P.M. Levy, J. Appl. Phys. 69, 4786 (1991)

Ref. III.4 G.E.W. Bauer, Phys.Rev.Lett. 69, 1676 (1992)

Ref. III.5 H.E Camblong, S. Zhang, and P.M. Levy, Phys. Rev. B 47, 4735 (1993)

Ref. III.6 A. Fert and P. Bruno, ed. by J.A.C. Bland and B. Heinrich, Berlin: Springer, (1994)

Ref. III.7. S.S.P. Parkin, Z.G. Li, and D.J. Smith, Appl. Phys. Lett. 58, 2710 (1991)

Ref. III.8 R. Schad et al. J. Magn. Magn. Mat. 148, 331 (1995)

Ref. III.9 R. Schad et al., Appl. Phys. Lett. 64, 3500 (1994).

Ref. III.10 J.M. George, L.G. Pereira, A. Barthelemy, F. Petroff, L.B. Steren, J.L. Duvail, A. Fert, R .Loloee, P. Holody, and P.A. Schroeder, Phys. Rev. Lett. 72, 408 (1994).

Ref. III.11 E.Y. Tsymbal and D.G. Pettifor, Solid State Physics, 56, 113-237 (2001)

Ref. III.12 N.W. Ashcroft and N.D. Mermin, Solid State Physics, Philadelphia: Saunders College (1976)

Ref. III.13 J.M. Ziman, Principles of the Theory of Solids, London Cambridge Univ. Press (1972)

Ref. III.14 P.M. Levy, Solid State Physics, 47, 367 Boston, London Acad. Press (1994)

Ref. III.15 B. Dieny, J. Phys. Cond Mat. 4, 8009 (1992)

Ref. III.16 R.E. Camley and J. Barnas, Phys. Rev. Lett. 63, 664 (1989)

Ref. III.17 J. Barnas, A. Fuss, R.E. Camley, P. Grunberg, W. Zinn, Phys. Rev. B 42, 8110 (1990)

Ref. III.18 P.M. Levy, S. Zhang, A. Fert, Phys. Rev. Lett. 65, 1643 (1990)

Ref. III.19 W.P. Pratt et al., Phys. Rev. Lett. 66, 3060 (1991)

Ref. III.20 S.F. Lee et al., J. Magn. Magn. Mater. 118, 1 (1993)

Ref. III.21 M. Johnson, Phys. Rev. Lett, 67, 3594 (1991)

Ref. III.22 M. Johnson, R.H. Silsbee, Phys. Rev. B, 35, 4959 (1987)

Ref. III.23 P.C. van Son et al., Phys. Rev. Lett, 58, 2271 (1987)

Ref. III.24 T. Valet and A. Fert, Phys. Rev. B, 48, 7099 (1993)

Ref. III.25 A. Fert, J.L. Duvail and T. Valet, Phys. Rev. B, 52, 6513 (1995)

Ref. III.26 S.S.P. Parkin, R. Bharda, and K.P. Roche, Phys. Rev. Lett. 66, 2152 (1991)

Ref. III.27 B. Rodmacq, G. Palumbo, and Ph .Gerard, J. Magn. Magn. Mat. 118, L11 (1993)

Ref. III.28 S.S.P. Parkin et al. Phys. Rev. Lett. 72, 3718 (1994)

Ref. III.29 S.S.P. Parkin, N. More, and K.P. Roche, Phys. Rev. Lett. 64, 2304 (1990)

Ref. III.30 B. Dieny, Phys. Rev. B, 45, 806 (1992)

Ref. III.31 B. Dieny, V.S. Speriosu, S. Metin, S.S.P. Parkin, et al., J. Appl. Phys. 69, 4774 (1991)

Ref. III.32 B Dieny, J. Magn. Mag. Mat. 136, 335 (1994)

Ref. III.33 S.S.P. Parkin, A. Modak, and D.J. Smith, Phys. Rev. B 47, 9136 (1993)

Ref. III.34 J.M Kikkawa and D.D Awschalom, Nature 397, 139–141 (1999)

Ref. III.35 Y. Ohno, et al. Nature 420, 790–792 (1999)

Ref. III.36 A.T. Hanbicki, et al. Appl. Phys. Lett. 80, 1240–1242 (2002)

Ref. III.37 S. Forrest, P. Burrows and M. Thompson, IEEE Spectr. 37, 29–34 (2000).

Ref. III.38 D. Voss, Nature 407, 442–444 (2000)

Ref. III.39 Z.H. Xiong, DiWu, Z. Valy Vardeny and Jing Shi, Lett. To Nature (2004)

Ref. III.40 M. Julliere, Phys. Lett. A 54, 225–226 (1975)

Ref. III.41 M.N. Baibich, J.M. Broto, A. Fert et al. Phys. Rev. Lett. 61, 2472 (1988)

Ref. III.42 G. Binasch, P. Grunberg, F. Saurenbach and W. Zinn, Phys. Rev. B 39, 4828 (1989)

Ref. III.43 J.J Krebd, P. Lubitz, A. Chaiken and A.G. Printz, Phys. Rev. Lett. 63, 4828 (1989)

IV **Characterization of GMR sensors**

The interest in the GMR technologies is due to their possible application in the field of Non Destructive Evaluation (NDE). GMR sensors can be used to test metallic structures of various type and composites of aeronautical interest, e.g. single layer metals, multilayers, or laminates, for the identification of processing or impact defects. In particular, this kind of sensors can potentially improve the performances of NDE systems in terms of spatial resolution and sensitivity for defects of hundreds of μm at depths exceeding 10mm. This chapter will report the experimental characterization of commercially available GMR sensors, including magnetic background noise analysis, conversion factor and non destructive measurements on several materials. Our study aimed to estimate the optimal configuration for a system of commercial GMR sensors. The use of GMR sensors in a gradiometric configuration, together with the applied filtering technique, enables the strong reduction of the magnetic noise increasing the signal to noise ratio. The results coming from the measurements, taken on different materials, allows to understand the advantage of using an electronic gradiometer and the reliability of our experimental probe.

The use of giant magnetoresistive sensors for electromagnetic non destructive evaluation has grown considerably in the last years [*Ref. IV.1-Ref. IV.3*]. Technological advances in the research and development of giant magnetoresistive materials has led to commercially available sensors. Low cost magnetometers based on GMR are now available. The main characteristics of this new device include: high magnetic field sensing, the capability to operate in the industrial magnetic environment, small power consumption, and operation at room temperature [*Ref. IV.4*]. Incorporation of these sensors into NDE probes has widened the range of their application field. In particular, the low frequency sensitivity of these devices provides a practical means to perform electromagnetic inspections on conducting structures. From the requirement to optimize the signal to noise ratio at low frequencies, the idea was born to develop an NDE measurement apparatus based on GMR sensors. Other distinguishing characteristics for GMR magnetometers are the potential sensitivity and the innovation component tied to the use of such technology. They offer the opportunity to develop a measurement system that ties the simple control electronics with the measurement reliability in a not electromagnetically shielded laboratory. A limiting factor in this work appeared to be the increased magnetic background noise level with decreasing frequency. Moreover the incorporation of a commercially available GMR sensor into a gradiometer system could be performed to greatly enhance the low frequency capabilities of the device. In order to improve the signal to noise ratio of the GMR based gradiometer, the system has been low-pass filtered that is shown to greatly reduce the magnetic background noise levels. This permits a good imaging on conducting materials.

IV.1 GMR magnetometers and the gradiometer measurement system

Thin-film GMR materials deposited on silicon substrates can be configured as resistors, resistor pairs or half bridges, and Wheatstone bridges. A sensitive bridge can be fabricated from four photolithographically patterned GMR resistors, two of which are active elements. The sheet resistance of the thin films is between 10Ω and 15Ω per square. Resistors of 10$k\Omega$ can be formed as 2μm serpentine traces covering less than a 100μm square. The following Figure IV.1 shows a view of a magnetometer developed by Non Volatile Electronics (NVE):

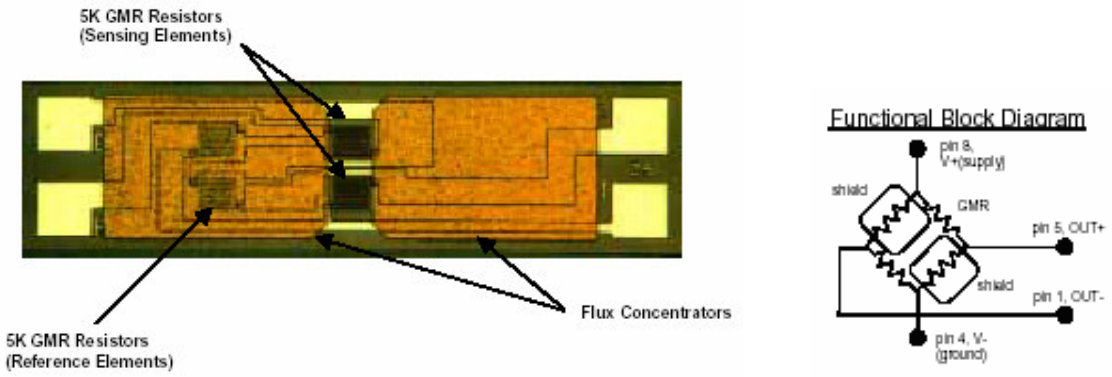

Figure IV.1 Physical layout and electrical scheme of a GMR magnetometer (Non Volatile Electronics, Inc.).

The circuit size is about 350μmx1400μm. Small magnetic shields of permalloy plated over two of the four equal resistors in a Wheatstone bridge protect the resistors from the applied field and let them act as reference resistors. These resistors are connected to the power and to the ground respectively. Because they are made of the same material, the reference resistors have the same temperature coefficient as the active resistors. The two remaining GMR resistors are exposed to the external field. The bridge output is therefore twice the output you would expect of a bridge with only one active resistor. The bridge output for a 10% change in these resistors is ~5% of the voltage applied to the bridge. Additional permalloy structures plated onto the substrate can act as flux concentrators to increase sensitivity. The active resistors are placed in the gap between two flux concentrators. These resistors experience a field larger than the applied field by approximately the

ratio of the gap between the flux concentrators to the length of one of the flux concentrators according the expression

$$B_{GMR} \cong 0.6 \cdot B_{APP} \cdot (l_{FC}/d_{FC})$$

where B_{GMR} is the field at sensor elements, B_{APP} is the external applied field at sensor elements, l_{FC} is the length of the flux concentrators and d_{FC} the gap between them. Therefore, the sensitivity of a GMR bridge sensor can be adjusted in design by changing the lengths of the flux concentrators and the gap between them. In this way, a GMR material, which saturates at ~300*Oe*, can be used to build different sensors, which saturate at 15*Oe*, 50*Oe*, and 100*Oe*. To produce sensors with more sensitivity, external coils and feedback can be used to produce sensors with resolution in the 100*mA/m* or *mOe* range. An example of the output from a low-field GMR bridge sensor is shown in Figure IV.2.

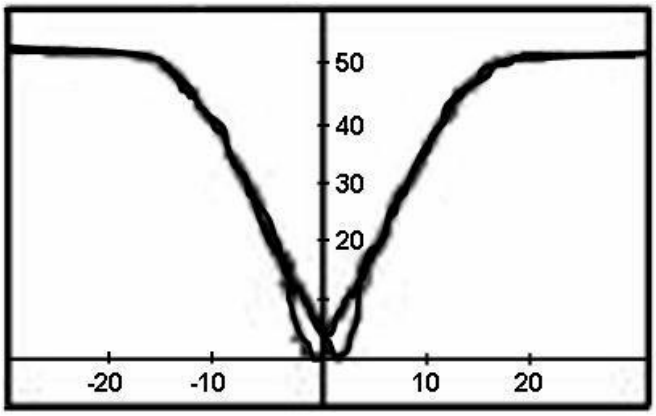

Figure IV.2 The output from a low magnetic field GMR Wheatstone bridge sensor under bipolar excitation shows its omnipolar, or pole-indifferent, response. The hysteresis near the origin is greatest if the sensor is traversed from large positive magnetic fields to large negative fields and back to large positive fields.

The curve traces out a full bipolar excitation of the sensor. The bipolar hysteresis shown is only observed when the sensor crosses from a large negative excursion to a positive excursion or vice-versa. The unipolar hysteresis is shown by the two lines on each side, which almost coincide. This sensor has a bridge resistance of 5*kΩ* and a slope sensitivity of 3.2*mV/V/Oe*. The flux concentrators on this sensor provide a gain of ~16. The following Table IV.1 summarizes the principal sensor characteristics

Part Number	Saturation Field (Oe)	Linear Range (|Oe1|)	Sensitivity (mV/V-Oe1)	Maximum Nonlinearity (% Uni)	Maximum Hysteresis (% Uni)	Maximum Operating Temp (°C)	Typical Resistance (Ohms)
AA005-02	100	10.0-70	0.45-0.65	2	4	125	5K
AA003-02	2.0	14	2-3.2	2	4	125	5K

Table IV.1 Magnetic characteristics of NVE GMR sensors.

The unipolar output characteristic doesn't enable to use a single GMR sensor as magnetometer since it cannot restrict the sign of the observed magnetic field. It is necessary, therefore, the linearization of the output characteristic. To discuss the issue of linearization, we consider the spin valve sensor configuration [*Ref. IV.5 - Ref. IV.7*] shown schematically in Figure IV.3**.** It consists of a ferromagnetic free layer and a ferromagnetic reference layer separated from each other by a thin spacer layer.

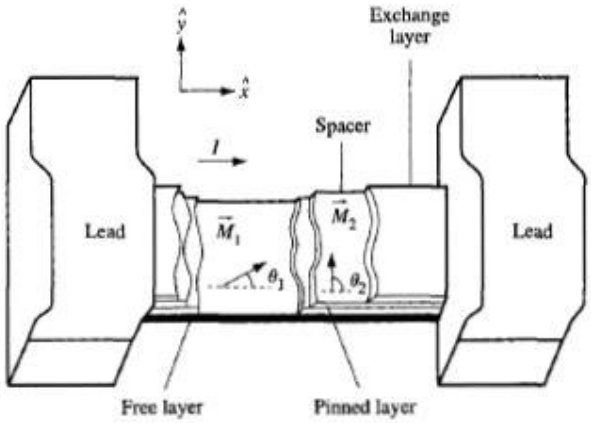

Figure IV.3 Schematic illustration of a spin valve sensor: a ferromagnetic free layer characterized by a magnetic moment M_1 *and a ferromagnetic reference layer characterized by a magnetic moment* M_2 *separated by a thin spacer layer. The magnetic moment of the free layer is allowed to rotate in response to signal fields.*

The magnetic moment M_2 of the reference layer is pinned along the transverse direction, typically by exchange coupling with an antiferromagnetic layer (e.g., FeMn), while the magnetic moment M_1 of the free layer is allowed to rotate in response to signal fields. The resultant spin-valve response is given by

IV.1) $\Delta R \propto \cos(\theta_1 - \theta_2) \propto \sin\theta_1$

where θ_1 and $\theta_2 (= \pi/2)$ represent the directions of free and pinned-layer magnetic moments, respectively (Figure IV.3). If the uniaxial anisotropy hard axis of the free layer is oriented along the transverse signal field direction, the magnetic signal response is linear $\sin\theta_1 \propto H$, yielding in turn a linear spin-valve sensor response through Equation IV.1. This linear spin-valve sensor response is in contrast to the parabolic signal response of conventional GMR or AMR sensors [*Ref. IV.7 - Ref. IV.8*]. However, the linearity of the spin-valve response depends first on the precise transverse magnetic orientation of the reference layer and second on the linearity of the magnetic behaviour of the free layer in the transverse direction. If the pinning field of the reference layer is not high enough compared to the transverse demagnetization field, the reference layer will become non uniformly demagnetized from the transverse direction near the upper and lower edges of the sensor. Also, if the exchange-bias pinning field is misaligned from the transverse direction, the magnetization of the reference layer will be canted as a whole from the transverse direction. In both cases, the θ_2 term in Equation IV.1 will not be $\pi/2$, resulting in a nonlinear spin valve response. In addition, if the uniaxial anisotropy easy axis of the free layer were canted from the longitudinal direction or if the free layer were under the influence of a strong longitudinal bias direction, the magnetic response $\sin\theta_1$ of the free layer would no longer be linear with the external magnetic field, resulting also in nonlinearities in the spin-valve response. Finally, the spin-valve sensor typically incorporates free layers that also exhibit AMR responses, although the net AMR response might be rather weak because of the thinness of the free layer and the shunting of the other layers. If the AMR response is not completely negligible compared with the spin-valve response, the resultant sensor response is modified from the simple linear spin-valve response by the presence of a parabolic nonlinearity from residual AMR response. The linear operation of the spin-valve sensor terminates when the free-layer magnetic moment becomes saturated along either the up or the down transverse direction This magnetic arrangement constitutes optimal biasing for the spin-valve sensor, which is very different from optimal biasing for an AMR sensor, where the magnetic moment of the AMR layer would be canted at $\approx 45^\circ$ from the longitudinal direction.

A typical magnetoresistive resistor is constituted by thin film stripes. The resistivity *R* of a magnetoresistive stripe depends on the angle between the directions of electric current (*I*) and magnetisation (*M*) according to the following eq.IV.2

IV.2) $R = R_0 + \Delta R_0 \cos^2\theta$

where ΔR_0 describes the strength of the magnetoresistive effect. The relationship between an external field H_y and angle α is determined by the geometrical dimensions of the stripe and the magnetic anisotropy of MR metal. This is taken into account by introducing a field H_0 that represents the demagnetising and anisotropic field leading to

$$IV.3) \quad \begin{cases} \sin^2\alpha = H_y^{\,2} / H_0^{\,2} & for \quad H \le H_0 \\ \sin^2\alpha = 1 & for \quad H \ge H_0 \end{cases}$$

The characteristic of a magnetoresistive stripe as a field sensor is:

$$IV.4) \quad R = R_0 + \Delta R_0 \left(1 + \frac{H_y^{\,2}}{H_0^{\,2}} \right) \qquad for \quad H \le H_0$$

A linear characteristic of the magnetoresistive sensor is required to measure a small magnetic field. The linear behaviour of the magnetoresistive sensor is achieved by using a "Barber pole" geometry. The stripes are covered with aluminium bars having an inclination of 45° to the stripe axis. Aluminum has a low resistivity compared to MR metal.

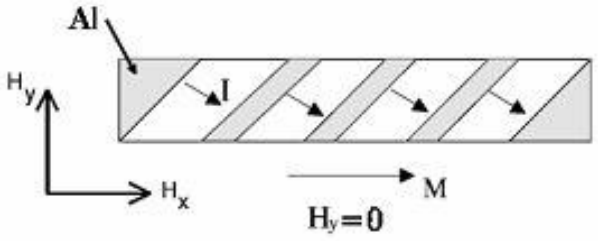

Figure IV.4 Covering the magnetoresistive stripe with "Barber poles" consisting of aluminium changes the direction of the current. This does not influence the direction of magnetisation.

Therefore the Barber poles cause a change of the current direction. The angle between current and magnetisation is shifted by 45° as shown in Figure IV.4. The relationship between resistance and magnetic field is now

$$IV.5) \quad R = R_0 + \frac{\Delta R_0}{2} \pm \Delta R_0 \left(\frac{H_y}{H_0} \right) \sqrt{1 + \frac{H_y^{\,2}}{H_0^{\,2}}}$$

A linear characteristic of the sensor is given around $H_y^{\,2} / H_0^{\,2} = 0$. The sign in this equation is determined by the inclination of the "Barber poles" (±45°) to the stripe axis. The characteristic of a sensor with and without Barber poles is presented in Figure IV.5.

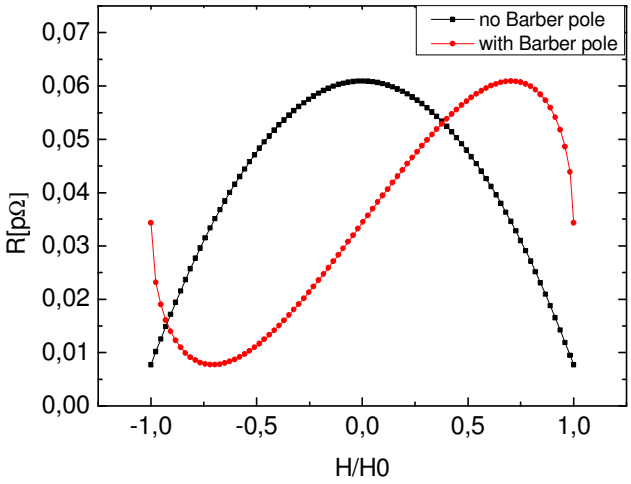

Figure IV.5 Characteristics of magnetoresistive sensors. The Barber pole structure enables a linear behaviour of the sensor for a small magnetic field. Data from Table III.1 applying eq.IV.5

Our aim is to reproduce the behaviour of a magnetoresistive sensor constituted by 40 Co/Cu bilayer with a "Barber poles" structure. The output characteristic has been derived from the experimental data of the Co/Cu bilayer shown in Table III.1 [data extracted from *Ref. III.24*]. The resistance values consider $R_0 = R_P$, i.e. in the absence of external applied field, the mutual layer direction is parallel and the overall resistance is minimal, while in the presence of field the mutual layer direction is antiferromagnetic and the overall resistance excursion, $\Delta R_0 = R_{AP} - R_P$, is the difference between the maximum value that it assumes during antiparallel configuration and the minimum one. The values of R_{AP} and R_P resistances were calculated using eq.III.32 and eq.III.34. The applied field H_0 is varying in the range $0 \div 3 kA/m$, the choice of the values is due to the linearity and application field of commercial sensors.

The magnetometer sensitivity to the magnetic field is several orders of magnitude less than the Earth magnetic field and other electromagnetic interferences. Usually in NDE applications in shielded environment, the low intensity of the field associated to the defect (few *pT*) makes magnetometers not usable for this purpose. A possible approach in order to realize such measurements is to recombine electronically signals coming from two or more magnetometers (GMR). The more common technique requires to subtract the signal coming from two magnetometers in order to form a first order gradiometer electronic, like shown in Figure IV.6

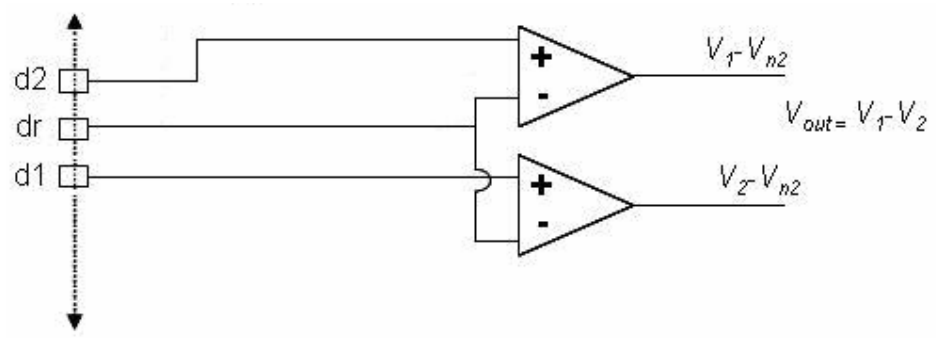

Figure IV.6 First order gradiometer from single magnetometers GMR.

The electronic gradiometer requires a third sensor GMR as reference in order to measure the level of the magnetic background interference. The reference device is situated between the other two sensors and enable the feedback on every measured magnetic field to the two sensors that form the gradiometer. In this way the gradiometer does not suffer from the magnetic background noise. The optimal configuration of measure is that shown in Figure IV.7.

A quantitative analysis of the signal received from the first order planar gradiometer can be obtained starting from the distribution of the field *B* generated from the magnetic dipole *m* within the test sample:

$$B(\vec{m},\vec{r}) = \frac{\mu_0}{4\pi}\left[\frac{3(\vec{m}\cdot\vec{r})\vec{r}}{r^5} - \frac{\vec{m}}{r^3}\right] \qquad \textit{IV.6)}$$

where *m* (Am^2) is the dipolar magnetic moment and *r* is the distance from the dipole and the measurement point.

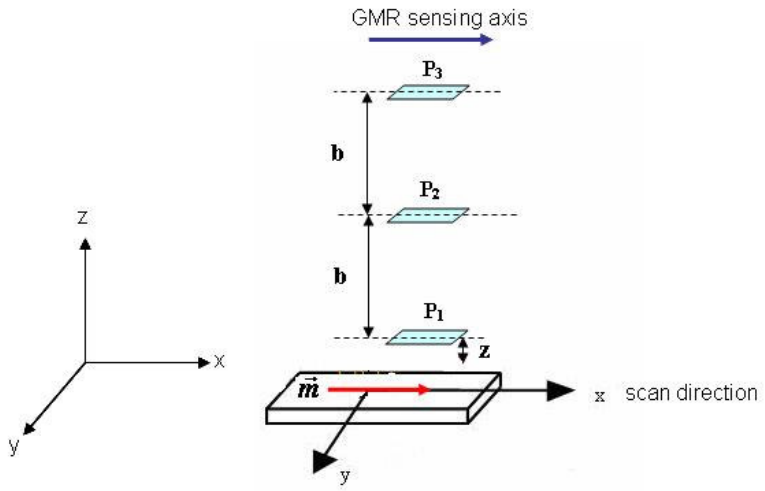

Figure IV.7 Gradiometric configuration using three individual magnetometers/chip GMR.

The second order gradiometer output ($\partial^2 B_x/\partial^2 x$) is given as two gradiometers differential with the mutual distance *b* (baseline). The sensing axis of the GMR probe is coplanar with the surface of the specimen. Thus, field components that are perpendicular to the sensitive axis have negligible effect on their output. We consider that the magnetic moment of dipole lies in the x-y plane and calculate the magnetic field gradient along the scan direction, e.i. in the following equation, both the scan direction and the magnetic moment are chosen parallel to the *x*-axis. The magnetic field *B* in Cartesian coordinates is given by

$$B_x = \frac{\mu_0 m}{4\pi}\left[\frac{3x^2}{r^{5/2}} - \frac{1}{r^{3/2}}\right] \qquad IV.7)$$

In accordance with the above equation the magnetic gradient field can be described as

$$\left.\frac{\partial B_x}{\partial x}\right|_{y,z=0} = \frac{\mu_0 m}{4\pi}\frac{3x\left(3z^2 - 2x^2\right)}{\left(x^2 + z^2\right)^{7/2}} \qquad IV.8)$$

Whereas the only useful component of the field *B* is the one that lies in the plan of the sensor in the scan direction, generated by magnetic dipole *m*, thus the field of gradiometer is obtained according the law $G = B_1 - 2B_2 + B_3$ with all three sensors oriented in one direction (for the measures *z=2mm*, baseline=*11mm*).

The measurement system is composed of a GMR gradiometer consisting of three GMR magnetometers AA005-02 (NVE), a voltage generator Keithley 2400, two operational amplifiers (unitary gain), a Low-Noise Preamplifier (EG&G Model 5113), a B Series Multifunctional DAQ (National Instruments) and is supported by LabVIEW software. The gradiometric system is powered with $8V$ DC voltage by the DC voltage generator keithley 2400. The output of each device is taken, using a coaxial cable. The output signals are themselves as input of the two operational amplifiers in order to achieve $B_1 - B_2$ and $B_2 - B_3$. During measurements, the outputs of the amplifiers are filtered by a second-order low-pass filter with a cutoff frequency of $30Hz$ using a EG&G Model 5113 low-noise preamplifier that allows to obtain $G = (B_1 - B_2) - (B_2 - B_3) = B_1 - 2B_2 + B_3$. A Labview data acquisition program collects data from the output of the filter via a National Instruments 16 bit analog-to-digital converter. For each scanning cycle, samples of filtered signal were collected at a sampling rate specified by the user. Time domain is converted into space domain taking into account the relation between number of samples, sampling rate, scanning velocity, and scanning length. Finally, for visualization of these results, 2-D maps representing the output voltage of the sensor as a function of displacements are plotted.

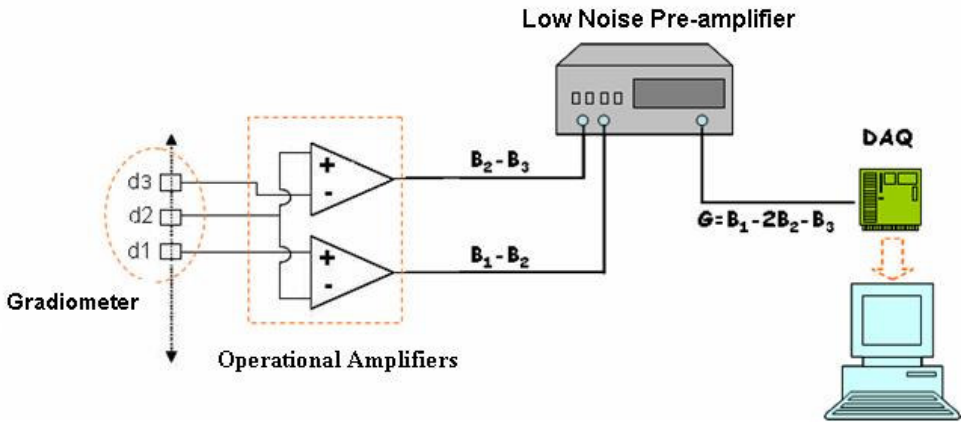

Figure IV.8 The gradiometer configuration and the data acquisition system consisting of a GMR gradiometer made of three GMR magnetometers AA005-02 (NVE), two operational amplifiers (unitary gain), a Low-Noise Preamplifier (EG&G Model 5113), a B Series Multifunctional DAQ (National Instruments) and supported by LabVIEW software.

The system is devoted to operate in a typical laboratory magnetic noise environment This means the power line interference with its $50Hz$ peak due to current flowing in and to electronic appliances has

to be taken into account in the measurement. Thus, the largest bond of a so diversified system is the environmental noise and the 1/f of the whole electronics involved. The risk is to have a system which results theoretically and electronically valid but with a noise (heat, intrinsic, cables) higher than its sensitivity. In fact, the ultimate low-field limit on any magnetic sensing system is noise. If the signal to noise ratio is less than one, it is difficult to have a meaningful measurement. Fortunately, there are several methods of improving the signal to noise ratio if one understands the sources of the noise [*Ref. IV.9*]. Noise can divided into two categories, inherent and transmitted. The sensor produces inherent noise while transmitted noise is due to the coupling between the sensing system and the outside world. Inherent noise can include such things as sensor and amplifier offset, thermal noise, and 1/f noise. Transmitted noise includes magnetic fields from unwanted sources and electrical noise from external sources picked up by the sensing system.

Therefore, the assessment that must precede any measurement is the noise of the system. As comparison, first we analyze the noise for a single GMR magnetometer then assess the one of the whole system.

IV.2 Sampling and numerical processing of the GMR magnetometer output

The Noise Power Spectrum Density (NPSD) analysis is carried out using a spectrum analyzer HP 35670A and the result is reported in the following figure

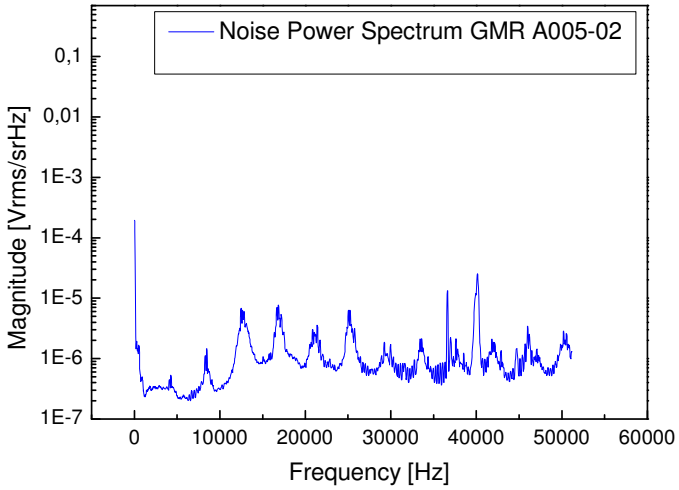

Figure IV.9 Single GMR magnetometer NPSD retrieved from a single window in frequency (1600 lines and frequency span ~15mHz ÷ 52kHz).

The above figure shows the full spectrum (frequency span about $15mHz \div 52kHz$). One can note, the value of the background increases for frequencies higher than $10kHz$ varying from $\sim 2 \cdot 10^{-7}$ to $\sim 4 \cdot 10^{-7}$. In the table below, we reported the main observed frequencies

Main Frequencies [Hz]	Peak Amplitude [$V_{rms}/\sqrt{Hz}$]	Peak Amplitude [%]
50.141	$3.685 \cdot 10^{-4}$	100
8480	$2 \cdot 10^{-6}$	0,54
12730	$2.167 \cdot 10^{-5}$	5,88
16946	$3.309 \cdot 10^{-5}$	8,98
25188	$1.064 \cdot 10^{-5}$	2,89
36630	$2.659 \cdot 10^{-5}$	7,21
40108	$3.772 \cdot 10^{-5}$	10,23
21516	$6.062 \cdot 10^{-6}$	1,645047
29248	$3.237 \cdot 10^{-6}$	0,878426
33430	$3.885 \cdot 10^{-6}$	1,054274
42044	$3.174 \cdot 10^{-6}$	0,86133
46274	$5.097 \cdot 10^{-6}$	1,383175
50474	$5.102 \cdot 10^{-6}$	1,384532

Table IV.2 Main noise peaks in single GMR magnetometer NPSD (frequency range ~15mHz ÷ 52kHz). The amplitude data do not take account of the different values of the background.

The next goal is to confirm of what is seen in the results of the spectrum analyzer and to check if there are significant noise components which make necessary filtering procedure, i.e. high-frequency noise with high dB level spurious down to low-frequency. Therefore, the GMR output measurement has been repeated by sampling the signal from the DAQ and processing the numerical data obtained for each sampling frequency by the signal processing tool provided by Matlab. This analysis has been completed taking into account several factors: signal characteristics as peak frequency of interest, DAQ technical characteristics, FFT algorithm and signal windows.

The Shannon (or Nyquist) theorem provides the necessary condition to return an analog signal after sampling, through a D/A converter. This means $f_c \geq 2f_s$ where f_s is the signal highest frequency and f_c is the sampling frequency. If sampling does not satisfy that requirement, the high frequency components are under sampling and they can be found again as low frequency components of the sampled signal (aliasing). The signal power density spectrum discloses the high amplitude peaks and their sampling frequencies

Main Frequencies [Hz]	**Peak Amplitude [$V_{rms}/\sqrt{Hz}$]**	**Min Sampling Frequencies [Hz]**
50.141	$3.685 \cdot 10^{-4}$	100.282
8480	$2 \cdot 10^{-6}$	16960
12730	$2.167 \cdot 10^{-5}$	25460
16946	$3.309 \cdot 10^{-5}$	33892
25188	$1.064 \cdot 10^{-5}$	50376
36630	$2.659 \cdot 10^{-5}$	73260
40108	$3.772 \cdot 10^{-5}$	80216

Table IV.3 Main noise peaks in single GMR magnetometer NPSD and the respective sampling frequencies.

As reported in the Table IV.4 below, the maximum sampling frequency of the data acquisition card is not limiting the signal noise analysis. The difference between two adjacent levels (Resolution) is $20V/2^{16} = 6{,}104e^{-4}\ V$, a level which may be considered acceptable for the purposes of the measure. After the analog to digital conversion by A/D converter (DAQ), the sequence of values obtained from the signal may be processed as an array of integers uniformly distributed on the times axis.

Sampling Frequencies	200 kS/s
Resolution	16 bits
Analogic Input - Max Range	-10..10 V

Table IV.4 DAQ main technical characteristics

The signal spectrum represented in this way may be calculated using the FFT providing the number *N* of the samples to be analyzed. In our treatment using the Matlab Signal Processing tool, *N* is set to maximum ($2^{10} = 1024$ samples). The FFT representation gives the same importance to both low and high frequencies. To avoid the samples spectral dispersion, it is necessary to apply a digital filter to the sampled signal before its FFT algorithm processing. The filter multiplies the signal by a weight function so that is zero to the extreme of each window. The most common used windowing is the Hanning window. Unlike the other (Gauss, triangular and so on), this one ensures the equivalence between the primary signal energy and the weighted one. To avoid the analysis distortion, it is necessary to translate all the successive windows in order to overlap them. This solution gives the right weight for those underestimated samples in previous windowing. For the Hanning window, the chosen overlap is 99%, that is nearly a window repetition each samples.

Therefore, since our intention is the GMR device background noise sampling, the sampling frequencies are numerous, starting from a sampling frequency $f_C = 1kHz$ up to $100kHz$ with $5kHz$ range. This is because the background white noise contains the spectral components for all frequencies. Below, there are only the results for maximum sampling frequency, it must be $f_c \geq 2f_s$ assuming $f_c = 100kHz > 80216Hz = 2f_s$ with f_s =40108*Hz*, noise peaks maximum frequency, and f_c=100*kHz* < 200*kHz*, DAQ maximum sampling frequency. The following figures report the Matlab Signal Processing results.

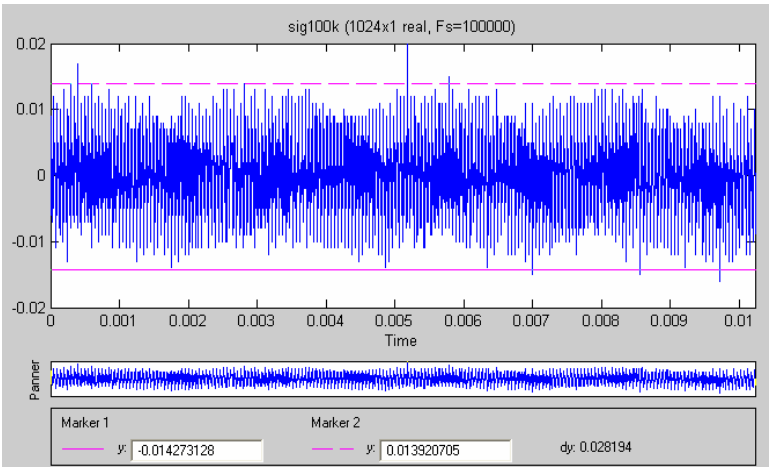

Figure IV.10 Numerical sample from an f_c= 100KHz sampling procedure.

The FFT algorithm and the windowing processing highlight the presence of secondary peaks (amplitude 5.1855504·e^{-9}, frequency 20214.844*Hz*).

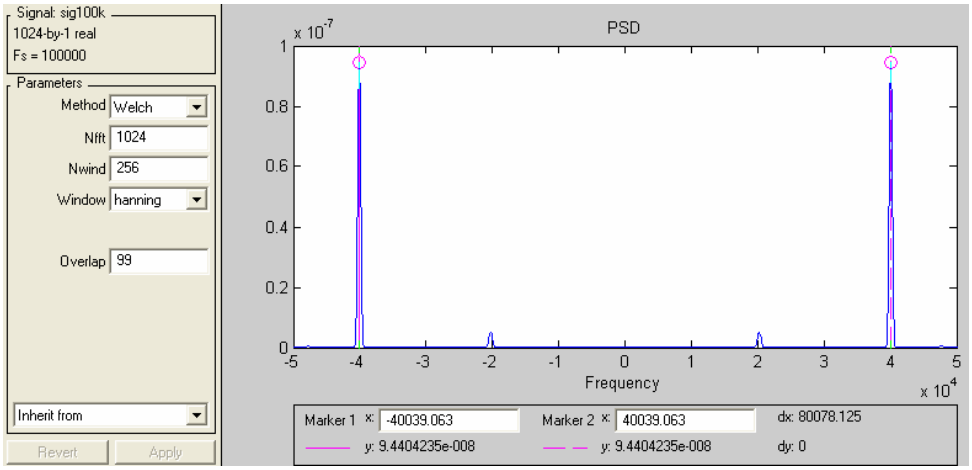

Figure IV.11 Linear representation in the [-fs/2, +fs/2] frequency range

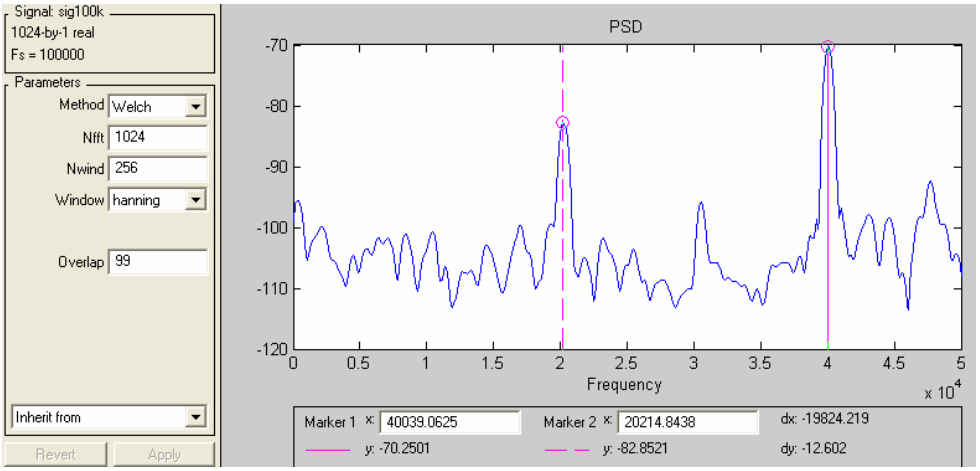

Figure IV.12 dB representation in the [0,+fs/2] frequency range

	Main Peaks [Hz]	**Main Peaks [dB]**	**Background [dB]**
f_c = 100kHz	40039.063	-70.2501	-95 a -113
	20214.844	-82.8521	
	47753.906	-92.424251	

Table IV.5 Summary of Hanning windowing processing of the single GMR magnetometer noise spectrum.

As first analysis result, it should be noted that those components, which seemed to be external "high" frequency noise sources ("high" when compared to the acquired DC signal) after the digital signal processing are reduced to a background noise characterized by minimum amplitude level peaks $-70 \div -93 dB$. The noise final graph allows to compare the results, reported to the same background level (Figure IV.13):

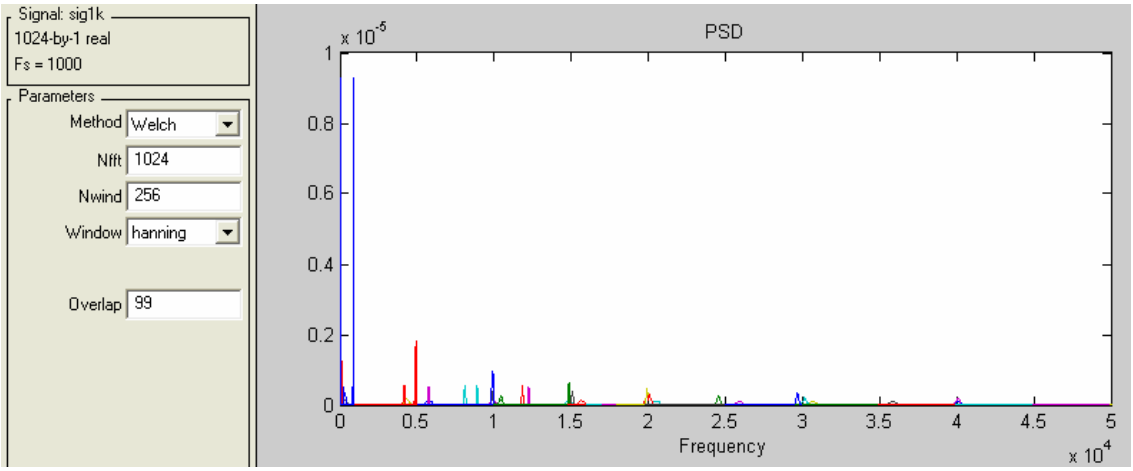

Figure IV.13 Linear representation in the [0, +fs/2] frequency range.

From Figure IV.13 and as shown in the Table IV.6 below, no irregularities from spurious components were found, and no noise components due to some external source, thus, the GMR noise assumes a typical *1/f* behaviour, in which the highest components are at low frequencies.

Main Peaks [Hz]	**Main Peaks [dB]**
80.078125	-50.325485
239.25781	-62.87291
265.625	-72.86566
398.4375	-73.359661

Table IV.6 Main peaks for [0,+fs/2] frequency range.

By changing the graph view using a double logarithmic scale, it is possible to analyze the results in a more appropriate frequency range (DC and low frequencies up to 10khz). The Figure IV.14 graph shows this passage.

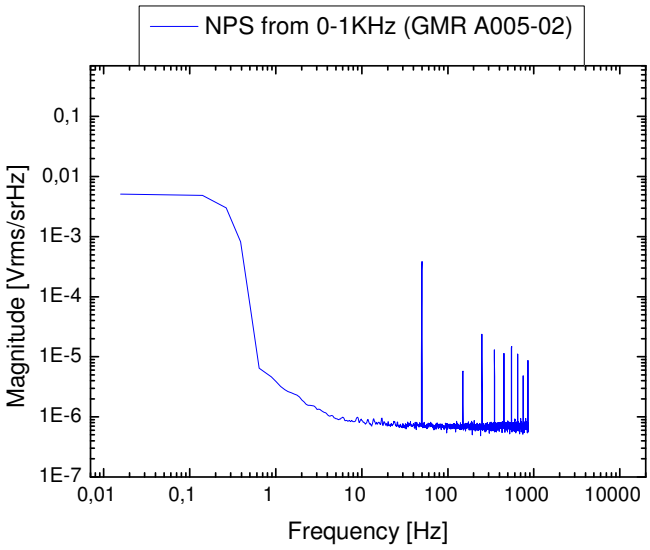

Figure IV.14 NPSD detail in the ~15mHz ÷10kHz range.

Main Frequencies [Hz]	**Noise Amplitude [$V_{rms}/\sqrt{Hz}$]**
DC ÷ $140 \cdot 10^{-3}$	$5.1 \cdot 10^{-7}$
50.141	$3.685 \cdot 10^{-4}$

Table IV.7 Main peaks for NPSD in the ~15mHz ÷10kHz frequency range.

Measured magnetic noise spectra of our laboratory showed two acceptable frequency ranges: 20 to 40*Hz* and 60 to 110*Hz*. In Figure IV.14 all 50*Hz* multiple frequencies up to 1*kHz* are evident and the main noise source is the *1/f* noise. *1/f* noise is an important source of inherent noise in all conductors. This noise is due to point to point fluctuations of the current in the conductor [*Ref. IV.11*]. It is proportional to the inverse of the frequency and often dominates below 100 Hz. At the lowest frequencies it is difficult to distinguish it from drift. While thermal noise is independent of current and exists even without current, *1/f* noise is proportional to the current and increases with increasing current. Bandwidth limitation, especially on the low frequency end will decrease *1/f* noise. As with any random noise source, averaging a repetitive signal will increase the signal to noise ratio by the square root of the number of singles averaged

Therefore, the noise main component is due essentially to the network that is indispensable unless supply batteries are used. We try to limit the 50*Hz* effect using a low pass filter from a pre-amplifier (EG&G Model 5113 Low-Noise Preamplifier). Thus, during the results evaluation, the pre-

amplifier characteristics have to be taken into account. Observing the pre-amplifier data sheets reported in Figure IV.15, we know how to proceed to reduce the noise from the network.

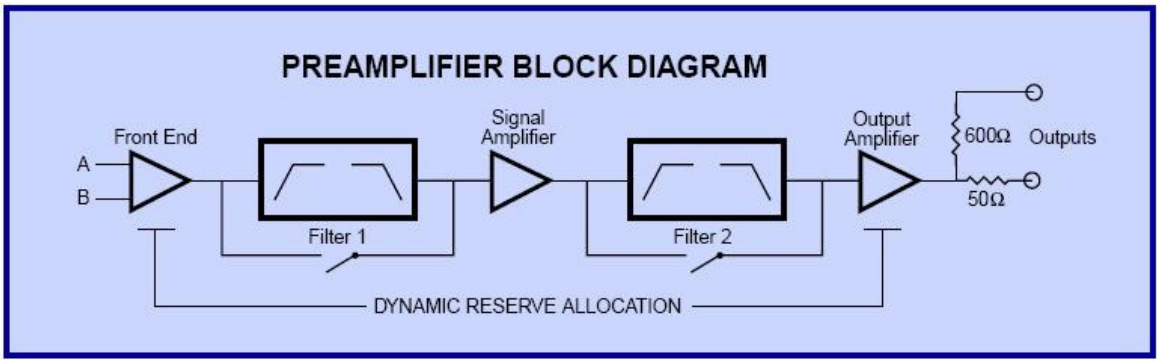

Figure IV.15 Pre-amplifier functional scheme.

The input voltage noise is roughly a resistor of 1000Ω, about $4nV/\sqrt{Hz}$. For sources/inputs impedance less than 1000Ω, the output noise will be less than the input voltage noise. For the GMR magnetometer, the input impedance is about $5k\Omega$ while the GMR gradiometer, as three magnetometer connected in parallel, has an input impedance of 1667Ω, therefore, both outputs will not be affected by the amplifier presence. The Figure IV.16 shows a typical behaviour for the amplifier input voltage noise.

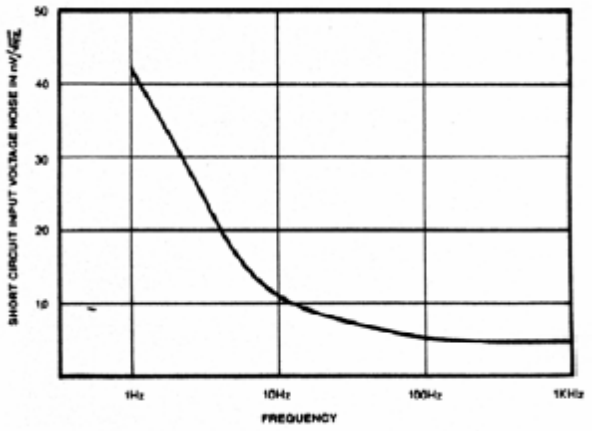

Figure IV.16 Pre-amplifier voltage noise in input.

It should be noted that the voltage noise increases at low frequencies, *1/f* noise behaviour. For this reason, the passage of the signal processing could be compromised from amplifier influence just in

the band of interest, DC and low frequencies up to 10*kHz*. The PAR insertion is validated by the measurements later displayed. The preamplifier includes two identical first order RC filters with configurable cut-off frequency and filter typology, High Pass filter HPF or low pass filter LPF, the filter maximum bandwidth is 1*MHz*. Since our purposes is the devices noise reduction, this is possible introducing a LPF whose slope profile (roll-off) is reproduced in Figure IV.17.

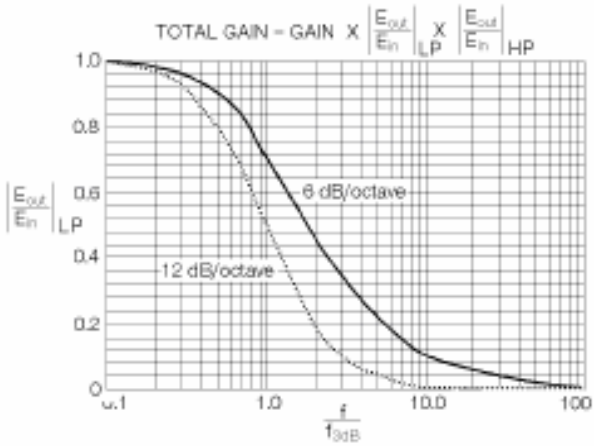

Figure IV.17 Low-Pass filter Amplitude vs. Normalized Frequency response.

It is important to note that the gain displayed from the PAR is considered without any active filter. Of course, the gain with the filters is a function of the frequency and of the output filter, i.e. the gain for each filter section is x0.707 (- 3*dB*) of the displayed gain. The results coming from PAR insertion with several filter applications are the following noise spectrum graphs.

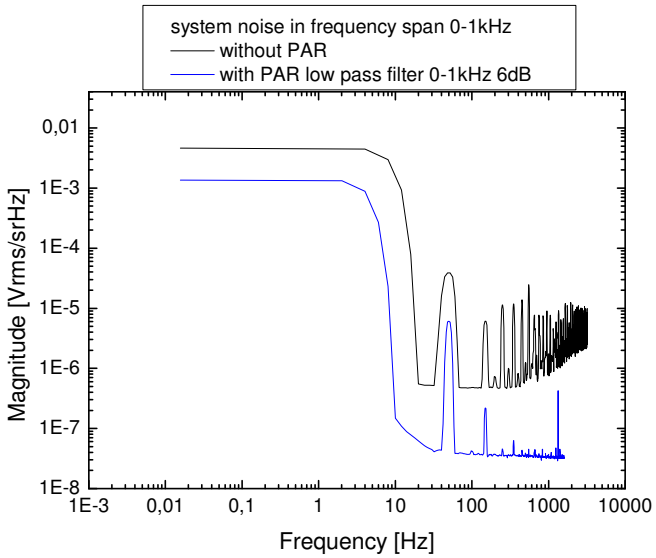

Figure IV.18 NPSD detail in the range ~15mHz ÷1kHz. It shows the noise of the system (in black) without power supply while (in red and blue) the powered system with a low pass filter 0÷1kHz in output. The frequency range 0÷1kHz is completely passing for the signal of interest

Despite the 0÷1*kHz* LPF is completely passing for the noise in the range of interest, it is possible to see a real improvement due to the progressive flattening of background noise and the lost of 50*Hz* multiple components. The best result is obtained with attenuation of 12*dB/octave*, as shown in the Table IV.8.

LPF 0-1kHz 12dB/oct	**DC Level [$V_{rms}/\sqrt{Hz}$]**	**Background [$V_{rms}/\sqrt{Hz}$]**	**50Hz [$V_{rms}/\sqrt{Hz}$]**
Gain x1	0.00136	$1.48 \cdot 10^{-7} \div 4 \cdot 10^{-8}$	$6.079 \cdot 10^{-6}$

Table IV.8 Main peak for NPSD in the ~15mHz ÷1kHz frequency range with a 0÷1kHz 12dB/oct. LPF.

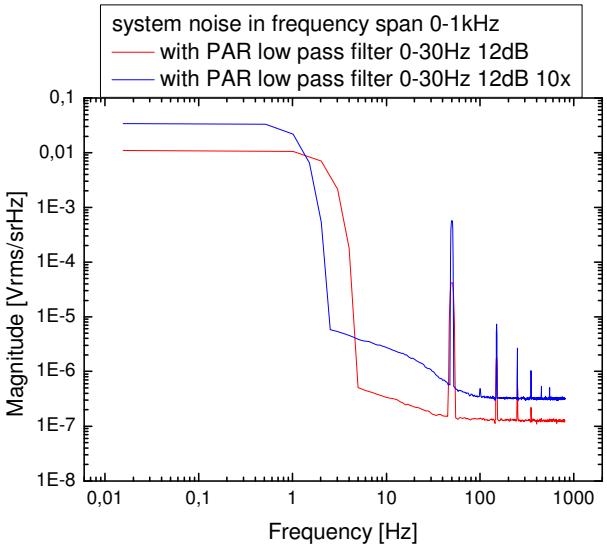

Figure IV.19 NPSD detail in the range ~15mHz÷1kHz with a DC÷30Hz 12dB/octave LPF.

Keeping 12*dB/octave* attenuation, the 0÷30*Hz* LPF filter, i.e. with a narrow frequency range, reveals a higher noise level compared to the previous one

LPF 0-30Hz 12dB/oct	**DC Level [$V_{rms}/\sqrt{Hz}$]**	**Background [$V_{rms}/\sqrt{Hz}$]**	**50Hz [$V_{rms}/\sqrt{Hz}$]**
Gain x1	0.0109	$5.11 \cdot 10^{-7} \div 1.5 \cdot 10^{-7}$	$4.23 \cdot 10^{-5}$

Table IV.9 Main peak for NPSD in the ~15mHz ÷1kHz frequency range with a DC÷30Hz 12dB/oct LPF.

Obviously, the noise level further increases with the amplification level (see blue curve). Indeed, the noise level should fall using a narrow frequency range filter. To have a further confirmation the filter bandwidth has been decreased up to 3*Hz*.

LPF 0-3Hz 12dB/oct	**DC Level [$V_{rms}/\sqrt{Hz}$]**	**Background [$V_{rms}/\sqrt{Hz}$]**	**50Hz [$V_{rms}/\sqrt{Hz}$]**
Gain x1	0.00192	$9.4 \cdot 10^{-8} \div 6.4 \cdot 10^{-8}$	$8.03 \cdot 10^{-7}$

Table IV.10 Main peak for NPSD in the ~15mHz ÷1kHz frequency range with a DC÷3Hz 12dB/oct LPF.

The Figure IV.18 and Table IV.8 summarize the comparison of the various filters.

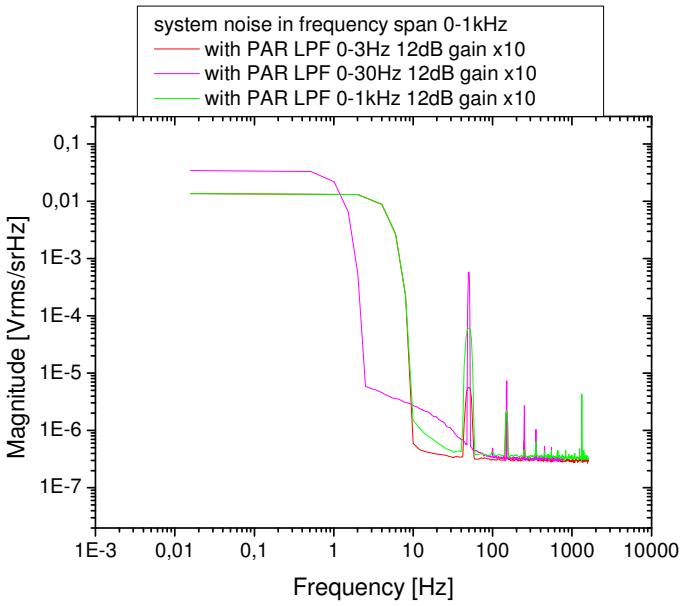

Figure IV.20 LPF final comparison.

Gain x10	DC Level [$V_{rms}/\sqrt{Hz}$]	Background [$V_{rms}/\sqrt{Hz}$]	50Hz [$V_{rms}/\sqrt{Hz}$]
LPF 0-1kHz 12dB	0.0136	$1.48 \cdot 10^{-6} \div 4.33 \cdot 10^{-7}$	$6.08 \cdot 10^{-5}$
LPF 0-30Hz 12dB	0.0341	$5.82 \cdot 10^{-6} \div 5.67 \cdot 10^{-7}$	$5.79 \cdot 10^{-4}$
LPF 0-3Hz 12dB	0.0134	$5.88 \cdot 10^{-7} \div 3.38 \cdot 10^{-7}$	$5.63 \cdot 10^{-6}$

Table IV.11 Main peaks for NPSD in the ~15mHz ÷1kHz frequency range for all LPF tested configuration.

In presence of pre-amplifier, the noise power density spectrum of the gradiometric configuration realized by three GMR AA005-02 with a mutual distance of 13*mm* has been compared with the NPSD of the single magnetometers,

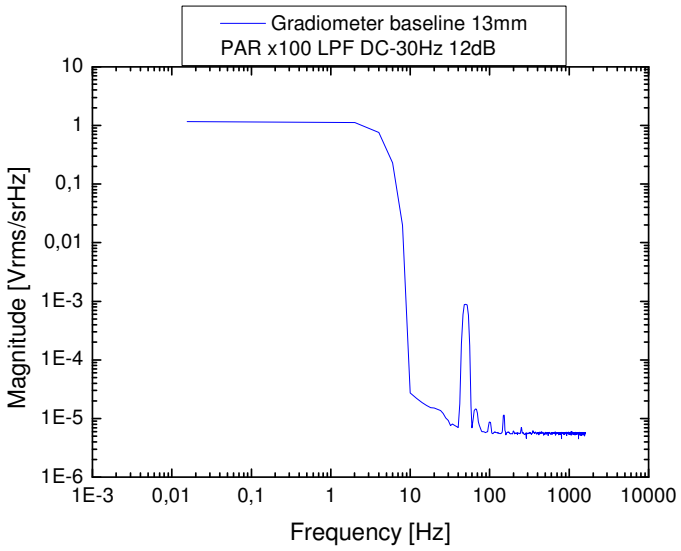

Figure IV.21 NPSD detail for the gradiometric configuration in the range ~15mH÷1.6kHz with DC÷30Hz 12dB/octave LPF.

It should be noted that we preferred the use of a DC÷30*Hz* 12*dB/octave* (100x gain) LPF instead of DC÷3Hz 12*dB/octave* LPF that ensures lower background and DC noise level (see table above) to allow greater dynamic measurements. The values from the graph are:

Gain x100	**DC Level [$V_{rms}/\sqrt{Hz}$]**	**Background [$V_{rms}/\sqrt{Hz}$]**	**50Hz [$V_{rms}/\sqrt{Hz}$]**
LPF 0-30Hz 12dB	1.1618	$2.74 \cdot 10^{-5} \div 7.02 \cdot 10^{-6}$	$8.93 \cdot 10^{-4}$

Table IV.12 Main peak for NPSD in the ~15mHz ÷1kHz frequency range with a DC÷30Hz 12dB/oct LPF.

The following graph compares the results of the gradiometric configurations with the noise spectrum of the individual sensors:

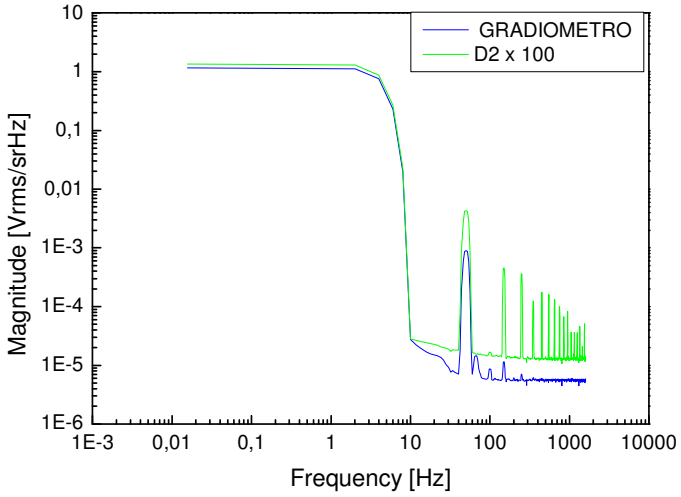

Figure IV.22 NPSD comparison between the single magnetometer and the gradiometric configurations in the frequency range ~15mHz ÷1.6kHz .

Comparing, with the same operating conditions, the spectrum of the single magnetometer (D2x100 in the label of Figure IV.22) with the one shown by the GMR gradiometer, it is possible to note how the adopted configuration allows to:

- decrease the background noise level for $10Hz$ frequency component (from $1.8 \cdot 10^{-5}$ to $7.02 \cdot 10^{-6}$ amplitude level);
- remove the $50Hz$ peak level and its components (from 0.0042 to $8.93 \cdot 10^{-4}$ amplitude level);
- maintain the DC noise level ($1.1618 V_{rms}/\sqrt{Hz}$ with a 100x gain).

We must consider that transmitted noise sources include any voltages picked up by the circuit as well as any magnetic signals picked up by the sensor which are not part of the desired magnetic signal. Any time varying magnetic field will not only produce a signal in a magnetic sensor, it will also induce a voltage in any circuit loop proportional to the circuit loop area and the time rate of change of the magnetic field. To minimize this inductive pick up, good circuit practices must be followed including minimizing any potential circuit loops and placing amplification as close to the sensor as possible. Electrical currents generate magnetic fields. Therefore, there are usually stray $50Hz$ magnetic fields in any industrial location. The increasing use of computers and other equipment with rectifiers-fed capacitor-input power supplies results in non-sinusoidal currents that produce harmonics of *50*Hz. Any moving or rotation magnetic material in equipment will produce a time varying magnetic field at frequencies characteristic of their period. The Earth's magnetic field itself, and its slow random variation is a source of noise if extremely low frequency magnetic fields are of interest. Transmitted magnetic noise sources are usually best minimized by filtering and if

practical, using magnetic shielding. Anyhow, our aim is to develop a measurement system characterized by simple control electronics with the measurement reliability in a not electromagnetically shielded laboratory. When measuring fields from a dipole source close to the sensor, a second sensor can be located at a distance at least twice as far from the dipole. The difference between the two signals, when adjusted for differences in sensitivity will be at least 7/8 the signal while cancelling out the signals from remote sources. When designing a magnetic sensor for searching for magnetic dipoles such as a permanent magnet or a buried surveying stake, it is difficult to differentiate the DC signal from the object sought from the DC signal from the Earth's magnetic field. The method described above of using two sensors in a differential mode can be used for our purpose. In fact, the use of GMR sensors in gradiometric configuration, together with the filtering technique, is mainly targeted to the elimination of the magnetic noise and to the increase of the signal to noise ratio.

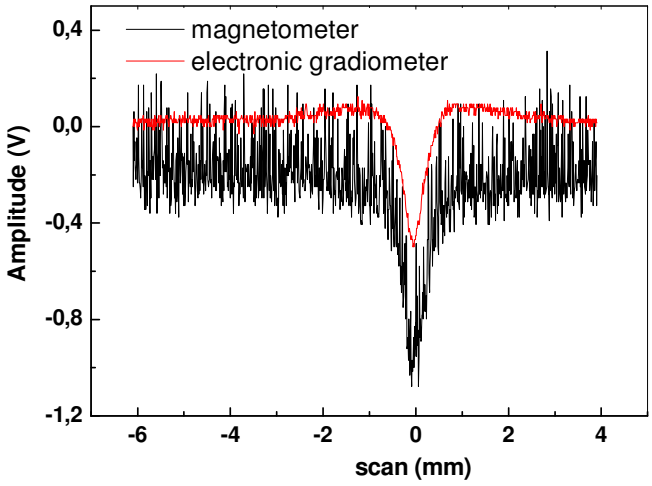

Figure IV.23 2nd order gradiometer response on a steel Fe360 sample characterized by an electro-erosion cut.

The Figure IV.23 confirms, as said before, the net improvement in the signal to noise ratio that is accomplished with the use of the gradiometric configuration.

IV.3 Tuning of the gradiometric system

Taking into account the NPSD measurements and the procedures used to reduce the environment noise, it was possible to trace the intrinsic magnetic field sensitivity for the single GMR magnetometers. This is defined as the ratio between the output voltage and the field intensity. This conversion factor has been obtained starting from known conversion factor of a flux gate probe (C.F. 143000*V/T*) using it as calibration sensor. The measure has been carried out setting the magnetometer and the flux gate sensor at the solenoid centre and varying the current. The Table IV.13 shows the values recorded during the measurement

Current (A)	Flux Gate Output (V)	B Flux Gate (T)	GMR Output (V)
0.005	0.72	5.03497e-6	0.00147
0.008	1.68	1.17483e-5	0.00155
0.009	1.96	1.37063e-5	0.0016
0.01	2.24	1.56643e-5	0.00164
0.02	5.2	3.63636e-5	0.00211
0.025	6.6	4.61538e-5	0.00241
0.03	8	5.59441e-5	0.00265

Table IV.13 Experimental comparison between flux gate sensor output and GMR sensor output vs magnetic field.

A linear data fit gives the conversion factor of GMR magnetometer as 23.91608*V/T*:

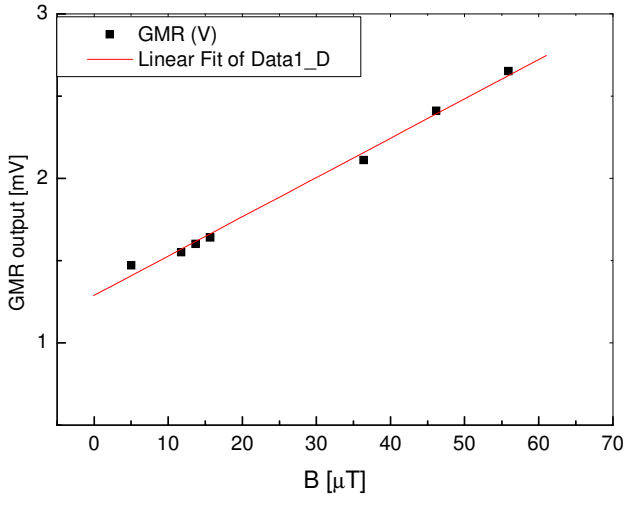

Figure IV.24 Linear data fit to calculate the GMR conversion factor.

However, the obtained value is much lower than expected. Therefore, the measurement has been repeated using the DC÷3*Hz* 12*dB/octave* LPF (250x gain). By applying the linear fit on the new data, it is possible to obtain a second value for the intrinsic magnetic field sensitivity of the GMR magnetometers, C.F. 5699.92*V/T*.

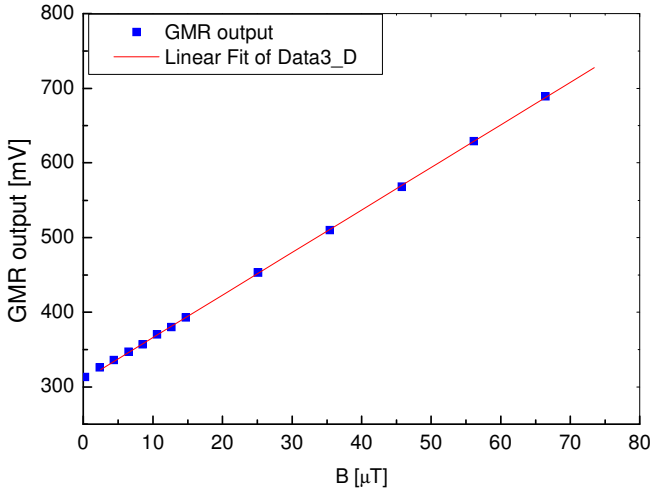

Figure IV.25 GMR intrinsic magnetic field sensitivity. Calculating the factor for conversion of GMR. Output is filtered by the pre-amplifier DC÷3Hz 12dB/octave LPF (250x gain).

This value, obtained using a filtering technique, shows a considerable increase of the signal to noise ratio. Furthermore, the GMR conversion factor, although lower than the one of the flux gate probe, demonstrates that this kind of sensor can have a promising sensitivity, that will be certainly increased in a gradiometric configuration.

In the following, we show data coming from measurements carried out using the configuration shown in Figure IV.8. These results allow to highlight the advantage of using an electronic gradiometer to improve the overall sensitivity of the system based on the GMR technology.
The sensitivity of a 1st order electronic gradiometer has been tested performing several scans on steel Fe360 samples, thickness 6*mm*, characterized by crossing cuts with different dimensions. The experimental scan system is realized using a step by step motor qualified to move the probe or the specimens. This is a low noise system, not affected by self magnetization, that allows scanning up to 5*kg* sample with a position accuracy of 0.1*mm*. The gradiometer baseline is 11*mm*. The distance between the core axis of the reference magnetic sensor, oriented in parallel with the surface of the

specimen, is about 3mm. In this configuration, the gradiometer measures the variations of the field in-plane components in the scan direction, the parallel component and the orthogonal one to the scanning direction. The probe motion and the data acquisition is completely automated. The control software works in LabVIEW environment. With this technique, it is possible to build the maps of the components $\partial B_x/\partial x$ and $\partial B_x/\partial y$ of the field **B** along the scanning direction, starting from an experimental data matrix 399×20. Figure IV.26 and Figure IV.27 show results obtained using the GMR system on a Fe360 sample characterized by a cut of dimensions 3*mmx*27*mm.* The sensor output is the dc component of the signal, from which the amplitude of the field created by the flaw is immediately extracted. In the presence of a defect, the output signal from the sensor is produced by the perturbation of the magnetic field path only.

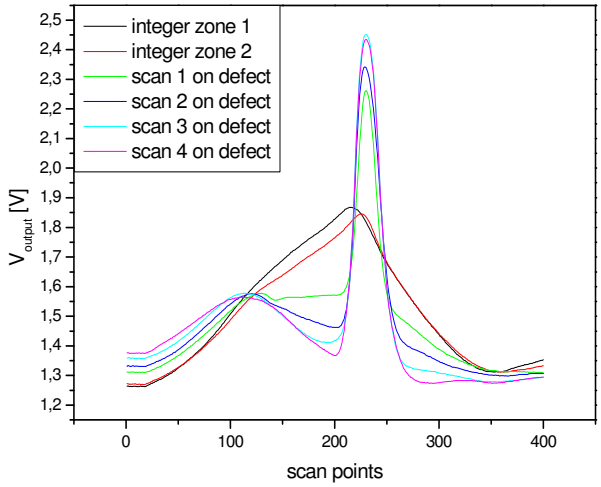

Figure IV.26 Different scans along x on Fe360 sample (cut dimensions 3mmx27mm). The scans show a typical GMR unipolar output where the sample is integer, while the output on the defect present maximum values.

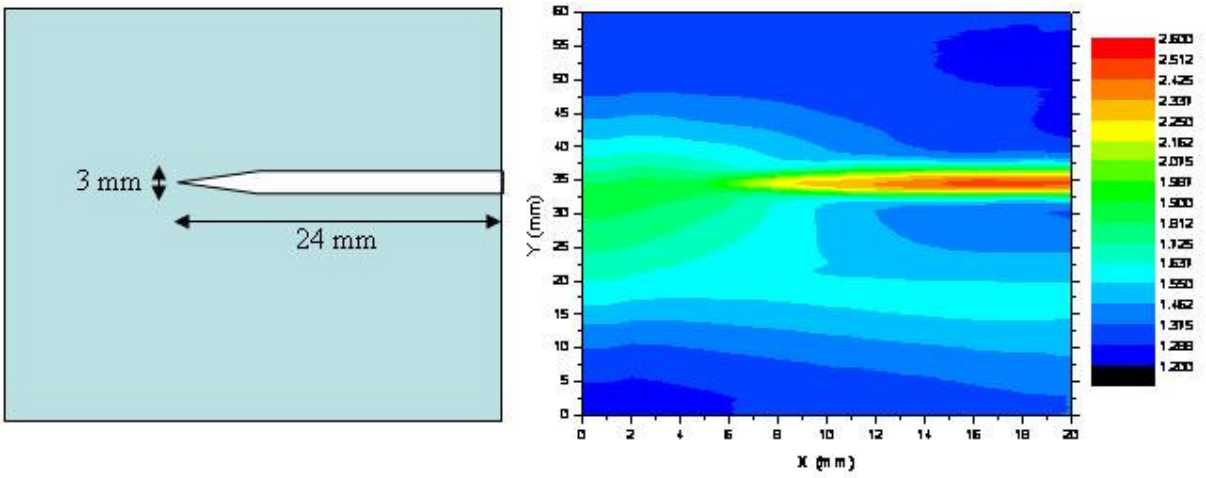

Figure IV.27 (Left) schematic design of the magnetized Fe360 sample showing the cut dimensions (3mmx24mm); (Right) map of the field distribution on the sample surface around the cut obtained from the GMR output signal.

A similar sample with a smaller cut (0.1mmx24mm) has been tested and results are shown in Figure IV.28 and Figure IV.29. The GMR gradiometer clearly revealed the cut, whereas a flux gate probe employed on the same sample was unable to detect the presence of the defect.

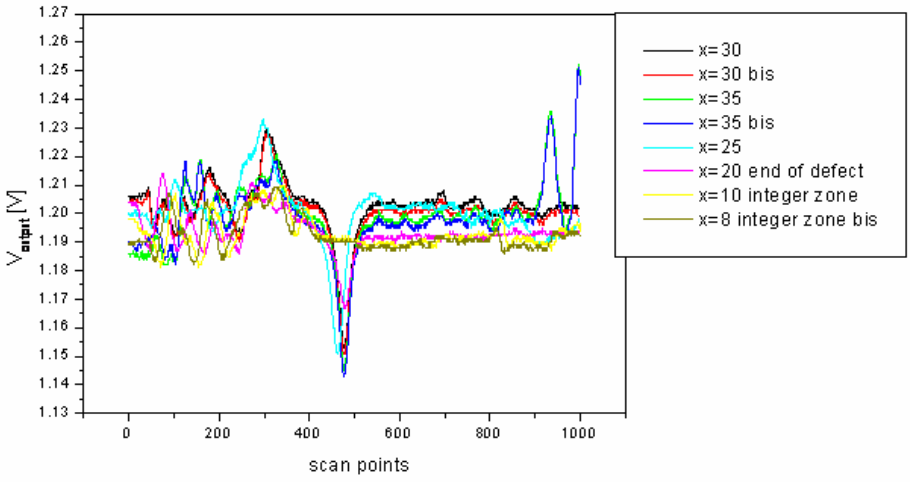

Figure IV.28 Scans along y on Fe360 sample (cut dimensions 0.1mmx24mm) for different x positions. In this case, scans show minimum values around the cut. The peaks are due to the field discontinuity on the sample borders.

The Figure IV.28 shows different single scans performed on the Fe360 sample. The output voltage behaviour is completely different in the presence of the defect where it presents a minimum. A full

bi-dimensional scan of the sample allows a surface map (Figure IV.29) that clearly shows the presence of the cut.

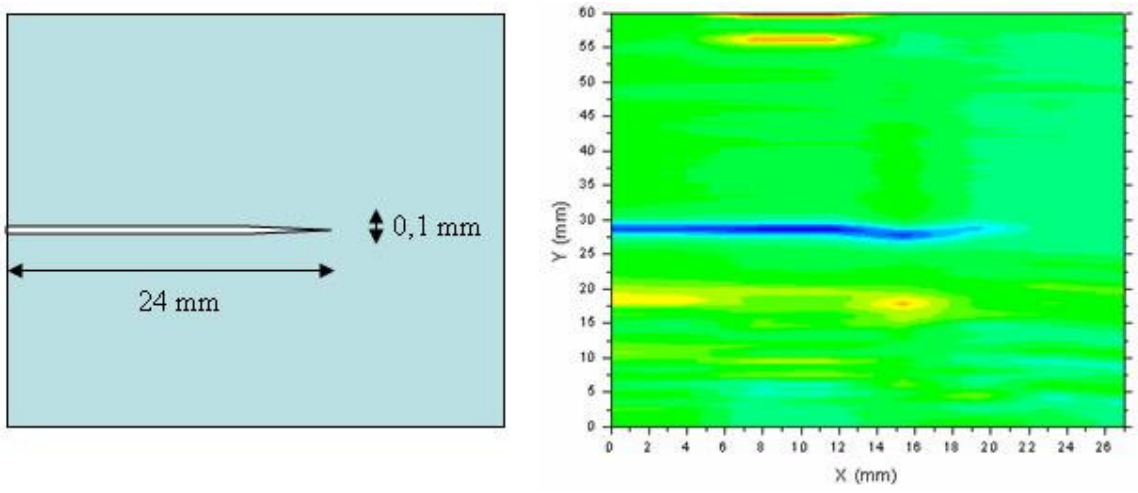

Figure IV.29 (Left) schematic design of the magnetized Fe360 sample showing the cut dimensions (0.1mmx24mm); (Right) map of the field distribution on the sample surface around the cut obtained from the GMR output signal.

Therefore, the combination of the gradiometric configuration of the sensor and a synchronous filtering of the output signal have definitely improved the stability and the resolution of the measurement system in a typical laboratory environment.

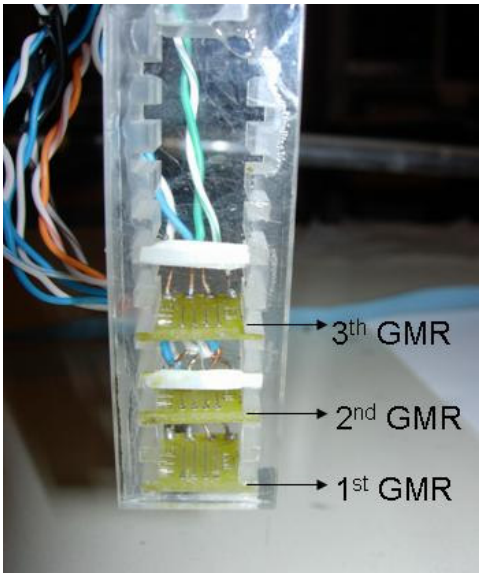

Figure IV.30 GMR 2nd order electronic gradiometer. It detects the in plane magnetic field component reducing the environmental noise.

Another interesting application of the GMR sensor in a gradiometric configuration is in the field of material characterization and magnetic microscopy.

Permanent magnet films based on highly anisotropic rare earth–transition metal phases like $SmCo_5$ are promising materials for structured micro-electromagnetic devices, when strong magnetic fields and high coercivities are needed. They may also find application in magnetic recording, as future miniaturization requires higher anisotropies to avoid a superparamagnetic switching of a magnetic bit. Via magnetron sputtering, highly coercive SmCo films can be prepared with a distinct in-plane texture and therefore almost square-shaped in-plane hysteresis loops [*Ref. IV.11*]. We show here a $SmCo_5$ sample obtained by pulsed laser deposition [*Ref. IV.18*]. Starting by SmCo target, thin film has been fabricated on steel substrate using pulsed laser deposition system at deposition temperatures below Curie temperature (T_C = *700:900 °C*), on plastic substrate. The film have been realized without the fabrication of a seed layer [*Ref. IV.17*]. The typical thickness of the deposited film is 800 nm. A $SmCo_5$ is used to test the validity of our gradiometer system, shown in Figure IV.30, as imaging system on ferromagnetic material. The Figure IV.31 shows clearly the sample under test and the results carried out using the GMR 2nd order electronic gradiometer.

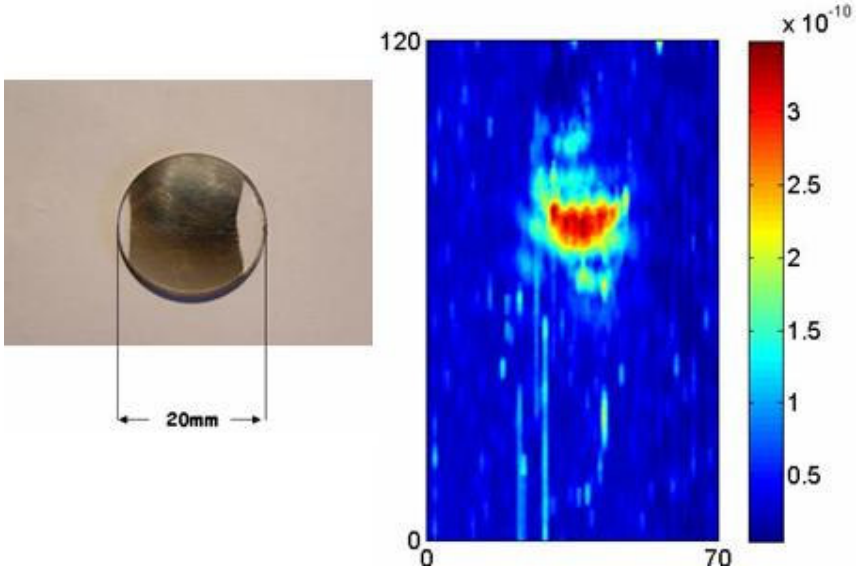

Figure IV.31 (Left) SmCo sample obtained by pulsed laser deposition; (Right) GMR 2nd order electronic gradiometer: 2D imaging of the ferromagnetic sample.[Ref. IV.18]

The measured magnetic moment of the film, after removing the spurious contributions of the substrate and the sample holder [*Ref. IV.18*], was $M = 2.06 \cdot 10^{-12}$ *Wb·m* which corresponds to a

magnetization $m = 0.66\ Wb/m^2$. The 2nd order GMR gradiomentric analysis shown in Figure IV.33 concerns the 2D magnetic image of the SmCo film sample. In the picture the magnetization is not uniform, more than one signal dipole is visible. The magnetic field gradient intensity, measured on the film surface versus the scan length, is up $0.3nT/cm$. The substrate's edge gives a magnetic intensity contribute of $0.15nT/cm$.

We, then, focalize the discussion on the use of GMR sensor as Eddy Current probe. In the Eddy Current Technique (ECT), an electromagnetic field is excited to variable frequency to induce a field of current in the material. In the presence of discontinuity in the material, which tears of fatigue, cuts, porosity etc, the induced currents in the material present distortions in their distribution. The variations in the distribution of the field of current produce flux variations that, in the case of induction coils, are measured through a measure of change of impedance according to the equation $Z\,i(t) = N\,d\Phi/dt$ and the expression that ties the material property to the penetration depth of the electromagnetic field is $\delta = 1/\sqrt{\sigma\mu\pi f}$. By using the Eddy Current Technique, it is possible to detect the geometry and the depth of the defect in conductive materials for processing or impact defects of the order of δ (hundreds of μm).

Most research using magnetoresistive sensors has been focused in the direction of deep flaw detection, a critical problem in the inspection of aircraft structures, such as riveted multilayers. Others approaches a different problem, that of detecting small defects, such as short cracks at the surface or near the surface of a conductive specimen. This can be of particular importance in different applications, such as detecting fatigue cracks in early stages of development [*Ref. IV.12 - Ref. I.53*]. It is envisaged that these two problems are optimally addressed using different probe designs. In general, in order to obtain a high penetration depth of the field and eddy currents into the material, large coils producing low-frequency excitation fields are required [*Ref. IV.16*].

At the same time the resolution of the probe is limited by the coil diameter, and the only way to enhance the resolution is to reduce the coil dimensions. Therefore, in the case of deep flaw detection, only relatively large defects are reliably detected. Currently, inductive probes based on small pickup coils are used for surface crack detection with high resolution. However, the reduction of the coil diameter leads to the decrease in sensitivity of the these probes. This is because the induced voltage depends linearly on the magnetic flux intercepted by the pickup coil, which in turn is proportional to its cross-section area [*Ref. IV.17*].

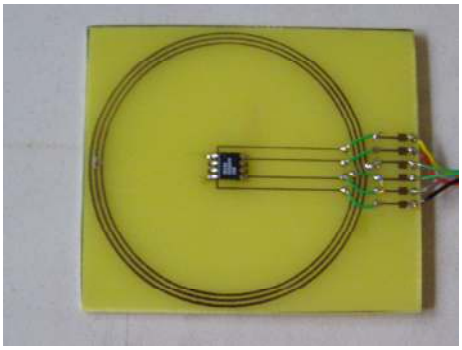

Figure IV.32 The GMR sensor assembly utilizing a cylindrical coil surrounding the sensor.

The main components of the eddy-current probes comprise either a relatively large cylindrical coil or a flat spiral coil with the GMR sensor located on the coil axis. The sensing axis of the GMR probe is coplanar with the surface of the specimen.

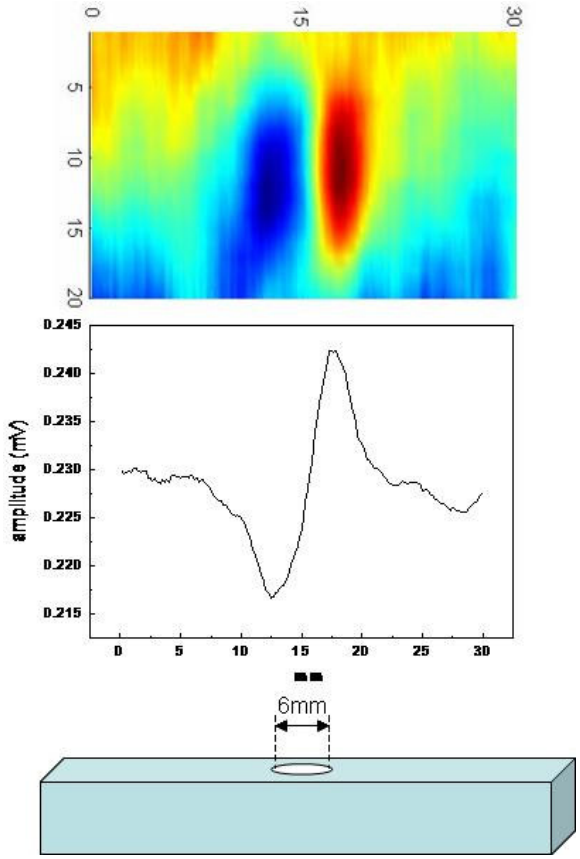

Figure IV.33 GMR Imaging of AlTi (Ti_6) specimen characterized by a 6mm hole. The measurement has been done with a 30mm diameter coil (supply current 30 mA and 6kHz frequency). The output of the GMR based eddy current probe reveals exactly the hole dimensions.

The excitation field on the coil axis, being perpendicular to the sensing axis of the GMR films, has no effect on the sensor. In a defect-free specimen, of the induced eddy currents because their circular symmetry will produce no effect on the sensor output. In the presence of a defect, output signal from the sensor is produced only by the perturbation of the eddy-current flow path.

Figure IV.33 shows the result of a single GMR based eddy current probe. The 30mm diameter excitation coil is supplied by 30*mA* current at 6*kHz* frequency. The sample is an AlTi (Ti_6) table characterized by a 6*mm* hole. The test is used to establish the possibility of achieving a GMR based eddy current probe in which the spatial resolution depends on the sensor and not on the excitation coil. Despite the coil has a diameter of 30*mm*, the configuration shown in Figure IV.32 is characterized by a spatial resolution of the order of 0.1*mm*. The high resolution is confirmed by the distance between the two peaks that is 6mm, just as the hole diameter previously measured.

References

Ref. IV.1 W.F. Arvin, Review of Progress in QNDE, Vol. 15, 1145, Plenum Press, New York, (1996)

Ref. IV.2 E.S. Boltz and T.C. Tiernan, Review of Progress in QNDE, Vol. 17, 1033, Plenum Press, New York, (1998)

Ref. IV.3 B. Wincheski and M. Namkung, Review of Progress in QNDE, Vol. 18, 1177, Plenum Press, New York, (1999)

Ref. IV.4 NVE Sensor Engineering and Application Notes, Nonvolatile Electronics, INC., (2003)

Ref. IV.5 B. Dieny, V. Speriosu, S. Parkin, P. Baumgart, and D. Wilhoit, J. Appl. Phys. 69, 8, 4774-4179 (1991)

Ref. IV.6 D. Heim, R. Fontana, C. Tsang, V. Speriosu, B. Gurney, M. Williams, IEEE Trans. Magn. 30, 2,(1994)

Ref. IV.7 C. Tsang, R. Fontana, T. Lin, D. Heim, V. Speriosu, B. Gurney, M. Williams, IEEE Trans. Magn. 30, (1994)

Ref. IV.8 C. Tsang, M. Chen, T. Yogi, and K. Ju, IEEE Trans. M a p . 26, 5, 1689-1693 (1990)

Ref. IV.9 J. Fraden, AIP Handbook of Modern Sensors, American Institute of Physics, New York, (1993)

Ref. IV.10 H.T. Hardner, M.B. Weissman, M.B. Salamon, and S.S.P. Parkin, Phys. Rev. B, 48, 21, (1993)

Ref. IV.11 F.J. Cadieu, Physics of Thin Films, Academic Press, Boston, p.145 (1992)

Ref. IV.12 M. Valentino, A. Ruosi, G.Pepe and G.Peluso, Physica C, 372-376 (2002)

Ref. IV.13 A.Ruosi, M.Valentino, V. Lopresto, G.Caprino, Journal of composite Material 56, 141-149 (2002)

Ref. IV.14 C. Bonavolontà, G. Peluso, G.P. Pepe, M. Valentino, EPJ 42, 491-496 (2004)

Ref. IV.15 C. Bonavolontà, G. P. Pepe, G. Peluso, M. Valentino, G. Caprino and V. Lopresto, IEEE Trans. Appl. Superconductivity 15, N°2, 711-714 (2005)

Ref. IV.16 Z. Mottl, Non-Destruct. Test. Int., vol. 23, pp. 11–18, (1990)

Ref. IV.17 J. Sayama, T. Asahi, K. Mizutani, T. Osaka, J. Phys. D: Appl. Phys. 37 (2004)

Ref. IV.18 L. Allocca,U. Gambardella, A. Morone, M.Valentino, Laser Deposition of SmCo Thin Film, SPIE (2007)

Conclusions

In this thesis the physical and technological characteristics of the GMR sensors are reported. The details on the physical properties of the sensors and the potentiality of this device as magnetic field detectors has been discussed.
A large introduction, on the magnetoresistive sensors GMR and AMR, shows how this sensors offer a good trade-off in terms of performance versus cost. Moreover they have small dimensions, high sensitivity over a broad range of frequency (from hertz to megahertz domains), low noise, and they can operate at room temperature.
In this work a lot of effort has been focused to discuss the experimental results concerning the GMR as magnetic probe for NDE testing on metallic materials using eddy currents. The experimental material has been collected during my permanence as Phd student at NDE laboratories of the CNR-INFM in Naples. The main results collected in the work can be resumed as follow.

With the aim of introduce the basic concept usefull to describe the physics of such magnetic materials, a brief review of the giant magnetoresistance (GMR) effect exhibited by magnetic multilayers, granular alloys, and related materials has been done in the first and second chapters of this thesis. Then, starting with the magnetoresistive (MR) effect characterization, we covered a description of the phenomenon in term of spin-dependent conduction and electronic band structure in magnetic multilayers. In the follow of cap III, using the Boltzmann theory, the macroscopic transport equations of magnetic multilayers in the case of current polarization perpendicular to the layers has been described. With the aid of numerical simulations, the GMR behaviour of a magnetic multilayer changing the main properties of the magnetic multilayer has been reported. In other terms, the GMR has been studied changing the non magnetic layer thickness dependence, the magnetic layer thickness dependence and the dependence of the magnetoresiste effect by the number of layers. This results could be useful to design and fabricate a new sensors starting from the fundamental magnetic properties of the materials.
Finally in the chapter IV, we reported the characterization of the single sensors in terms of magnetic environmental noise analysis and the its magnetic calibration. Moreover in the Cap. IV the

prototype of an electronic gradiometer realized using single magnetometer has been realized and characterized. In fact, we proved that this configuration, together with the applied filtering technique, is able to reduce the magnetic noise and raising the signal to noise ratio. To shown the advantage joint to the use of electronic gradiometer and the goodness of our experimental set-up, several results have been reported.

Moreover a 2^{nd} order GMR gradiometer realized in the CNR-INFM NDE laboratory, has been showed. It has been realized with the aim to measure the magnetic characteristic of a material on the micrometric scale. The 2D magnetic imaging measured on a SmCo sample has been discussed. This results shows the possibility to execute scanning microscopic analysis with high sensitivity and spatial resolution at room temperature.

Finally further measurement has been made by using a GMR eddy current probe. Several metallic structures and composite material of aeronautical interest, i.e. single layer metals, multilayers and FML laminates has been measured. The test has been performed to establish the possibility of achieving a GMR based eddy current probe to detect millimetric defect in metallic alloy with a good sensitivity and high spatial resolution comparable with the conventional search coil.